DISS. ETH NO. 22835

Field Cameras for Magnetic Resonance Systems

A thesis submitted to attain the degree of

DOCTOR OF SCIENCES of ETH Zurich

(Dr. sc. ETH Zurich)

presented by

Benjamin Emanuel Dietrich
MSc ETH EEIT, ETH Zurich

born on December 7th, 1982
citizen of Basel, Switzerland

accepted on the recommendation of
Prof. Dr. Klaas P. Pruessmann
Prof. Dr. Richard Bowtell

2015

Contents

Summary vii

Zusammenfassung xi

1 Introduction 1
- 1.1 Magnetic Resonance Imaging . . . 1
- 1.2 Magnetic Field Monitoring . . . 5
  - 1.2.1 Field Probes . . . 5
  - 1.2.2 Spatial Field Expansion . . . 7
  - 1.2.3 Promises and Limitations . . . 10
- 1.3 Thesis Outline . . . 12

2 A Stand-Alone Field Camera 15
- 2.1 Introduction . . . 15
- 2.2 Methods . . . 17
  - 2.2.1 Hardware . . . 17
  - 2.2.2 Experiments . . . 25
- 2.3 Results . . . 27
  - 2.3.1 Monitoring and Image Reconstruction . . . 27
  - 2.3.2 Mechanical Vibrations . . . 33
  - 2.3.3 Field Drifts / Fluctuations . . . 33
- 2.4 Discussion . . . 36

3 Concurrent Gradient and RF Pulse Monitoring 39
- 3.1 Introduction . . . 39

3.2 Methods . . . 41
3.2.1 Imaging System . . . 41
3.2.2 Monitoring System . . . 42
3.2.3 Monitored Sequences . . . 49
3.3 Results . . . 49
3.4 Discussion . . . 59

4 Continuous Monitoring 61
4.1 Introduction . . . 61
4.2 Methods . . . 63
4.2.1 Probe Frontend . . . 64
4.2.2 Transmit/Receive Hardware . . . 67
4.2.3 Sequence Timing and Synchronization . . . 69
4.2.4 High-Level Signal Processing . . . 70
4.2.5 Experiments . . . 72
4.2.6 Sensitivity and Consistency Assessment . . . 73
4.3 Results . . . 74
4.3.1 Field Monitoring . . . 74
4.3.2 Trajectory Monitoring . . . 77
4.3.3 RF Pulse and Gradient Monitoring . . . 82
4.4 Discussion . . . 82

5 Higher-Order Continuous Monitoring 89
5.1 Introduction . . . 89
5.2 Methods . . . 90
5.2.1 Monitoring System . . . 90
5.2.2 Scanner and Shim Hardware . . . 97
5.2.3 Experiments . . . 98
5.3 Results . . . 99
5.3.1 Single-Shot Impulse Response Function Measurement . . . 100
5.3.2 Sequence Monitoring . . . 101
5.3.3 Dynamic Shimming . . . 106
5.4 Discussion . . . 109

6 k-t-Calibration **113**
6.1 Introduction . . . 113
6.2 Theory . . . 114
6.3 Methods . . . 116
6.3.1 Hardware . . . 116
6.3.2 Phase Map Generation . . . 116
6.3.3 Non-Linear System Solving . . . 117
6.3.4 Experiments . . . 119
6.3.5 Higher-Order Fields . . . 120
6.4 Results . . . 121
6.4.1 Static Fields, Precision and Phase-Map Resolution . . . 121
6.4.2 Higher-Order Fields . . . 121
6.4.3 Image Reconstruction Based on k-t-Calibrated Trajectory . . . 123
6.5 Discussion . . . 125

7 Conclusions and Outlook **129**

References **133**

Curriculum Vitae **145**

List of Publications **147**

Acknowledgements **157**

Summary

Magnetic Resonance Imaging (MRI) is an established biomedical imaging modality that emerged over the last decades to an indispensable medical diagnostic tool. This success is largely owned to the fact that it is non-invasive and offers a large variety of soft tissue contrasts. MRI is based on the physical effect of nuclear magnetic resonance (NMR) and requires for signal generation a strong homogeneous static magnetic field, as well as precise dynamic magnetic fields for signal manipulation and spatial encoding. Despite the enormous precision of current MRI systems, many applications are still limited by inaccuracies, instabilities and fluctuations of these fields. Thus many hardware, signal encoding, acquisition, and image reconstruction optimizations would benefit from insight into the actual field evolutions. These can be measured with NMR field probes with very high sensitivity. However, due to relaxation of the macroscopic magnetization and signal loss due to internally and externally induced field inhomogeneities inside the probes, these measurements are so far limited to short, stroboscopic acquisitions and thus, the full field dynamics of arbitrary MRI sequences cannot be detected within a single measurement. To date, these sensors are also to a great extent dependent on the employed MRI system. The main focus of the present work is the development of a scanner independent, continuous magnetic field measurement method for MRI.

In a first step, an independent, stand-alone, field probe based monitoring system has been developed that enables high sensitivity measurements and analyses of the field evolutions during typical MRI sequences, as well as during undefined states of the MRI sys-

tem. This measurement system, called field camera, is based on a modular design, which comprises direct digitization of the radio frequency signals of the field probes and digital signal processing on field programmable gate arrays. This allows for fast adaptation to the rapidly changing requirements in research. This monitoring system was then used for the measurement of k-space trajectories for improved image reconstruction, for field drift measurements following intensive gradient system use, as well as for the analysis of mechanical resonances of the gradient system.

Current NMR field probe based monitoring methods do not address the radio frequency fields generated by the MRI systems and therefore do not deliver a complete view of all relevant field dynamics. This limitation is overcome by spectrally decoupling the monitoring experiment from the hydrogen (^{1}H) based imaging experiments. Thus, the nucleus for field sensing was changed to fluorine (^{19}F), allowing concurrent monitoring and imaging. The radio frequency waveforms could then be acquired and mapped to their respective sources by means of electromagnetic coupling into the probe's electronics, frequency-dependent signal scaling and dual-band demodulation. This allowed the measurement and analysis of various MRI sequences, including multi-channel transmit examples.

To overcome the limitation of measurement duration, a method was developed that allows continuous monitoring over arbitrary periods, which are only limited by data storage space. It is based on fast probe re-excitation with multiple probe sets and probe signal lifetimes in the 100 µs range. Due to these short lifetimes signal dephasing is, even under very strong gradients, no longer a limiting factor. The use of multiple probe sets gives each probe more time for relaxation and thus reduces the risk of spurious echo formation and SNR loss due to steady state effects. The sensitivity of the field measurements was analyzed under static conditions, and image reconstruction was used to verify the correctness of the

monitored trajectories. Several MRI sequences were measured with this method, such as diffusion weighted EPI with strong gradients. The developed field camera thus permits, paired with the radio frequency field measurement capability, insight into all field dynamics relevant for MRI signal formation and encoding.

In order to spatially resolve fields of higher spatial order, as created by so-called shim coils for the correction of field inhomogeneity inside the subject, the continuous field camera was improved with respect to probe design and number of channels. The resulting 32-channel continuous field camera allowed spatial field expansions on a full 3^{rd}-order spherical harmonic basis with two alternated probe sets. The field camera was applied to measure dynamic shim updates and impulse response functions of the gradient and shim system.

Since a substantial part of the errors in the continuous field measurements were of systematic nature, a method for probe phase calibration in k-space and time domain was developed, reducing reproducible errors due to field inhomogeneity inside the probe.

In this thesis different magnetic field cameras were developed for scanner independent operation, continuous field monitoring and concurrent radio frequency field monitoring. They provided insight into previously hardly accessible field dynamics in MRI systems, which can simplify sequence development and debugging. The measured trajectories have successfully been used to improve image reconstruction. The ability to measure continuously over arbitrary durations, only limited by data storage, might enable new real-time field control, system surveillance and failure prediction methods. The achieved fast system characterization by means of single-shot impulse response function measurements promises new approaches for time-resolved system characterization, e.g. under thermal stress.

Zusammenfassung

Magnetresonanztomographie (MRT) ist ein etabliertes, nicht invasives biomedizinisches Bildgebungsverfahren, das sich in den letzten Jahrzehnten vor allem durch seine Vielfalt an Gewebekontrasten zu einem unverzichtbaren medizinischen Diagnoseinstrument entwickelte. MRT basiert auf dem physikalischen Effekt der Kernspinresonanz (NMR) und benötigt für die Signalerzeugung ein starkes homogenes Hintergrundmagnetfeld, sowie exakte dynamische Magnetfelder für die Signalmanipulation und räumliche Kodierung. Trotz der hohen Präzision von gegenwärtigen MRT-Systemen limitieren Ungenauigkeiten, Instabilitäten und Fluktuationen dieser Felder noch immer viele Anwendungen. Sowohl zur Verbesserung der Hardware, sowie auch zur Optimierung von Kodierung, Akquisition und Bildrekonstruktion ist daher der Einblick in das tatsächliche Feldverhalten hilfreich. Mithilfe von NMR-basierten Magnetfeldproben können die tatsächlichen Feldverläufe mit sehr hoher Sensitivität gemessen werden. Aufgrund der Relaxation der makroskopischen Magnetisierung, sowie von intern und extern induzierten Feldinhomogenitäten in diesen Proben und dem damit verbundenen Signalverlust, sind diese Messungen jedoch auf kurze, stroboskopische Einblicke limitiert. Die vollständige Felddynamik kann daher oft nicht innerhalb einer Messung erfasst werden. Ausserdem ist der Betrieb dieser Sensoren bisher in grossem Masse abhängig von dem zu untersuchenden MRT System. Die vorliegende Arbeit widmet sich der Entwicklung einer MRT-System unabhängigen, kontinuierlichen Magnetfeldmessmethodik für MRT.

Zuerst wurde ein unabhängiges Messsystem entwickelt, das erlaubte, sowohl die Feldverläufe während typischer MRT-Sequenzen,

als auch Feldverläufe in undefinierten Zuständen des MRT-Systems mit sehr hoher Sensitivität zu messen und zu analysieren. Dieses Messsystem, auch Feldkamera genannt, basierte auf einem modularen Aufbau. Direkte Digitalisierung der von den Proben empfangenen Radiofrequenzsignale und anschliessende digitale Signalbearbeitung auf programmierbaren Gatterfeldern ermöglichte eine einfache und schnelle Adaption an die rasch ändernden Anforderungen in der Forschung. Dieses Messsystem wurde unter anderem dafür benutzt Feldverläufe und k-Raum Trajektorien zu messen, Felddrift nach intensiver Gradientennutzung zu bestimmen und mechanische Resonanzen des Gradientensystems zu identifizieren.

Bisherige auf NMR-Proben basierte Monitoring-Methoden unterstützten keine Messung von Radiofrequenzfeldern in MRT-Systemen, weshalb diese bisher kein vollständiges Bild aller für MRT relevanten dynamischen Felder lieferten. Um diese Fähigkeit zu erreichen wurde in einem nächsten Schritt Fluor (^{19}F) als Probenkern eingesetzt und damit die Feldmessung spektral von der Wasserstoffbasierten (^{1}H) Bildgebung separiert. Die Radiofrequenzfelder konnten dann durch elektromagnetische Einkopplung in die Probenelektronik, frequenzabhängige Signalskalierung und Mehrkanaldemodulation mitgemessen und der jeweiligen Quelle zugeordnet werden. Diese Methode wurde benutzt um diverse MRT-Sequenzen, unter anderem mit Multikanal-Transmittern, zu analysieren.

Um die Limitationen in Bezug auf Messzeit zu überwinden wurde eine Methode entwickelt, die kontinuierliche Feldmessungen erlaubte. Diese Methode basierte auf schneller Wiederanregung von mehreren alternierten Proben-Sets mit Signallebenszeiten im 100 µs Bereich. Aufgrund dieser kurzen Relaxationszeiten war Probensignal-Dephasierung auch unter sehr starken Gradienten kein limitierender Faktor. Die Verwendung von mehreren Proben-Sets gab jeder einzelnen Probe mehr Zeit zur Relaxation und reduzierte somit die Bildung störender Echos. Die Präzision wurde durch Sensitivitätsanalysen unter statischen Feldern untersucht und die

Richtigkeit der gemessenen Trajektorien durch Bildrekonstruktion verifiziert. Diverse MRT-Sequenzen wurden damit gemessen, wie z. B. diffusionsgewichtete EPI mit starken Gradienten und langen Auslesephasen.

Zusammen mit der Fähigkeit die Radiofrequenzsignale zu messen erlaubte das entwickelte System somit einen kontinuierlichen Einblick in alle relevanten Felder für die Manipulation und räumliche Kodierung von MRT-Signalen. Für die Messung von Felddynamiken mit höherer räumlicher Ordnung, wie z. B. erzeugt von Shimspulen zur Korrektur von Feldinhomogenitäten in der Versuchsperson, wurde die kontinuierliche Feldkamera optimiert und mit zusätzlichen Kanälen erweitert. Die Fähigkeit Felder kontinuierlich auf einer sphärisch harmonischen Basis dritter Ordnung zu entwickeln wurde dann benutzt um MRT-Sequenzen in Bezug auf Felder höherer Ordnung zu analysieren. Zudem wurden Sequenzen mit dynamischen Shim-Updates untersucht, sowie Übertragungsfunktionen der Gradienten und Shims gemessen.

Da ein wesentlicher Teil der Fehler in den kontinuierlichen Feldmessungen systematischer Natur war, wurde abschliessend eine Methode zur Probenphasen-Kalibration entwickelt. Diese Kalibration in Zeit und k-Raum ermöglichte es reproduzierbare Fehler aufgrund von Feldinhomogenitäten in den Proben zu reduzieren.

In dieser Arbeit wurden verschiedene Feldkameras für den MRT-System unabhängigen Betrieb, kontinuierliche Feldmessung und gleichzeitiges Monitoring der Radiofrequenzsignale entwickelt. Diese Feldkameras gaben Einblick in bisher nur schwer zugängliche Felddynamiken, was eine wesentliche Vereinfachung der Fehlersuche und Sequenz-Entwicklung erlaubt. Die gemessenen Trajektorien wurden zudem erfolgreich zur Verbesserung der Bildrekonstruktion eingesetzt. Die Fähigkeit kontinuierlich über beliebige Zeiträume zu messen, nur limitiert durch die Datenspeichergrösse, könnte neue Methoden zur Echtzeit-Feldsteuerung, Systemüberwachung und Fehlervorhersage ermöglichen. Die schnelle, nur we-

nige Sekunden dauernde Systemcharakterisierung mittels Übertragungsfunktionen verspricht neue Ansätze für die Untersuchung von Systemveränderungen, wie sie z. B. unter thermischer Belastung durch intensive Gradientennutzung auftreten.

1 Introduction

1.1 Magnetic Resonance Imaging

Magnetic resonance imaging (MRI) is based on the nuclear magnetic resonance (NMR) effect, which was first discovered by Edward Purcell and Felix Bloch in 1946 [1], [2]. If nuclei with a magnetic dipole moment, in MRI typically hydrogen due to its abundance in biological tissues, are exposed to an external static magnetic field, their nuclear magnetic moments or spins, partially polarize and precess at the so called Larmor frequency around the magnetic field vector [3]. The value of the Larmor frequency is linked to the external field by the nucleus-specific gyromagnetic ratio and is in the range of 20 MHz to 400 MHz for hydrogen in typical MRI background fields. When exposed to a magnetic field oscillating at this Larmor frequency, spin state transitions and phase coherence can be induced, resulting in tipping of the apparent macroscopic magnetization away from the main magnetic field vector towards the transverse plane. Upon such manipulation, called excitation, the macroscopic magnetization precessing around the main field vector returns back to the thermal equilibrium state, governed by the sample specific longitudinal relaxation time T_1 and transverse relaxation time T_2. During this process, the oscillating transverse component can be detected by Faraday induction in nearby detector coils. This radio frequency (RF) signal, received from the magnetized sample, is enriched with an abundance of information, ranging from chemical content and magnetic field exposure to spin density, local spin environment and motion,

which are all encoded in the frequency, signal strength and decay rate. Smart manipulation of the macroscopic magnetization through the two available inputs — longitudinal background field and transverse RF irradiation — allows signal encoding such that this multitude of sample properties can be deduced and spatially resolved from the received RF signals. Since biological tissues are largely transparent for signals of this frequency range, this requires neither an invasion into the sample nor the destruction of it.

Based on this principle MRI evolved from the first images, made in the 1970's [4]–[6], to a very versatile biomedical imaging modality that is now used in everyday clinical diagnostics, as well as cutting-edge research. The broad success of MRI builds on its non-invasive, non-toxic nature combined with a very large variety of available soft tissue contrasts. Compared to competing modalities such as X-ray, MRI does not expose the subject to ionizing radiation and hence enables recurring examinations without radiation dose tracking, which is especially useful for clinical studies.

Creation of state of the art magnetic resonance (MR) images involves very complex systems, joining physics and engineering expertise from various fields. Today's MRI systems are typically based on a cylindrical main magnet built from superconductors cooled by liquid helium, reaching field strengths from 0.5 T to 9 T. Inside the magnet bore a set of coils, called gradient coils, generates switchable field gradients for position dependent manipulation of the longitudinal main field. This enables spatial signal encoding and hence image formation. These coils can typically generate field gradients up to a range of $40\,\mathrm{mT\,m^{-1}}$ to $100\,\mathrm{mT\,m^{-1}}$. The available bandwidth for gradient switching (typically $< 50\,\mathrm{kHz}$) is largely limited by the tremendous reactive power in the MW range that needs to be handled due to the large inductive loads. The second input for manipulation of the sample's magnetization — the transverse RF field — is typically actuated by near field transmitters placed inside the gradient coils, transmitting at power levels in

the 0.1 kW to 20 kW range. In order to receive the very weak signals emitted by the sample upon excitation (µW range), optimized near field receive coils are placed as close to the subject as possible. From there the RF signals pass the receive chain comprising pre-amplifiers, gain stages and filters until they are digitized by the spectrometer and processed into the final image.

Even though current systems reach remarkable levels of complexity and precision, culminating in costly developments, installations, maintenance and operator training, there are still many challenging problems that need to be solved. Among them are the need for more sensitivity and higher resolution to resolve subtle tissue structures, examination speed and robustness against subject motion.

The most straightforward approach to gain more sensitivity is to increase background field strength, leading to an increased polarization, macroscopic magnetization and ultimately signal-to-noise ratio (SNR). Exposure to very strong static magnetic fields is well tolerated by humans and does not cause any permanent harmful effects according to current knowledge. Besides, several methods gain specificity, such as increased line separation in spectroscopy [7]. However, there are some side effects due to the higher field strength: RF field non-uniformity due to shorter wavelengths, increased RF induced losses, and faster signal decay due to susceptibility induced field inhomogeneity inside the subject. To reduce the RF non-uniformity multichannel transmit systems were developed [8], enabling more refined signal encoding during excitation. The increased RF losses inside the subject, paired with uncontrolled field superpositions from several transmitters due to unknown tissue transitions can lead to RF induced heating and thereby threaten subject safety, calling for robust RF surveillance. In order to reduce the subject dependent main field inhomogeneity the gradient systems were extended with so called shim coils, which produce spatially higher-order correction fields [7].

The quest for more encoding speed and higher resolution led to sophisticated solutions in gradient coil engineering, such as active shielding [9], [10] and pre-emphasis to reduce and counteract eddy currents in surrounding conducting materials, which hamper fast field changes. Current gradient switching speeds and strengths reach regimes that can induce pain by peripheral nerve stimulation [11], [12], questioning the usefulness of further increases.

On the signal processing side many methods emerged, which try to leverage as much information as possible for either image reconstruction or acceleration of image acquisition, such as coil sensitivities in parallel imaging [13]–[15].

Although many of these improvements contributed to the development of highly accurate magnetic fields in present-day MRI systems, a range of confounding mechanisms still limit magnetic field fidelity and therewith many advanced imaging methods. These mechanisms include magnet drifts, remaining eddy currents induced by the switching of gradient and shim fields [16], coupling between coils, finite linearity and stability of amplifiers and supplies, mechanical resonances [17], [18], heating effects [19], breathing, blood pulsation, digestion and other motion induced field fluctuations, and many more. Not least, the field evolution in an MR system may also be flawed due to hardware deterioration or failure as well as programming errors. At the image level, such field imperfections can impair results in various ways ranging from blurring and distortion to artifacts and signal dropouts. These issues continue to be addressed at the hardware and sequence levels as well as by advances in signal processing and image reconstruction. All these optimization approaches require insight into the underlying imperfections, calling for immediate observation by magnetic field monitoring [20]–[23]. To serve the purpose, such measurements must be feasible in high background fields, offer high sensitivity and temporal resolution and should also capture the relevant spatial degrees of freedom of the magnetic field.

1.2 Magnetic Field Monitoring

1.2.1 Field Probes

Even though a large variety of magnetic field sensors exists [24], [25], only a few of them offer sufficient sensitivity and the ability to operate within the harsh electromagnetic environment of MR systems. Among the most popular sensors for magnetic field measurements are induction coil sensors [26]. Although they offer a very large detection range from nT to T, they can only detect field changes and hence rely on noise-prone integration in order to capture full field evolutions. Other sensor types, such as magneto-resistive, Hall-effect, Flux-gate, or superconducting quantum interference device (SQUID) sensors suffer from various shortcomings, i.e. high background field incompatibility, low sensitivity, low temporal resolution and difficult handling due to liquid nitrogen cooling requirements. Remarkably, the currently most promising sensors for use in MR systems make used of the same physical principle as the imaging experiments — NMR.

NMR field probes, are based on miniaturized NMR experiments inside a small confined volume. First implementations [27] employed spectral absorption measurements to extract the Larmor frequency f and therewith the magnetic field magnitude B at the probe position $\mathbf{r}$ by knowledge or calibration of the nuclei specific gyromagnetic ratio γ:

$$f = \gamma\, B(\mathbf{r}). \tag{1.1}$$

While this approach delivers excellent results with sub-ppm resolution for mapping of static fields, it does not deliver the measurement bandwidth required for direct observation of the field dynamics present in modern MRI systems. More recent methods [20], [22], [23], [28] therefore apply the same pulsed NMR approach as MRI does.

Pulsed NMR based field measurements use the free induction decay (FID) signal emitted by the probe sample upon application

of a short excitation pulse at the approximate Larmor frequency. The phase evolution $\phi(t)$ of the observed FIDs is then proportional to the integral of the magnitude of the magnetic field at the probe location:

$$\phi(t) = \gamma \int_0^t B(\mathbf{r}, \tau) \mathrm{d}\tau + \phi_0, \tag{1.2}$$

with ϕ_0 being the initial phase after excitation. Temporal derivation of the phase evolution $\phi(t)$ results in a time resolved version of Eq. 1.1, delivering the field magnitude. The temporal resolution of this field magnitude evolution is solely limited by the spectrometer used for signal acquisition (typically µs range). Alternatively, when the phase evolution is linear throughout the whole FID such as under static conditions, the field can be determined from the slope by means of a linear fit, yielding a very high sensitivity [20].

Current field probe designs used for field monitoring in MRI systems [20], [22], [23], [29]–[31] are mostly based on liquid state samples, using either ^{1}H, ^{2}H or ^{19}F nuclei. An advantage of liquid state samples is that both longitudinal and transverse relaxation time, T_1 and T_2, respectively, can be rather easily adjusted by addition of selected compounds, such as for example soluble paramagnetic salts in case of ^{1}H (H_2O) probes. This adjustability plays an important role in tuning measurement duration and precision. To give an example, a very short T_2 in the sub ms range paired with a long T_1 in the second range is rather common among solid state samples. Consequently, this allows only for very short readouts and requires a long dead-time before re-excitation due to the slow longitudinal relaxation.

In general, field measurement sensitivity strongly depends on the spin density of the selected compound and on the gyromagnetic ratio of the nuclei [20]. Nuclei with a high gyromagnetic ratio, such as ^{1}H (42.576 MHz T^{-1}) would thus deliver a high sensitivity, but at the same time interfere with the imaging experiments, making concurrent monitoring and imaging problematic. Therefore ^{19}F

is often the next best choice, delivering spectral decoupling from the imaging experiments and an almost equally high gyromagnetic ratio ($40.052\,\mathrm{MHz\,T^{-1}}$).

Figure 1.1 shows a schematic representation of a probe design used in current MRI research [20], [29]–[31]. A solenoid around a small glass capillary ($\approx$ 1 mm diameter) filled with the NMR active liquid serves as a transmit-receive (T/R) coil and is connected to a tune-match circuit, transforming the impedance of the solenoid at the expected resonance frequency to the $50\,\Omega$ impedance of a coaxial cable. The size of the field sensing NMR active droplet is confined by the glass capillary and sensitivity profile of the solenoidal coil. Encapsulation within a susceptibility matched ellipsoidal material, such as doped epoxy resin [20], ensures that the different susceptibilities of the involved materials (especially coil wire) do not cause field inhomogeneities inside the probe droplet. Any field inhomogeneity, e.g. caused by external gradients, results in different spins precessing with different frequencies, which ultimately leads to signal loss due to dephasing. Hence the droplet size is an important design parameter with respect to spatial resolution and the maximum gradient moment that can be monitored.

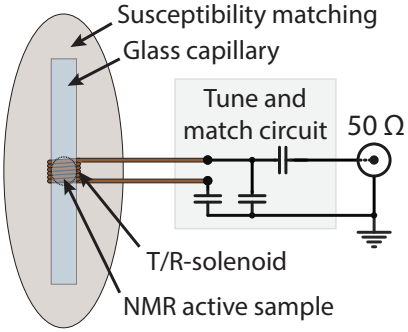

Figure 1.1: Schematic representation of a field probe.

1.2.2 Spatial Field Expansion

When analyzing the fields inside an MRI system, different temporal and spatial regimes can be distinguished. Static perturba-

tions of the ideally homogeneous longitudinal main field are mainly caused by magnet imperfections, and differences in the susceptibility of the tissues and body parts under examination. While the magnet induced field distortions are spatially smooth and to a large degree negligible inside the specified homogenous volume, the susceptibility induced perturbations can be highly structured in space. Dynamic field components on the other hand originate mostly from outside of the subject, particularly from gradient and shim coils and eddy currents in the cryostat. Since these fields are orders of magnitudes weaker than the main field, the susceptibility induced perturbations also scale proportionally, rendering them nearly source-free in the volume of interest and thus allowing spatial expansion on a low number of spatially smooth basis functions b_i [21]:

$$B(\mathbf{r}, t) = \sum_i c_i(t)\, b_i(\mathbf{r}), \tag{1.3}$$

where c_i represents the field dynamics in the respective basis function indicated by the subscript i. The necessary spatial order of such expansion depends on the proximity of relevant field sources relative to the diameter of the volume of interest and affects the required number of surrounding probes. A typical choice of basis functions are spherical harmonics.

The temporal field magnitude evolution B_p of probe p, given the probe positions $\mathbf{r}_p$ and number of basis functions L, is then:

$$B_p = \sum_{i=1}^{L} b_i(\mathbf{r}_p)\, c_i(t). \tag{1.4}$$

In terms of vector-matrix notation this yields with the calibration matrix

$$\mathbf{P} = \begin{pmatrix} b_1(\mathbf{r}_1) & \cdots & b_L(\mathbf{r}_1) \\ \vdots & \ddots & \vdots \\ b_1(\mathbf{r}_N) & \cdots & b_L(\mathbf{r}_N) \end{pmatrix}, \tag{1.5}$$

N the number of probes, $\mathbf{B}$ a vector containing the probe local fields and $\mathbf{c}$ a vector containing the field dynamics:

$$\mathbf{B}(t) = \mathbf{P}\,\mathbf{c}(t). \tag{1.6}$$

The dynamics vector $\mathbf{c}$ can then be obtained by solving the inverse problem through simple application of the pseudo-inverse of the calibration matrix, indicated by $^+$:

$$\mathbf{c}(t) = \mathbf{P}^+\,\mathbf{B}(t). \tag{1.7}$$

Alternatively, a basis built from field patterns generated by gradient and shim coils can be used. In this case some or all of the components of $\mathbf{P}$ can be replaced with field values corresponding to unit actuation of the respective system input and probe. Such a field pattern-based calibration represents the fields in terms of driving ports of a linear time-invariant system, which is especially useful for field control applications [32], [33].

If the field dynamics are intended to be used for image reconstruction, it is typically a good idea to calibrate the probe positions in the coordinate system spanned by the gradients. The gradient coordinate system is usually slightly warped with respect to the Euclidean due to spatial non-linearity of the actual gradients. If gradient footprints are used for position calibration and an ideal spherical harmonic field model is subsequently applied for spatial interpolation, the encoding fields will be measured in the same slightly warped coordinates as the image, providing an easily interpretable, consistent relationship. Such a probe position calibration can be achieved by measuring the difference in the probe local fields under trusted reference gradients (typically in x, y and z direction) and under no gradient, yielding the probe coordinates $\mathbf{r}_p^G$:

$$(\mathbf{r}_p^G)_i = \frac{\Delta B_p^i}{G_i}; i = x, y, z, \tag{1.8}$$

with the superscript ^{G} indicating gradient coordinates and ΔB_p^i being the probe local field step produced by activation of the respective gradient G_i.

For image reconstruction the actual field evolution is not of primary interest, but rather the field's temporal integral, describing k-space trajectories. The k-space evolution can directly be obtained by similar spatial expansion of the probe phase evolutions:

$$\boldsymbol{\phi}(t) = \frac{\gamma_p}{\gamma_{MRI}} \mathbf{P}\, \mathbf{k}(t) + \boldsymbol{\phi}_0, \tag{1.9}$$

with γ_p being the gyromagnetic ratio of the nucleus in the field probes, γ_{MRI} the gyromagnetic ratio of the nucleus observed by the imaging experiment, $\boldsymbol{\phi}_0$ a vector containing the initial phases after excitation and $\mathbf{k}$ a vector containing the k-space coefficients of the selected basis functions. Application of the pseudo inverse $\mathbf{P}^+$ results then in the k-space coefficients:

$$\mathbf{k}(t) = \frac{\gamma_{MRI}}{\gamma_p} \mathbf{P}^+ \left(\boldsymbol{\phi}(t) - \boldsymbol{\phi}_0\right). \tag{1.10}$$

Field integration over time is in this case inherently and fully performed by coherent spin precession, rendering measurement noise in k-space trajectories only dependent on the SNR of the probes at the respective time.

1.2.3 Promises and Limitations

NMR field probe based magnetic field monitoring has already proven its usefulness for a variety of MRI applications, such as sequence analysis and improved image reconstruction [21], [23], [30], [34]–[38], retrospective correction of image artifacts caused by physiological field fluctuations [39], real-time motion correction [40] and gradient/shim characterization by means of impulse response function measurements [41], [42].

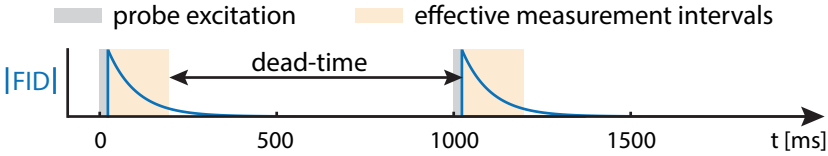

Figure 1.2: Typical probe acquisition windows.

Despite all these successes, current monitoring methods still suffer from various limitations, hampering their vast adoption and delaying an eventual paradigm shift in MRI technology.

The most fundamental limitations are the exponential signal decay due to T_2 and dephasing under strong field gradients. Upon a SNR dependent threshold the phase evolution of the FIDs can no longer be extracted and unwrapped, resulting in complete signal loss. State of the art field probes [29], [31] reach usable readout durations in the 100 ms range. After this time an additional dead-time has to be added before re-excitation, depending on the probe's longitudinal relaxation time T_1 as shown in Fig. 1.2. This dead-time prevents loss of SNR due to reduced longitudinal magnetization and spurious echo formation if the probes were subject to dephasing. As a consequence of these rather short snapshot field measurements, monitoring acquisitions need to be tightly integrated into the MRI system's sequence programs. Many sequences rely on long readouts and strong gradient moments and therefore cannot be measured within a single sequence execution, preventing complete monitoring of non-reproducible field fluctuations.

So far, field monitoring heavily relied on hardware and software of the MRI systems under test, since they share many common features due to their similar NMR-based principle. This renders the field measurements subject to limitations of these systems and their state of operation. While this poses no problem for most approaches using field monitoring data acquired during the imag-

ing readouts, this becomes a major limitation for methods relying on field data, e.g. during the MRI system's transmit periods when typically no signal acquisitions are allowed due to the risk of receive hardware destruction, or for system characterization and diagnostics during faulty system states or system construction.

Apart from highly homogeneous and precisely timed longitudinal main field distributions and modulations, MRI also relies on accurate transverse RF fields for excitation. These fields are so far not addressed by field probe based monitoring methods.

1.3 Thesis Outline

The underlying goal of this thesis is the development of an independent monitoring system/toolset, which delivers continuous and precise access to all magnetic fields relevant for MR signal formation and encoding.

Chapter 2 introduces a scanner independent stand-alone monitoring system, called field camera. This system is based on a modular hardware design, using direct RF digitization and digital signal processing on field programmable gate arrays (FPGA). Its monitoring capabilities are demonstrated on examples of k-space trajectory mapping for image reconstruction, measurement of field oscillations due to mechanical resonances and measurement of field drifts.

Chapter 3 explores how such a field camera can be used for observing the MRI system's transverse RF excitation fields. The developed RF pickup capability is then demonstrated by monitoring of various sequences, including experiments with multi-transmit arrays.

In Chapter 4 a continuous monitoring method based on rapid re-excitation of multiple probe sets with very short relaxation times in the µs range is presented, essentially freeing field monitoring from gradient induced signal loss and acquisition dead-times. This

capability is also combined with the RF monitoring technique and used to measure various sequences with long readouts and large gradient moments. The precision of the proposed method is further investigated under various conditions.

Chapter 5 deals with aspects of continuous monitoring and spatially higher-order fields. Suitable hardware modifications are presented, enabling simultaneous spatial field expansion on a full 3^{rd}-order spherical harmonic basis set. The resulting capability is demonstrated on examples of sequence/system analysis, single-shot gradient and shim impulse response function measurements, and monitoring of scans with dynamic shim updates.

Nonlinear probe phase components due to inhomogeneous fields inside the probe droplets lead to systematic field measurement errors. Chapter 6 presents a probe phase calibration method with the goal to remove such reproducible erroneous phase components.

Finally, Chapter 7 gives a short outlook on current and prospective uses of the hardware and methods developed in this thesis.

2 A Field Camera for MR Sequence Monitoring and System Analysis

Adapted from:

- *"A field camera for MR sequence monitoring and system analysis"*. Dietrich, Benjamin E.; Brunner, David O.; Wilm, Bertram J.; Barmet, Christoph; Gross, Simon; Kasper, Lars; Haeberlin, Maximilian; Schmid, Thomas; Vannesjo, S. Johanna; Pruessmann, Klaas P. *Magnetic Resonance in Medicine*, 2015. DOI 10.1002/mrm.25770.

2.1 Introduction

Using the same physical principle as MRI, the implementation of NMR field sensing can partly rely on hardware and methods that are already available in MRI systems. Early implementations did so to a large degree, involving the host systems entire transmit and receive chains, and incorporating field probe operation in pulse sequence programs [21], [22]. Yet the convenience of such close integration comes at the expense of flexibility, calling for greater independence from the MRI equipment and procedures to be monitored. First steps in this direction have been the transitions to local probe transmitters [30] and heteronuclear field probes, relying on fluorine or other non-proton samples for spectral decoupling from imaging experiments [23], [31], [34]. However, relying on the RF chains, spectrometer, and console of a host system still imposes major limitations and constraints, particularly in terms of sequencing options, measurement timing and bandwidth, data throughput,

and receiver specifications. Taking up receiver channels for field monitoring also limits the performance of imaging experiments. Moreover, towards the implementation of a genuine measurement device [29] it is unsatisfactory that field sensing should require the system under test to be fully operational.

In the present work these limitations are overcome by the transition to a stand-alone device, which will be referred to as a field camera. The proposed system is designed to record spatiotemporal field evolutions up to third order in terms of spherical harmonics, relying on an array of 16 field probes as first proposed in Ref. [29]. It is equipped with custom-designed RF chains including pulse synthesis, per-channel power amplification, transmit-receive (T/R)-switching, and two-stage amplification in the receive path. The cameras spectrometer is based on a software-defined-radio (SDR) design, using direct undersampling with high-rate analog-to-digital converters and signal manipulation mostly in the digital domain. The SDR approach simplifies the analog receive modules and adds flexibility to signal conditioning at the expense of large digital data flows [43]. Parallel, real-time signal processing at suitable rates is accomplished with field programmable gate arrays (FPGA) before data output for higher-level processing, display and storage.

To illustrate the versatility and usefulness of the proposed camera system, field dynamics have been studied in a selection of situations involving different time scales. Measurement of k-space trajectories is illustrated by monitoring of echo-planar-imaging (EPI) readouts and use of the results for image reconstruction. Further examples demonstrate the observation of field perturbation due to mechanical oscillation of gradient coils, thermal field drift after demanding gradient use, and field errors induced by external sources such as trams passing near the laboratory.

2.2 Methods

2.2.1 Hardware

The proposed system combines a field probe frontend with a transmit chain and a receive section based on a typical SDR approach with direct RF digitization. Figure 2.1.A schematically illustrates the most important system components and their interconnections. The system consists of 4 main building blocks: A field probe array, first and second stage receive and excitation electronics, and a digitization/digital signal processing block. The first stage comprising T/R-switches and amplifiers is closely integrated with the camera head for placement in the scanner bore to avoid SNR loss in long cables. The second stage and digital processing part are placed outside the high magnetic field due to the use of ferrite in baluns and power supplies.

Field Probe Array

The implemented field probe array is based on the probe design described in Refs. [29], [30] and consists of 16 ^{1}H-based field probes built from 0.8 mm inner diameter glass capillaries filled with H_2O doped with $CuSO_4$. For each probe a 5-turn solenoid serves as a T/R coil. The capillary is encased in an ellipsoidal, susceptibility-matched epoxy housing [20], [29]. The field probes are placed on the surface of a 17 cm diameter sphere using an approximately even distribution found by repulsive-potentials simulation. Fig. 2.1.A shows a schematic representation of the probe positions along with a close-up view of a probehead. Figure 2.1.E shows a fully assembled field camera head. Figure 2.1.F displays a packaged version with a custom-designed polyurethane housing including the 1st-stage transmit and receive electronics.

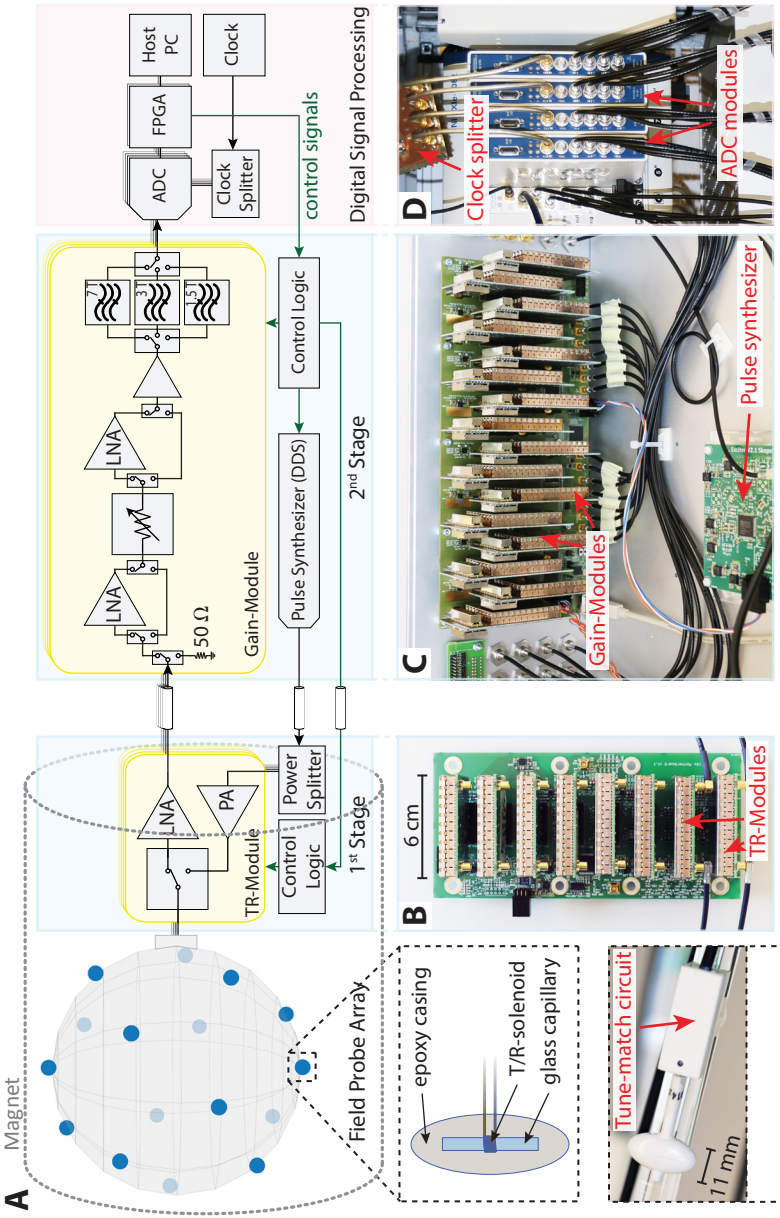
A
Magnet
Field Probe Array
TR-Module
LNA
PA
Control Logic
Power Splitter
1st Stage
Gain-Module
LNA
LNA
50 Ω
Pulse Synthesizer (DDS)
Control Logic
2nd Stage
control signals
Digital Signal Processing
ADC
FPGA
Host PC
Clock Splitter
Clock
B
6 cm
TR-Modules
C
Gain-Modules
Pulse synthesizer
D
Clock splitter
ADC modules
epoxy casing
T/R-solenoid
glass capillary
Tune-match circuit
11 mm

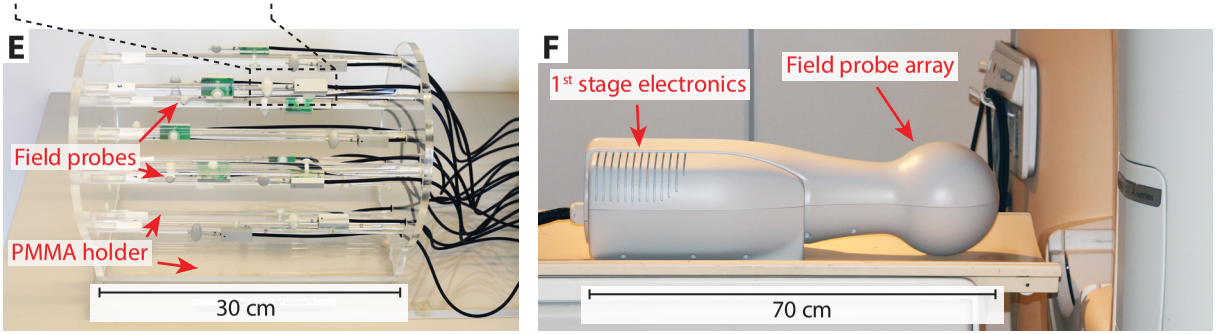

Figure 2.1: A: stand-alone monitoring system schematic and its building blocks. From left to right: field probe array; 1st stage electronics typically placed inside the scanner bore, comprising transmit-receive-switches, low noise amplifiers and excitation amplifiers; 2nd stage electronics comprising adjustable gain stage, anti-aliasing filters, and an excitation pulse generation module (DDS); and the digital signal processing stage consisting of digitizer modules, field programmable gate-array modules and a processing and control computer. B: 1st stage electronics prototype. C: 2nd stage electronics. D: digitizer modules. E: assembled field camera head and close-up of a field probe. F: packaged version including 1st-stage electronics, mounted in a polyurethane body.

Analog RF Chain

Each field sensor is connected to a T/R module (Fig. 2.1) consisting of a T/R-switch, an excitation power amplifier (PA), and a low-noise receive amplifier (LNA). Field effect transistor (FET)-based T/R-switches are used to achieve sub-microsecond switching performance. The more common option of PIN-diode switches exhibits better high-power signal compliance, but the required bias currents can sum up to a significant overall power consumption [44], which was avoided here to limit thermal changes in the measurement unit. Additional advantages of FET switches include integrated packaging and the fact that they do not require quarter-wavelength transformation, matching components, or high-current driver circuits. The noise figure of the T/R module, including T/R-switch and LNA, was determined at 0.9 dB. 16 T/R-modules are connected to one motherboard responsible for supply, trigger, and excitation pulse distribution. All components of the first stage (T/R-switch, LNA, PA, and control logic) are placed within approximately 50 cm distance from the field sensors. This is a tradeoff between cable losses in front of the LNA that cannot be recovered, and field perturbations caused by the electronics. Care was taken to keep those to a minimum and at the same time protect the sensitive electronics from gradient-induced eddy currents, which would otherwise cause detrimental signal modulations.

A second stage of electronics as depicted in Fig. 2.1 boosts and filters the receive signal such that it fits the ADC input range and prevents unintended aliasing. Digitally controllable attenuators and selectable amplifier bypasses enable gain scaling such that the ADC range can be used in an SNR-optimal way with different field probes. The resulting overall adjustable gain of the receive chain is -1.7 to 79.5 dB. Again, 16 gain-scaling and filtering modules are connected to one motherboard. A programmable direct digital synthesis (DDS) module generates frequency-modulated excitation pulses of variable duration (typically 2 µs to 8 µs). Active

power splitters placed on the first-stage motherboard distribute these pulses to all 16 transmit PAs, which can boost them to a maximum output power of 3 W per channel. The whole system, except for the tuned field probes and the anti-aliasing filter at the ADC input, supports a large bandwidth of 50 MHz to 500 MHz and hence a wide range of field strengths and nuclei. The anti-aliasing filters can be selected through software from a set of filters, to fit the frequency range given by the magnet strength and monitoring nucleus. These settings can be different for different channels, permitting the simultaneous operation of field probes based on different nuclei.

Digitization / Decimation

Digitization and digital signal processing (digital signal processing stage in Fig. 2.1) is based on National Instruments (Austin, USA) hardware comprising NI 5761 14-bit ADCs sampling at 180 MHz to 250 MHz, NI 7961R FPGA modules for real-time demodulation, filtering, and down-sampling, and a host controller (NI 8133, NI 1082) for further signal processing, data visualization, sequence control, and data storage. Four channels are processed by each ADC and FPGA module resulting in a total maximum input data rate of 56 Gbit/s for 16 channels. Figure 2.2 depicts the implemented fixed-point I-Q demodulation, filter, and decimation chain composed of a shared DDS module for sine and cosine generation, high-speed multipliers, a cascade-integrate-comb (CIC) pre-decimation low-pass filter, and a finite-impulse-response (FIR) gain-compensation and decimation low-pass filter. The actual output data rate can be adjusted via the decimation rate and is typically set to 1 MHz (complex samples), which is amply sufficient for the gradient strengths of typical MRI systems.

The direct digitization approach simplifies the analog receiver design by removing the need for analog mixers, intermediate frequency filters, and potentially additional gain stages. Instead of a

low phase-noise local oscillator for mixing a low phase-noise digitization clock is required and the sampling frequency needs to be carefully selected together with the ADC input anti-aliasing filter in order to prevent unintended signal aliases. Any jitter or drift of the sampling clock results in a measurement error of the uniform (B_0) field component. An NI 6674T timing and synchronization module is used to generate the digitization clock with a jitter of 230 fs (200 MHz carrier, 10 Hz to 1 MHz carrier offset phase noise integration range) based on a 50 ppb/year reference oscillator.

Timing

A set of pulse generators, implemented on one of the FPGA modules, serves as sequence controller and generates all required control signals. Each sequence is typically started/synchronized with an external trigger signal from the MR system under test, followed by a configurable series of probe excitation-acquisition periods. The sequence controller operates on a 100 MHz clock which is phase locked with the digitization reference clock. This results in a sequence timing and external trigger synchronization resolution of 10 ns, which is considered adequate for most field measurement scenarios, since gradient chains are typically limited to bandwidths below 50 kHz. Figure 2.3 depicts a typical sequence of control signals, excitation pulses and acquisition intervals.

To use field measurements for image reconstruction, a common time base needs to be established between the field camera and the MRI system, accounting for receive chain delays and different sampling rates. For this purpose the two systems are synchronized by locking the cameras reference oscillator onto the reference clock of the MRI system. Delay calibration was achieved with an amplitude-modulated test signal transmitted into both receive chains during a synchronization scan. The difference in sampling rate was corrected by resampling the measured k-space trajectory according to the typically lower bandwidth of the raw imaging data.

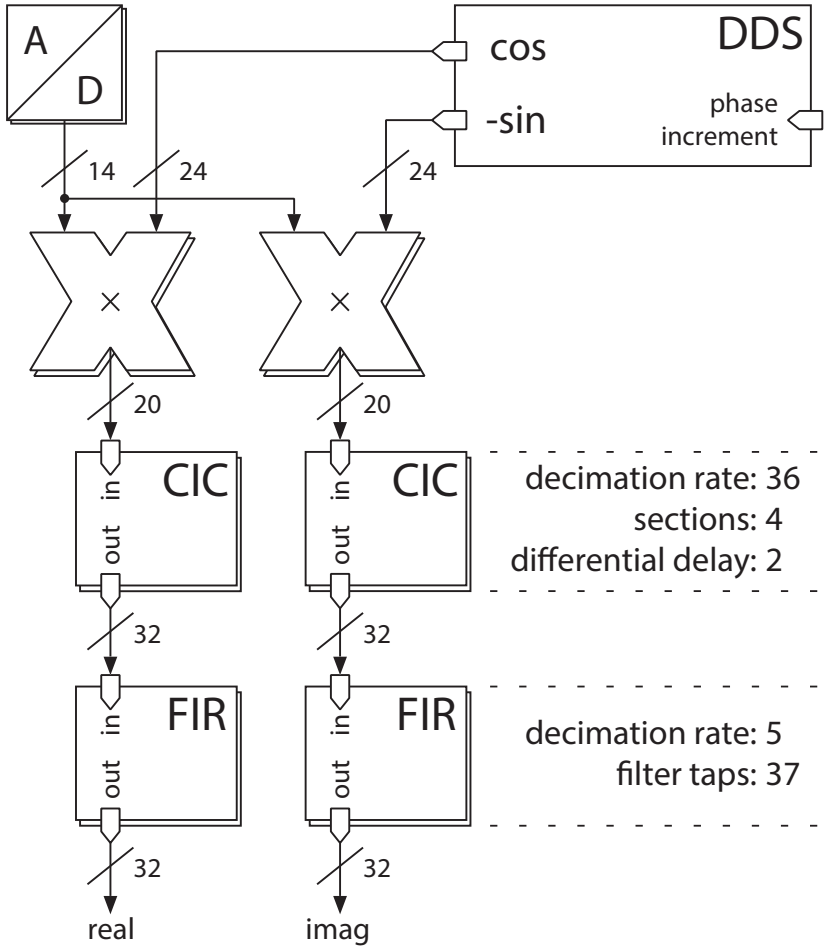

Figure 2.2: Digital real-time processing implemented on the FPGA modules. The digitized signals from each channel (14 Bit) are multiplied with a sine and cosine and decimated through 2 filter stages, yielding the complex raw data signal with a real and imaginary word width of 32 Bit each. Specifications of the implemented filters for 128 MHz operation are indicated.

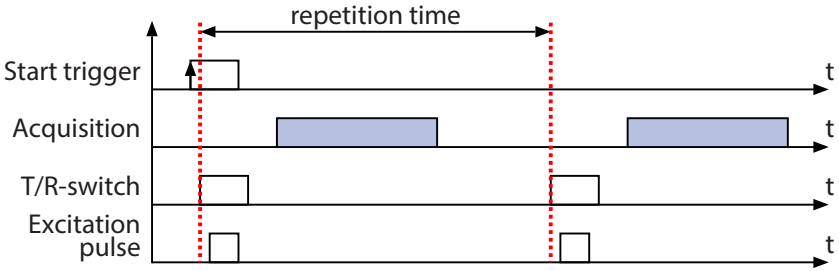

Figure 2.3: Control signal timing of a typical monitoring sequence. An external trigger from the MR system under test starts the probe excitation-acquisition sequence.

High-level signal processing

Following low-level signal processing on the FPGAs as described above, higher-level processing is performed on the controller CPU. It comprises extraction of the phase of the probe signals, unwrapping, and fitting to a third-order, real-valued, spherical-harmonic field model as described in Chapter 1.2.2 and Ref. [21]. The resulting time-varying phase coefficients reflect the global phase term (k_0), the familiar k-space coordinates (k_x, k_y, k_z), as well as second, and third-order components. The temporal derivatives of the phase time courses represent the spatially uniform field component, the familiar gradient field evolutions (G_x, G_y, G_z), and higher-order field contributions. At the level of phase and field coefficients, further filtering and down sampling can be performed to reduce noise and data size. The choice of final bandwidth depends on the highest frequencies of field variation that occur in the given MRI system. In the present work it was 50 kHz based on the observation that the gradient chains create the highest-frequency field dynamics.

2.2.2 Experiments

All measurements were performed in a whole-body Philips Achieva 3 T system (Philips Healthcare, Best, The Netherlands). Imaging experiments employed a commercially available 8-channel head receive array.

Receive chain performance

The digitizers signal-to-noise ratio (SNR), spur-free dynamic range (SFDR), and additive root-mean-square (RMS) phase jitter were measured using a reference signal from a SMA 100A signal generator (Rohde & Schwarz, Munich, Germany). The frequencies of the signal generator and receiver were set to 128 MHz, to simulate 3 Tesla ^{1}H operation. The resulting receiver output data rate was set to 1 MHz. Using 100 ms acquisitions, the additive RMS phase jitter was calculated by integration of the phase noise spectrum starting at a carrier offset frequency of 10 Hz and subtracting the phase noise of the reference signal generator, which was measured with an NI PXI-5660 vector signal analyzer. Third-order intermodulation distortion (IMD3) of the whole receive chain was measured by means of a two-tone measurement with a second signal generator (SMB 100A, Rohde & Schwarz, Munich, Germany). The second tone was set to a carrier offset frequency of 100 kHz. The two tones were fed into the T/R-module while the system was properly set up in the scanner bore at a combined signal level of -50 dBm, which is equivalent to the initial signal strength of a large ($>$2 mm diameter) field probe and hence represents a worst-case intermodulation condition.

Trajectory measurement and image reconstruction

The basic functionality of determining field dynamics during challenging gradient sequences was explored in examples of single-shot

EPI with uniform and variable speed [38] as well as an example of multiple-shot spiral scanning. The parameters of the uniform EPI readout were echo time (TE) = 25 ms, slice thickness = 2.5 mm, field of view (FOV) = 230 mm × 230 mm, resolution = 2.5 mm × 2.5 mm. The parameters of the variable-speed readout were TE = 35 ms, slice thickness = 1.8 mm, FOV = 230 mm × 230 mm, resolution = 1.8 mm × 1.8 mm, SENSE factor 3. For the spiral scan the parameters were TE = 1.4 ms, TR = 1.6 s, slice thickness = 3 mm, FOV = 228 mm ×228 mm, resolution = 1 mm × 1 mm, 8 interleaves. To employ measured k-space trajectories for image reconstruction, the camera measurement and the actual imaging procedure were performed in sequence, using synchronization as described above. B_0 and receive coil sensitivity maps were obtained with a common spin-warp gradient-echo sequence, performed with TE = 4.5 ms and TE = 6.8 ms and yielding 1 mm in-plane resolution. Image reconstruction was based on zeroth- and first-order results of the field measurements as well as the B_0 and sensitivity maps, using iterative algebraic reconstruction as described in Refs. [38], [45].

Mechanical vibrations

Field effects of mechanical gradient vibrations were examined in the following setting: Each gradient coil was separately driven to 35 mT m^{-1} for 100 ms and then switched off with the maximum slew rate, resulting in a steep, and approximately 200 µs long, gradient slope. The field camera was excited 70 µs before the slope onset to capture the switching event and ensuing field dynamics. Fields were studied in the time and frequency domains, including comparison with an acoustic spectrum obtained with a microphone.

Field drifts and external perturbations

Field fluctuations and drifts were studied with the following protocol: Initially, an EPI readout sequence with high duty cycle was played out on the scanner after being idle for several hours. The imaging parameters were chosen to reflect typical values used in functional MRI (fMRI) as follows: 2D single-shot gradient echo EPI with a TE of 35 ms, a FOV of 220 mm × 220 mm × 48 mm, 10 slices with an inter-slice gap of 2.5 mm, a voxel size of 2.6 mm × 2.6 mm × 2.5 mm, 400 dynamics with a slice TR of 3 s, and sequence TR of 300 ms, resulting in a total of 4000 EPI readouts in 20 min. After the EPI protocol the subsequent magnetic field evolution in the idle scanner was observed for 120 min, with a temporal resolution of 595 ms. This was realized by repetitive probe excitation with each excitation-readout cycle yielding one data point. Field coefficients for each data point were obtained by linear regression of probe phase time courses of 150 ms and subsequent transform into the basis of spherical harmonics.

2.3 Results

Table 2.1 shows the performance figures of the receiver module. The achieved probe sensitivity was assessed at $\xi = SNR\sqrt{BW} = 1.0 \times 10^5\sqrt{\text{Hz}}$ [20], resulting in an initial SNR of 40 dB at an acquisition bandwidth of 1 MHz, which is well below the receiver SNR, rendering the system probe-limited. Probe $T2^*$ was assessed as 65 ms. The maximum k-space range resulting from the probe droplet diameter of $d = 0.8$ mm was, according to Ref. [21], $k_{max} = (2.86\,\pi)/d \approx 11\,231\,\text{rad}\,\text{m}^{-1}$.

2.3.1 Sequence Monitoring and Image Reconstruction

A fully monitored single-shot EPI trajectory, including slice-selection and re-phasing gradients, is shown in Fig. 2.4. The scanner-

independent operation enables monitoring even during slice excitation, when the scanner is in transmit mode and typically not capable of acquiring any signal. Monitoring the large moments of the slice-selection gradients challenges the probes almost up to their de-phasing limits, which can be seen in the increased noise at around 1.5 ms. The close-ups show typical smoothing effects of the bandwidth limitation of the gradient system. Fig. 2.5 shows the corresponding measured 3D trajectory and excursions due to slice selection. A monitoring result for the case of variable-density EPI is shown in Fig. 2.6. In both cases the dynamics of the zeroth-order (k_0) component relate to eddy currents, which can be concluded from their temporal relationship to gradient switching. The drifting second-order terms, illustrated by the blue graphs in Fig. 2.4 and Fig. 2.6, most likely reflect concomitant-field effects, which depend on the squared magnitude of the readout gradient strength and hence drives over the whole readout into the same direction and has a smaller slope in the middle of the variable density EPI. The close-up in Fig. 2.6 nicely shows that the EPI blips end up having a tail due to the finite bandwidth of the gradient systems impulse response function. This is less critical in the imaging case since its integral and hence the distance between adjacent k-space lines is more important than the exact shape of the curve. Corresponding 2D trajectory, phantom and in-vivo images based on the measured variable-density trajectory, as well as spiral trajectories are shown in Fig. 2.7. The absence of perceivable ghosting and blurring in Fig. 2.7.D, 2.7.E and 2.7.F demonstrates consistency between the monitored trajectories and imaging data. Figure 2.7.G-I show corresponding images reconstructed using nominal trajectories. Figure 2.7.A shows one of the gradient echo images used for coil sensitivity and B_0 mapping, again reconstructed on the monitored trajectory.

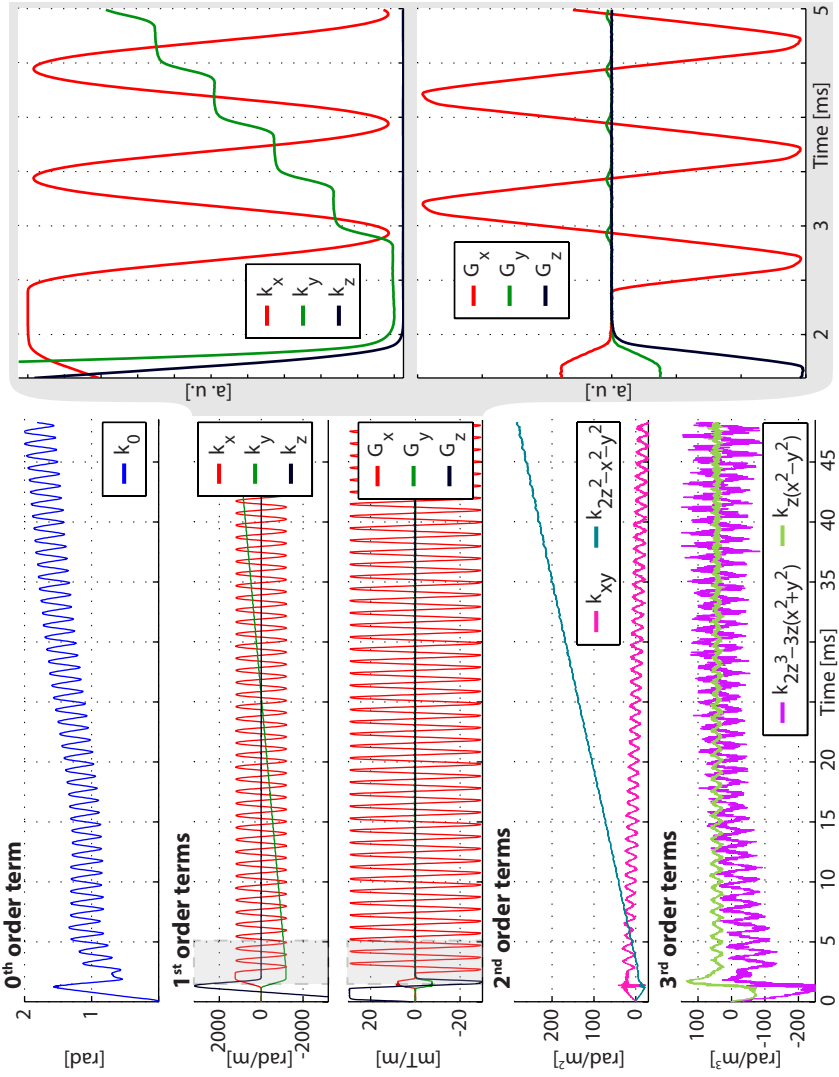

Figure 2.4: Fully monitored 2.5 mm × 2.5 mm × 2.5 mm voxel size, 230 mm × 230 mm FOV, single shot EPI, including slice selection and re-phasing gradients. Selection of the calculated phase coefficients in time domain at a bandwidth of 50 kHz, and zoomed excerpt of the first order coefficients and derivatives (gradients).

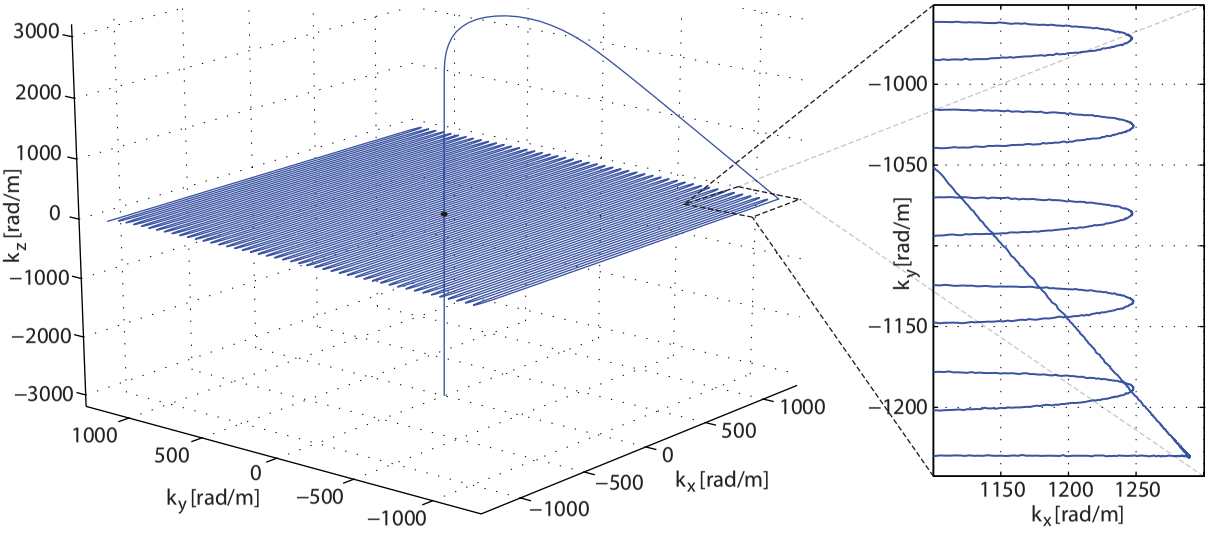

Figure 2.5: 3D k-space representation and zoomed excerpt at 1 MHz bandwidth of a fully monitored 2.5 mm × 2.5 mm × 2.5 mm voxel size, 230 mm × 230 mm FOV, single shot EPI trajectory including slice selection and re-phasing.

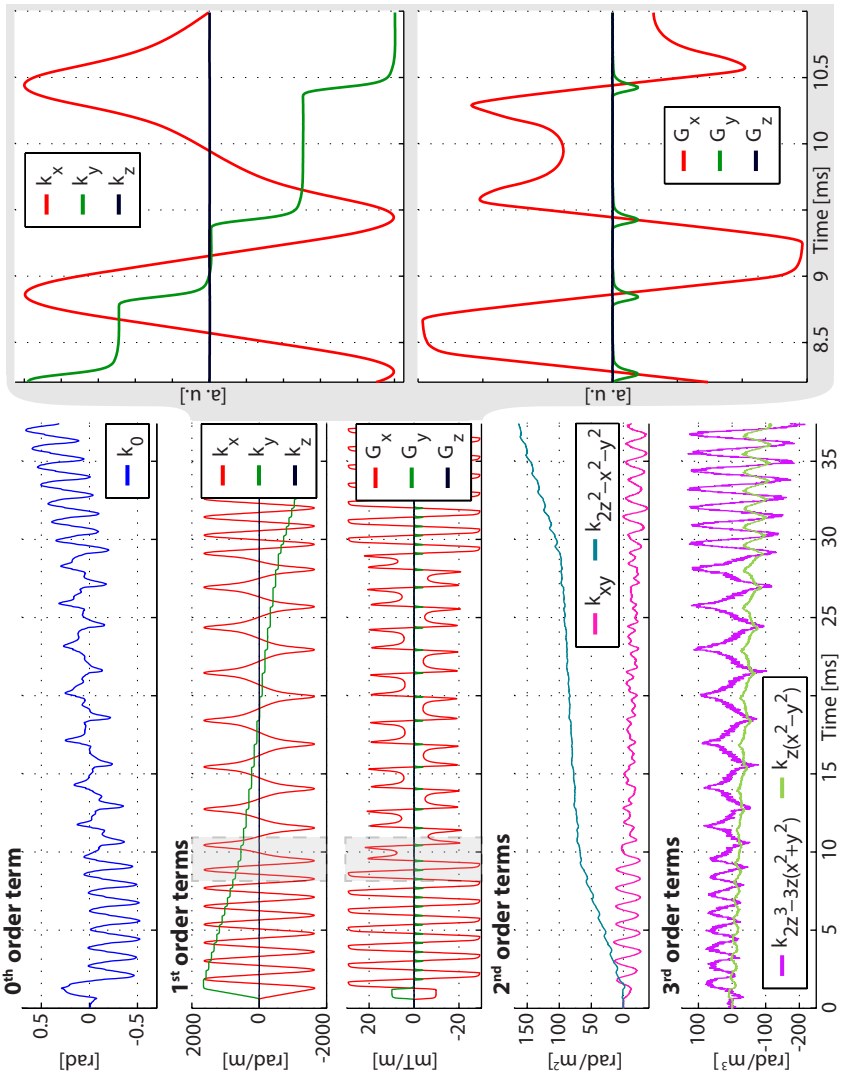

Figure 2.6: Monitored variable density (matched-filter) EPI, phase coefficients, gradient waveforms and zoomed excerpts of the 1st order fields.

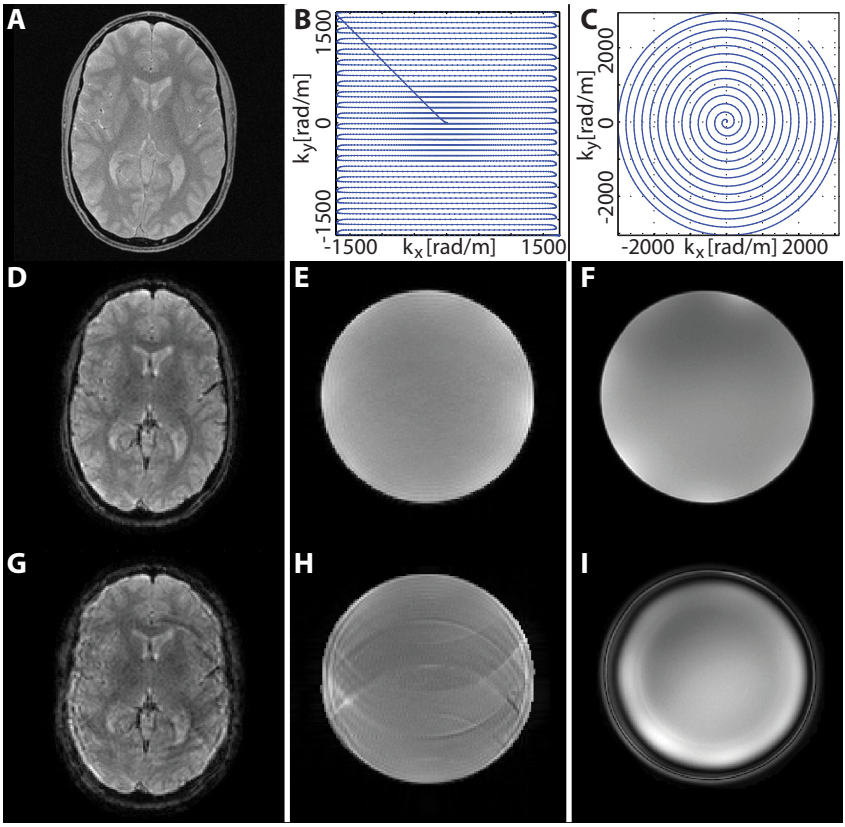

Figure 2.7: One of the gradient echo images used for coil sensitivity and B_0 mapping (A), monitored 2D accelerated variable density EPI trajectory (B), and interleave of the monitored spiral trajectory (C). In-vivo (D) and phantom (E) image reconstructed with the monitored variable density EPI trajectory, phantom image reconstructed with the monitored spiral trajectory (F), and images reconstructed with the corresponding nominal trajectories given by the sequence (G,H,I).

SNR (1 MSPS)	82.2 dB
SFDR (1 MSPS)	96.7 dB
Additive RMS phase jitter of the digitizer (1 MSPS, 10 Hz offset)	230 fs
Third-order intermodulation distortion (IMD3)	74.7 dB
Noise figure 1st stage	0.9 dB
Gain 1st stage	22.1 dB
Noise figure 2nd stage	2.3 dB
Gain 2nd stage	−23.8 to 57.4 dB

Table 2.1: Receiver performance results (128 MHz operation).

2.3.2 Mechanical Vibrations

Fig. 2.8 shows time evolutions and corresponding frequency domain components of the first order phase coefficients during and following a steep gradient turn-off event. The zoomed plot (Fig. 2.8.C) of k_z shows a distinct oscillation at 1298 kHz with an amplitude of approximately 0.75 rad m^{-1} and a decay time of approximately 15 ms, while the other coefficients (Fig. 2.8.B) appear to be mostly affected by rather slow eddy currents. A comparison with the acoustic spectrum (Fig. 2.8.D-E) confirms the mechanical nature of the observed oscillation.

2.3.3 Field Drifts / Fluctuations

Intensive gradient duty cycles heat-up the scanner, which can cause field drifts. Fig. 2.9 shows the field evolution of an idle scanner over a period of 2 h right after a demanding fMRI scan session. Several effects can be observed, such as disabling of the shim system at around 2 min, a B_0 drift with a decay constant of approximately 15 min, fluctuations due to the cryogenic pump, fluctuations due to trams passing close to the MR system site, a repeatable change in

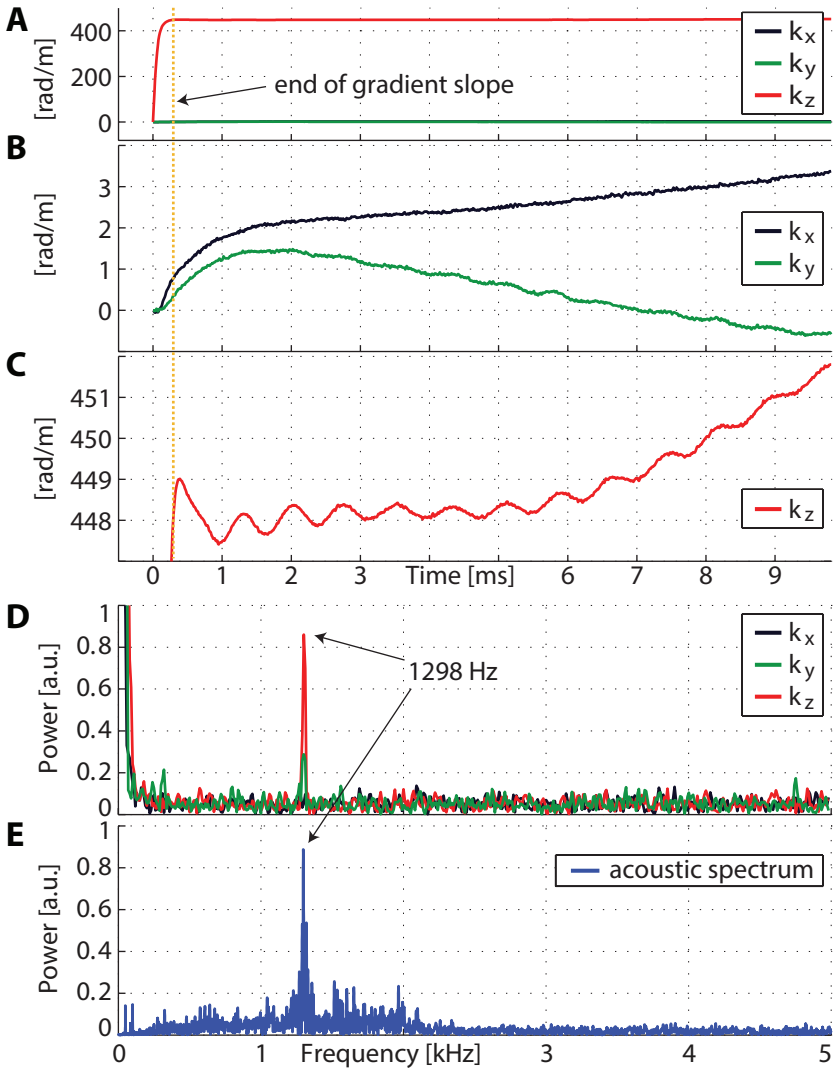

Figure 2.8: Dynamics of the 1st order phase coefficients during and after a steep z-gradient slope (A: all 1st order coefficients, B and C zoomed), as well as corresponding frequency domain representation (D) and acoustic spectrum of a microphone (E).

almost all field orders at around 94 min, and many more. The effect of the cryogenic pump is mostly visible in the B_0 and G_y terms, where it appears like an increased noise level. The power spectrum of the B_0 term in Fig. 2.9.B reveals an alias of the pumps primary acoustic frequency component, which cannot directly be resolved due to the limited time resolution of 595 ms. Shortening this time is possible but can lead, given the relaxation times of the used field probes, to spurious echo formation. A rather regular pattern of disturbances following roughly the 7 min schedule of the public transport system can be seen in the first and second-order terms. The B_0 term does not show these disturbances, which is most likely due to the shielding effect of the super-conducting magnet. The 94 min glitch is most likely due to a change in the operation mode of the scanner, such as shutdown of the gradient cooling system.

The measured field noise (Fig. 2.9) is in the range of 2.5 nT for the zeroth, 7.5 nT m^{-1}for the first, 19.3 nT m^{-2} for the second, and 124 nT m^{-3} for the third order terms (averaged over all components of each order). The field measurement sensitivity of the probe array can be calculated by extending the thermal noise based field sensitivity approximation from [20, equation 10] with the noise propagation due to the spatial field-model from [21, equation 8] yielding:

$$\sigma_{\mathrm{B}_l} \approx \frac{\sqrt{6}}{\gamma \xi T_{obs}^{3/2}} \sqrt{\sum_j \left(P_{l,j}^{+}\right)^2}. \tag{2.1}$$

In other words, the probe phase noise is scaled by the magnitude of the corresponding row of the pseudo-inverse of the probing matrix, which reflects the probe position calibration in terms of the used basis functions. This results using an observation time of 150 ms - in 2.6 pT for the zeroth, 55 pT m^{-1} for the first, 1.3 nT m^{-2} for the second, and 20 nT m^{-3} for the third-order terms. The same calculation based on the sensitivity due to the additive jitter of the receiver (Table 1) gives 68 fT for the zeroth, 1.4 pT m^{-1} for the

first, $33\,\mathrm{pT\,m^{-2}}$ for the second, and $543\,\mathrm{pT\,m^{-3}}$ for the third-order terms. The measured noise is hence roughly 3 orders of magnitude higher than the theoretical sensitivity, which is also roughly 3 orders of magnitude higher than the noise due to the receiver. This suggests that the measurement is field noise limited.

2.4 Discussion

We introduced a stand-alone system for dynamic magnetic field monitoring, delivering camera-like access to field dynamics in MR systems, with high temporal resolution and sensitivity in the nanotesla range. The implemented system was evaluated at 3 T, delivering insights into otherwise poorly accessible field dynamics such as slice excitation, effects of mechanical vibrations, eddy currents, and magnet cool-down. The accuracy of the monitored trajectories proved suitable for challenging variable density EPI image reconstructions.

The current implementation allows for real-time field monitoring and visualization up to a duty cycle of 25 % with a probe re-excitation period of roughly 600 ms, given the relaxation times of the used field probes ($T_2^* = 65\,\mathrm{ms}$) and a very conservative level of accepted spurious coherences from previous excitations.

A comparison of measured field noise with the theoretical values based on the sensitivity of the probes and the receiver revealed that the measurements are limited by actual field noise.

Since the field probes measure the magnitude of the magnetic field, it is expected that the derived spatial field distributions deviate from the main magnet axis due to concomitant fields of the gradient system. This is typically not a problem since the imaging sample is also subject to these deviations. If required, this could be circumvented by an increased number of probes and optimized basis functions for concomitant fields, as well as an optimized spatial probe positioning. Another approach could be analytical calcula-

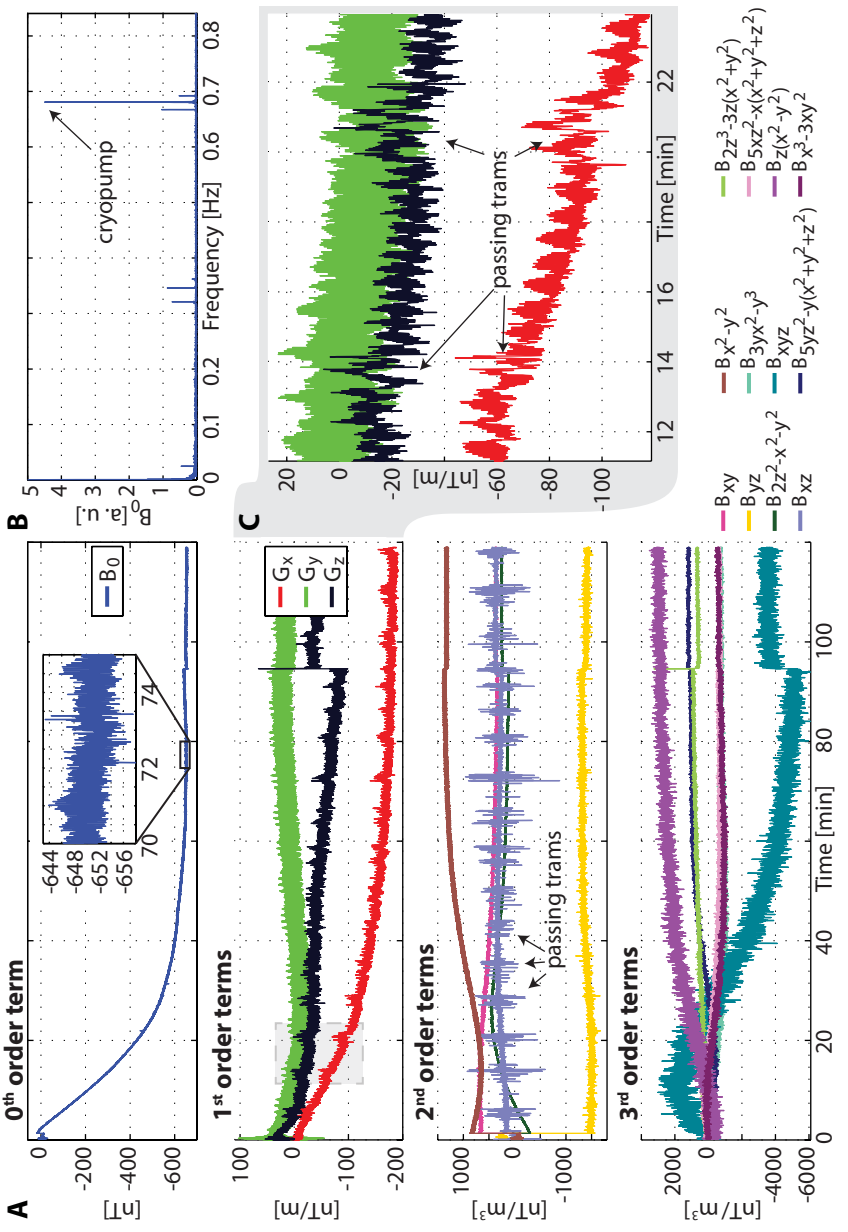
A
0th order term
[nT]
B0
-644
-648
-652
-656
70
72
74
1st order terms
[nT/m]
Gx
Gy
Gz
2nd order terms
[nT/m²]
passing trams
3rd order terms
[nT/m³]
Time [min]
B
B0 [a. u.]
cryopump
Frequency [Hz]
C
[nT/m]
passing trams
Time [min]
Bx²-y²
B3yx²-y³
Bxyz
B5yz²-y(x²+y²+z²)
B2z³-3z(x²+y²)
B5xz²-x(x²+y²+z²)
Bz(x²-y²)
Bx³-3xy²
Bxy
Byz
B2z²-x²-y²
Bxz

Figure 2.9: Field evolution of the idle scanner over a period of 120 min, starting right after a 20 min fMRI scan (A). Power spectrum of the 0^{th} order component (B), and zoomed excerpt of the 1^{st} order components time evolution (C).

tion of the expected concomitant fields and retrospective correction of the phase evolutions.

Direct sampling and FPGA-based real-time data processing render the proposed system flexible and easily adjustable to different requirements. Scalability in terms of number of channels, support for different scanner vendors, field strength, and nuclei, is designed into the modular receive, excitation, and data processing chains. Filters and bandwidth can be changed without hardware modifications, and processing steps can be moved to the FPGAs to increase performance for real-time field monitoring applications. Its flexible nature, ability to acquire data with a duty cycle of up to 100 % over arbitrary durations, only limited by the hard disk size, its real-time field data processing capabilities, modular interfaces, and scalable design, make it useful for a whole range of other applications such as impulse response based gradient and shim system characterization [41], [42]. In conjunction with a switch to another nucleus, the system can be transformed from a pure analysis and characterization instrument into an active field controller for real-time field stabilization, as has been shown by [32], [33]. A whole range of other applications might profit from these capabilities, for example field probe based motion correction [40] or other concurrent monitoring and imaging modalities [39].

3 Concurrent Gradient and RF Pulse Monitoring

Partially published in:

- *"A stand-alone system for concurrent gradient and RF sequence monitoring".* Dietrich, Benjamin E.; Brunner, David O.; Barmet, Christoph; Wilm, Bertram J.; Pruessmann, Klaas P. *In Proceedings of the Annual Meeting of ISMRM*, Melbourne, Australia, 2012. Abstract 700.
- *"Concurrent Monitoring of RF and Gradient Waveforms of Parallel Transmission Pulses by a Field Camera".* Brunner, David O.; Dietrich, Benjamin E.; Cavusoglu, Mustafa; Barmet, Christoph; Wilm, Bertram J.; Pruessmann, Klaas P. *In Proceedings of the Annual Meeting of ISMRM*, Salt Lake City, Utah, USA, 2013. Abstract 293.
- *"Automatic Reconstruction of Gradient Echo Imaging Sequences by Concurrent and Continuous Monitoring of Gradient and RF Waveforms".* Brunner, David O.; Dietrich, Benjamin E.; Barmet, Christoph; Gross, Simon; Wilm, Bertram J.; Pruessmann, Klaas P. *In Proceedings of the Annual Meeting of ISMRM*, Salt Lake City, Utah, USA, 2013. Abstract 553.
- *"Concurrent Recording of RF Pulses and Gradient Fields – Comprehensive Field Monitoring for MRI".* Brunner, David O.; Dietrich, Benjamin E.; Cavusoglu, Mustafa; Wilm, Bertram J.; Schmid Thomas; Gross, Simon; Barmet Christoph; Pruessmann, Klaas P. *NMR in Biomedicine*, 2015. DOI 10.1002/nbm.3359.

3.1 Introduction

Magnetic field monitoring using NMR probes allows observation of the spatio-temporal evolution of low-frequency (longitudinal) encoding fields and field disturbances with high precision, as demonstrated in Chapter 2 and [20], [21], [24]. However, for correct MR

signal formation, accurate, stable, and precisely timed transverse RF fields are of equal importance, especially towards ultra-high field applications employing parallel imaging [13]–[15] and parallel transmission [8], [46] techniques. Furthermore the accuracy of the applied RF waveforms has direct implications towards subject safety [47], [48].

Especially temperature, environmental, and subject induced field alterations are difficult to manage and call for concurrent observation of the low-frequency, as well as high-frequency field dynamics (gradient and RF pulses respectively) during imaging experiments.

So far RF pulse monitoring required separate pickup coils [49] or current sensors [50] and NMR field probe operation was not possible during high-power RF pulse transmissions due to strong RF coupling, saturating or even destroying the field probe's receive chains.

The proposed solution presented in this Chapter enables the previously introduced stand-alone monitoring system (Chapter 2) to operate during high-power RF pulses and to simultaneously acquire their waveforms without additional pickup coils or current sensors. Therefore ^{19}F-based field probes are used, providing spectral separation between low-frequency field monitoring and RF pulse monitoring. The same field probe's electronics serve as pickups for the high-power RF pulses and subsequent frequency selective signal scaling in the receive chain ensures that both frequency bands can be acquired simultaneously without the risk of destruction or operation in a non-linear regime.

Spatial expansion of the longitudinal low-frequency field dynamics [21] can typically be achieved with a reasonable number of field sensors, since these fields originate primarily from sources relatively far from the imaging volume as elaborated in Section 1.2.2. This is not the case for the RF pulses. Currents and dielectrics in the sample represent driving terms within the imaging volume, precluding spatial interpolation of the field. However, the temporal

dynamics of the RF pulses, which drive currents in the different RF coils, can be captured and related to B_1^+ maps.

Measurement of the RF pulses and gradient waveforms on a common time basis delivers a comprehensive view of all external field dynamics driving the spin system. Thus the exact timing of the imaging experiment's spin coherence with respect to the trajectory becomes apparent.

Examples of balanced steady-state free precession (bSSFP), ultrashort echo time imaging (UTE) and spatially selective parallel transmit pulses are used to demonstrate the functionality of the proposed system.

3.2 Methods

3.2.1 Imaging System

All measurements were performed on a Philips Achieva 7 T MRI system (Philips Healthcare, Cleveland Oh, USA), equipped with a single 4 kW transmit channel and an 8 x 1 kW parallel transmission extension (Philips Research Laboratories, Hamburg, Germany). All sequences were executed with standard parameters and power settings. A head volume resonator (Nova Medical Inc., Wilmington, Ma, USA) was employed for single channel experiments, and an 8-channel loop array (Rapid Biomedical, Rimpar, Germany) was used for multichannel transmission.

To prevent the MRI system's broadband RF power amplifiers from emitting noise in the fluorine frequency band, which couples into the sensitive high-gain receive electronics of the monitoring system, high-power compatible bandpass filters were added at the amplifier output. These filters were based on an interdigital design, using quarter-wavelength copper-rods, as presented in Ref. [51]. This design was adapted by simulation with ANSYS HFSS (ANSYS, Inc., Canonsburg, Pennsylvania, USA). Figure 3.1 shows the

resulting filter design and performance.

3.2.2 Monitoring System

The stand-alone field camera presented in Chapter 2 and Ref. [52] formed the basis of the used monitoring system. Several modifications were applied to make it fully operational during high-power RF transmissions of the MRI system. These modifications comprise the field probe array, frequency selective signal scaling and dual-band demodulation. Figure 3.2 shows a schematic of the extended monitoring system and its building blocks.

Field Probes

NMR field probes built from 1.7 mm inner diameter glass capillaries, as exemplified in Section 1.2.1 and Refs. [20], [30], [31], filled with a hexafluorobenzene compound were used. 16 such probes, with signal life times of about 40 ms were arranged on the inside of the MRI system's RF transmitters, equally distributed on two transverse rings with a diameter of about 22 cm. The distance between the rings was approximately 15 cm. The probes were operated in parallel to the MR sequence under test, as described in Chapter 2.2.1.

RF Pulse Sensing

RF pulse sensing was based on coupling between the MRI system's transmitters and the RF lines of the field probe array. Even though the field probes were tuned to the fluorine frequency (≈ 280 MHz at 7 T), signal levels of the RF pulses induced by the MRI system (≈ 298 MHz for ^{1}H at 7 T) were found to be to high for the field probe's sensitive receive chains. In order to prevent destruction of the receive chain circuitries, the probeheads where equipped with gradient compatible RF shields. However, the levels of the

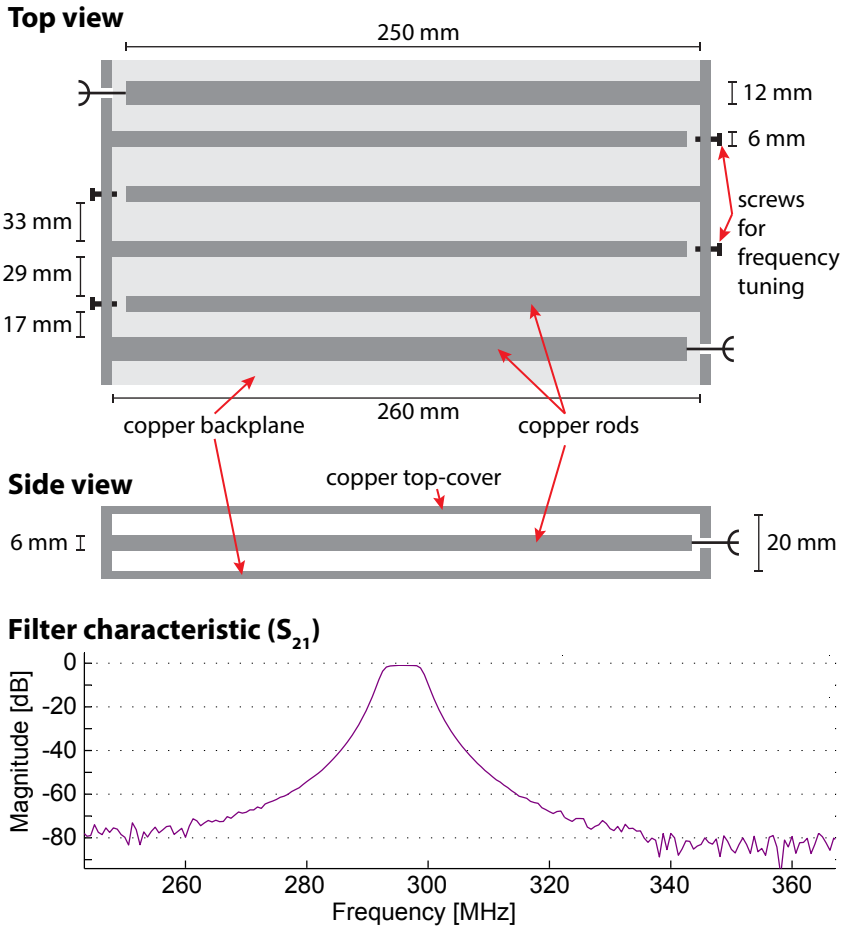

Figure 3.1: Construction and S-parameter of the high-power band-pass filters inserted into the MR system's transmit chain.

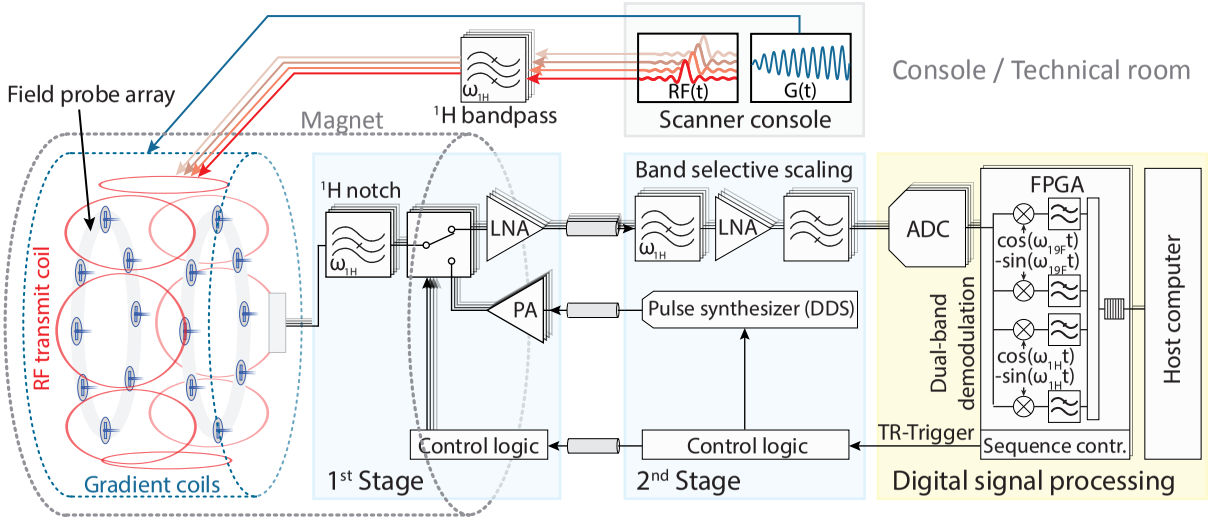

Figure 3.2: a) Block diagram of the employed setup with the scanner console driving the sequence and the monitoring spectrometer acquiring the longitudinal field dynamics encoded on the fluorine band and the RF pulses in the proton band.

induced signals were still found in a range that would cause saturation and nonlinearities, resulting in signal distortion. Therefore, coaxial stub-line notch filters as shown in Fig. 3.2 were introduced before the preamplifier and the second stage amplification in order to prevent saturation of the subsequent gain stages and to provide comparable signal levels in both bands to the converters. The SNR critical first stage filters had an insertion loss of about 0.8 dB in the ^{19}F band and a rejection of 20 dB in the ^{1}H stop band (Fig. 3.3.A). To avoid strong dependence of the isolation on the cable length of the field probes, these filters were built such that they provide a $50\,\Omega$ matched input impedance in both bands, realized by a terminated diplexer structure. The second stage filters, built with a similar topology (Fig. 3.3.B), provided a reflective rejection of about 40 dB and had an insertion loss of 1.2 dB.

After passing through the receive chains and broadband digitization (14 bits, 250 MSPS), the RF pulses and probe FID's were separated by dual-band demodulation and application of strongly band selective digital filters. Two sets of in-phase and quadrature demodulators were therefore implemented on the field programmable gate arrays (FPGA), one for each frequency band, to retrieve complex baseband signals at rates of 1 MHz each.

Immunity of the fluorine receive lines to the high power transmission has been validated by testing that a full power pulse at the proton frequency does not raise the noise floor of the fluorine acquisition, nor distort the received FID. Therefore, FIDs were acquired concurrent to a sinc-gauss pulse of maximum peak amplitude and checked if it affects the resulting signal. Further the effect of the bandpass filters, inserted in the transmission path of the scanner, was checked.

High-Level Signal Processing

In order to correct for delay differences in the ^{1}H and ^{19}F frequency bands, all filter components and field probes were charac-

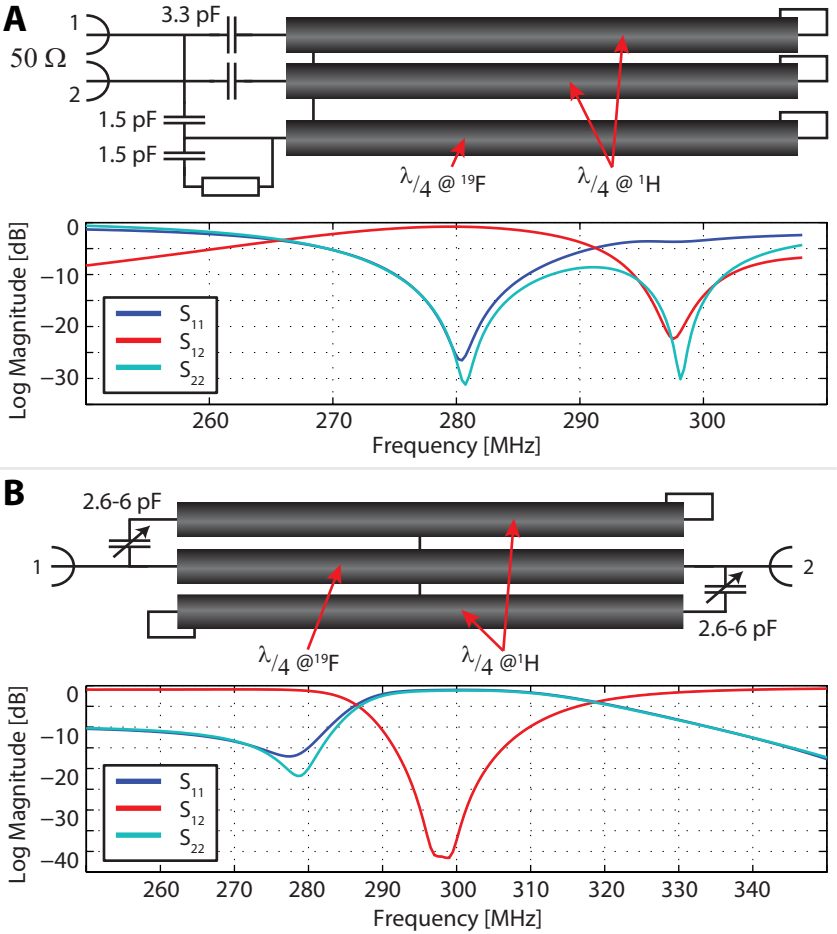

Figure 3.3: A: Construction and S-Parameters of the filter protecting the low noise preamplifier from saturation during high power transmission. This filter exhibits low reflections towards the probe (port 2) in the ^{1}H and ^{19}F frequency bands. B: Construction and S-Parameters of the reflective coaxial notch filter used for band selective scaling in order to reduce the signal in the ^{1}H band to similar dynamic ranges as the ^{19}F signals.

terized by network analyzer measurements (ENA50613, Agilent, Santa Clara). The group delay was found to be dominated by the resonant solenoid detector loop (80 ns) and the notch filters (first stage −120 ns and −130 ns for the second stage). Thus signals in the proton band were shifted and resampled by 170 ns using a fractional delay Farrow filter [53].

After spatial field expansion according to [21], k-space trajectories and gradient waveforms were filtered to 50 kHz using a delay compensated FIR filter. The RF pulse waveforms were decomposed into amplitude (AM), phase (PM) and frequency (FM) modulation and subsequently filtered to 100 kHz. The FM modulation represents the center frequency of the pulse as found by the center-of-mass of its spectrum. Phase jumps of π were attributed to the AM in order to make the pulse waveforms more readable. All calculations were implemented in custom routines using Matlab (Mathworks, Natick, MA, USA).

Calibration

Probe positions for 1$^{\text{st}}$-order spatial field expansion of the low frequency field dynamics were calibrated using the field patterns of the main magnet, x, y, and z gradient coils. Fields, determined in 4 ms intervals, with the magnet at rest and under 2.5 mT m^{-1} gradients were used to calculate the positions in the gradient coordinate system. The local fields were determined with a linear fit on the phase evolution of each probe's FID, 1 ms after probe excitation. A 300 ms long delay was inserted between the gradient ramp-up and probe excitation to make sure that all fields were settled.

In order to map the received RF waveforms (B_p^1), to currents (j_c^1) driving the individual coils of the multichannel transmit system, a coupling matrix $\mathbf{A}$ was determined by sequentially playing out block pulses with each transmit channel. Superscript 1 indicates transverse field component, subscript p the probe index, and

subscript c the coil index. Initial tests revealed that coupling was noticeably frequency (ω) dependent within the bandwidth of the excitation pulses and consequently the calibration matrix entries had to be considered over the entire transmission band (tilde indicates Fourier transform):

$$\tilde{B}_p^1(\omega) = \sum_c \left(\tilde{\mathbf{A}}(\omega)\right)_{p,c} \cdot \tilde{j}_c^1(\omega), \tag{3.1}$$

$$B_p^1(t) = \sum_c \left(\mathbf{A}(t')\right)_{p,c} * j_c^1(t''). \tag{3.2}$$

Therefore block pulses of 0.7 ms duration where played out sequentially with each channel, stepping the carrier frequency by 40 kHz to cover a total bandwidth of 200 kHz. Since the frequency dependence of the coupling ($\tilde{\mathbf{A}}(\omega)$) turned out to be very smooth within the band of the RF pulses, it could be interpolated in the frequency domain with a second order polynomial (1024 points). Short time domain kernels were then generated by fast Fourier transformation, and the waveforms mapped to the coils using:

$$j_c^1(t) = \sum_p \mathcal{F}^{-1}\left(\left(\tilde{\mathbf{A}}(\omega)^+\right)_{c,p}\right) * B_p^1(t), \tag{3.3}$$

where $\tilde{\mathbf{A}}(\omega)^+$ denotes the pseudoinverse of $\tilde{\mathbf{A}}(\omega)$ and $\mathcal{F}^{-1}$ the inverse Fourier transform.

The accuracy of the obtained calibration was verified by checking for a correct reconstruction of the pulse waveform of a calibration pulse series with a center frequency of 0 kHz, which has not been previously acquired for calibration. As a further test case each channel of the transmit array was requested to play out a sinusoidally amplitude modulated pulse with the modulation frequency set such that the number of cycles inside the acquisition window is equal to the channel number.

When using such a broadband calibration, one has to bear in mind that the system behaviour is calibrated to the recorded calibration pulses. The obtained pulse waveforms reflect the physical measurement of the fields inside the scanner only if the spectral behaviour is dominated by the response properties of the measurement system. This is clearly the case in the presented system because typically the RF coils' frequency response are much broader than the ones of the sensors' circuits and especially than that of the employed filters for frequency selective signal scaling.

3.2.3 Monitored Sequences

For demonstration a 3D ultra-short echo time sequence [54] (TR = 6.2 ms, TE = 0.14 ms, 1.25 mm isotropic resolution) and a 3D balanced steady-state-free-precession (bSSFP/true FISP) sequence (TR = 6.2 ms, TE = 3.2 ms, 1.25 mm × 1.25 mm × 4 mm resolution) were monitored using the scanner in the single transmit channel configuration. Due to the signal decay and the required deadtime before re-excitation of the field probes, only excerpts of 30 ms were measured every 400 ms.

Accelerated, spatially selective pulses were recorded using the 8-channel transmission extension. First a 5.3 ms spatially selective spiral with a field of excitation of 12.8 cm and a 4 fold acceleration was designed as described in [55] and played out prior to a 3D Cartesian readout (TE/TR 4.5/100 ms, resolution 2 mm × 2 mm× 4 mm). Further a 7-spoke 2D selective excitation pulse [56] was monitored.

3.3 Results

The immunity tests in Figure 3.4 show a raised noise floor in the ^{19}F band during unblanking of the power amplifier of the MRI system, however the acquired FIDs are not distorted or modulated

even by a pulse with full peak power. Hence the increased additional noise originates from the high in-band output noise level of the power amplifier, coupled into the field probes' receive lines. The high-power compatible bandpass filters, inserted before the RF coils, blocking the noise at the ^{19}F frequency, resolved the issue. Although the noise of the power amplifier decreases the SNR of the field probes during the unblanking time, the found noise level is too low in order to nutate the excited spin coherence in the probes. Therefore, given that the phase of the field probe's FIDs could be unwrapped, the measurement of the k-space trajectory would not be affected once the power amplifier of the MRI system is blanked again, even if the high power RF signals would not be filtered. Since the power amplifier usually is blanked during acquisition intervals of the MRI system, the k-space trajectory could still be acquired with equal quality during readouts. However, when measuring the field evolution during RF transmission the SNR would be degraded.

Fig. 3.5 shows data of the RF calibration. The signals acquired by each receiver of the monitoring system clearly show distinct coupling constants for different transmit channels when playing the calibration pulse train (Fig. 3.5.A). The frequency dependence of the resulting calibration coefficients is shown in Fig. 3.5.B and their smoothness justifies the low order interpolation for calculation of the convolution kernels. In Fig. 3.5.C the resulting waveforms of each transmitter (colour coded from blue to brown) is shown, reconstructing a pulse train played at 0 kHz (which was not acquired for the calibration), using the broadband calibration. The effect of the broadband calibration becomes apparent when comparing this result to plot Fig. 3.5.D which shows the same pulse train reconstructed by calibrating only at 20 kHz and ignoring the frequency dependency. As the close-up of the signal floor plotted below shows, the broadband calibration significantly improves the specificity of the reconstruction isolating the signals from the dif-

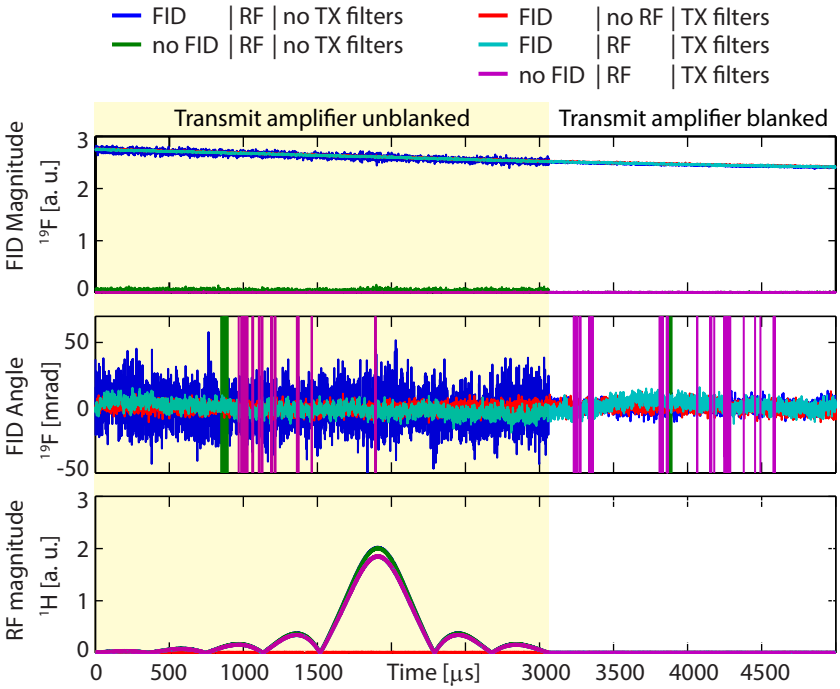

Figure 3.4: Immunity testing of the acquisition in the fluorine band towards high power transmission in the proton band. The acquisition of the ^{19}F FID is not affected in magnitude and phase by intermodulation or compression effects. However the high thermal noise floor of the power amplifier increases the noise floor in the fluorine band. Filtering the transmission lines stops the noise in the fluorine band.

ferent transmit channels. Further Fig. 3.6.A shows the waveforms recorded by each probe channel and Fig. 3.6.B the reconstructed pulse waveform of each channel of the transmit array. The individual amplitude modulations are very well obtained with no visible sign of distortion or signal misallocation between the traces of the different transmit channels.

Figure 3.7 shows the resulting k-space trajectory, gradient and RF waveforms of the monitored UTE sequence. The k-space origin was set to the centre of the block pulse in correspondence to the sequence. The RF waveform of the block pulse exhibits a slight ramp.

Figure 3.8 shows the monitoring results for the trueFISP/bSSFP sequence showing several repetition times acquired in one shot. Almost the full coherence life-time of the sensors could be used to track the gradient waveforms of the system even during the RF pulses because the probes were excited in the magnetic centre of the RF pulses and were hence refocused by the sequence. Further the phase alignment of the pulses could clearly be observed.

The results obtained from the multichannel excitation pulses are shown in Fig. 3.9 and Fig. 3.10. For these plots, the k-space origin was set to the end of the RF pulse, which allows monitoring the excitation and the read-out k-space trajectory seamlessly. The exemplary comparison of the measured and the demanded waveform show good correspondence. The conditioning of the RF calibration matrices was found to range between 10 and 20 depending on probe positioning. Lower condition numbers could be achieved by placing the probes closer to the transmitting element (being currently held on 2 cm spacers). However this would presumably affect the accuracy of the longitudinal field measurement by catching magnetic fields induced by local eddy currents running on the coils conductive structure and could potentially impair the function of the coil.

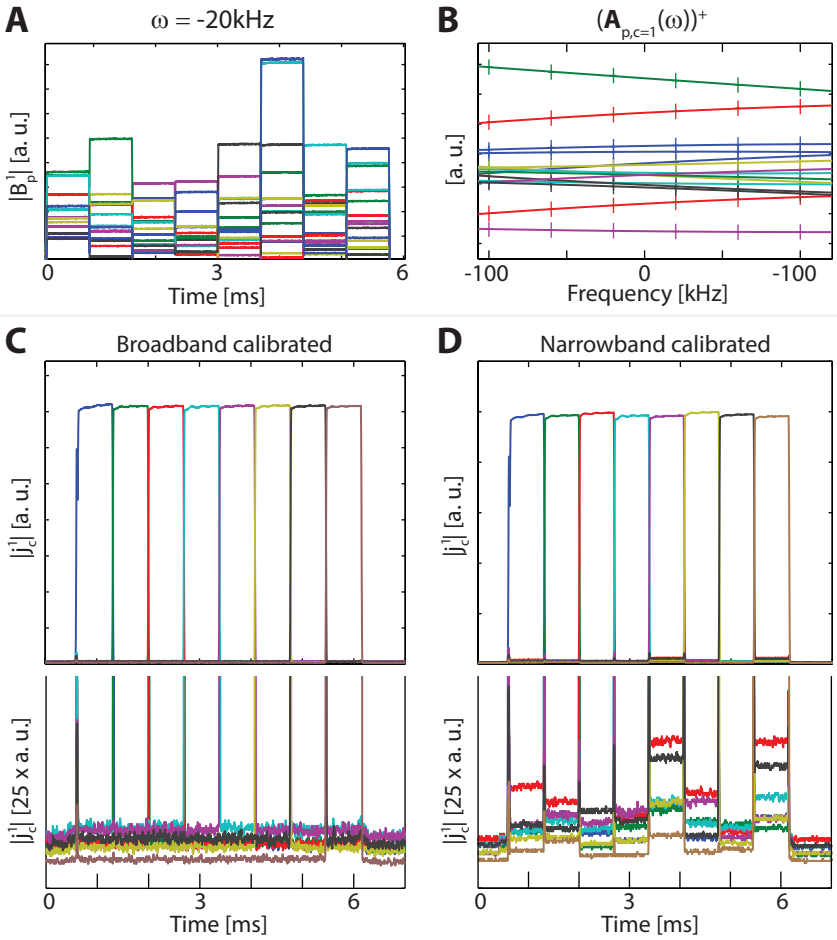

Figure 3.5: Calibration of the sensor array for multi-channel transmission systems. A: Calibration pulse train playing a block pulse with each Tx channel as recorded with the probe array (magnitude plotted). B: Frequency dependence of reconstruction coefficients. C & D: effect of frequency dependent calibration on monitored results. As shown by the magnification of the signal floor below, the seperation of the individual Tx channels is significantly improved.

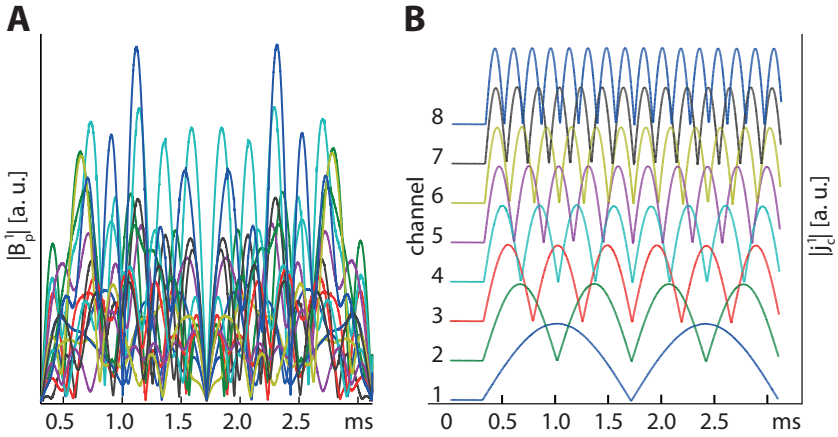

Figure 3.6: A: signal received when each Tx channel plays a sinusodial AM modulation with different modulation frequency. B: Magnitudes of reconstructed waveforms from e) showing clean separation of the pulses in each Tx channel.

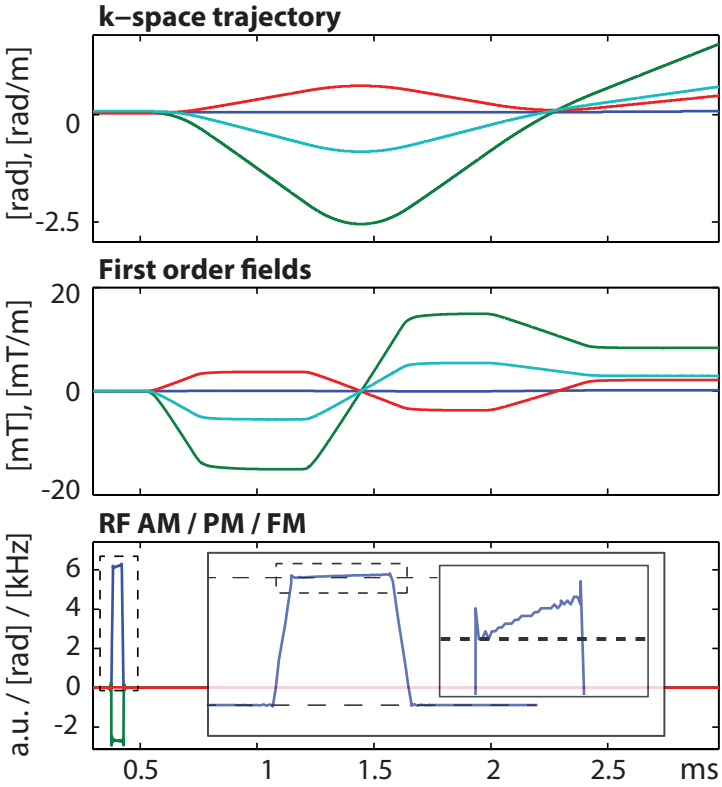

Figure 3.7: Monitoring result showing a single repetition of a UTE acquisition measured with the single channel transmit coil. k-space trajectory (top), corresponding gradients (middle) and the RF pulse (bottom). The color coding for the k-space and the gradient components is dark blue (0^{th} order), red (x), light blue (y), and green (z). RF waveform AM (blue), phase (green) and frequency (red). The close-ups of the RF pulse show the rise and fall time, as well as a minute transient on the plateau.

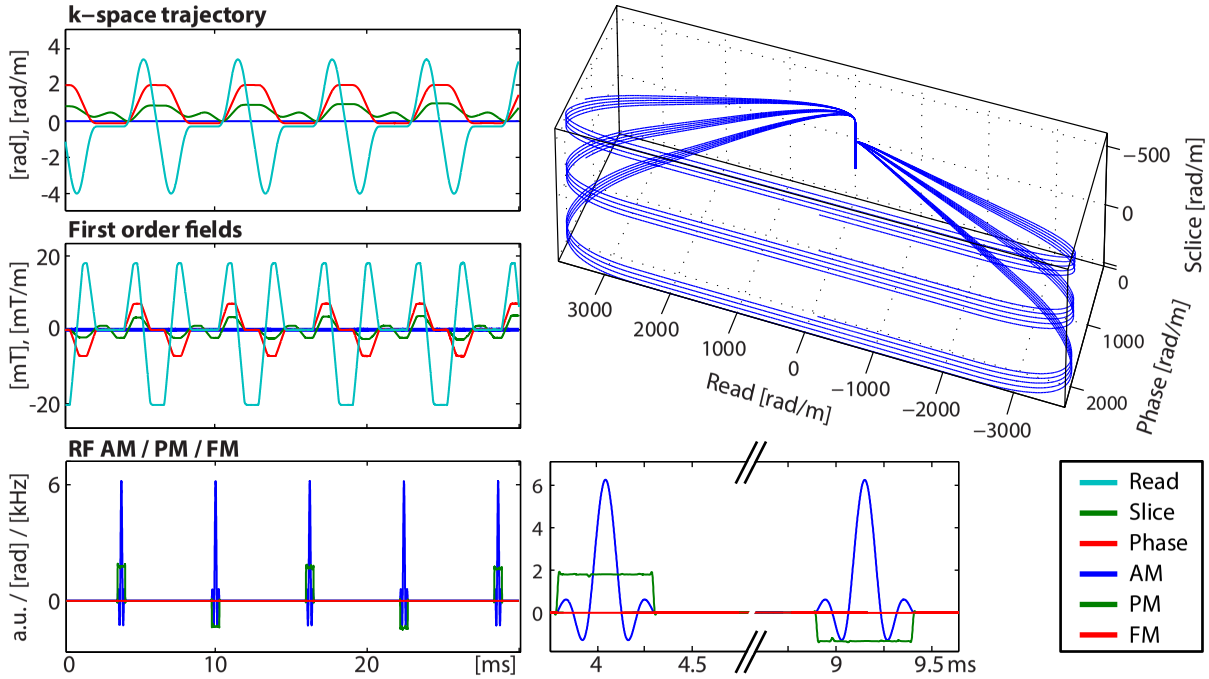

Figure 3.8: Monitoring results retrieved from the single channel transmit coil, running a true FISP/balance SSFP sequence. The excerpt on of the RF waveform in the right column shows the slice selective waveform used in the sequence and the phase alternation scheme. The 3D plot shows the k-space trajectory as acquired by three different shots of the probe array.

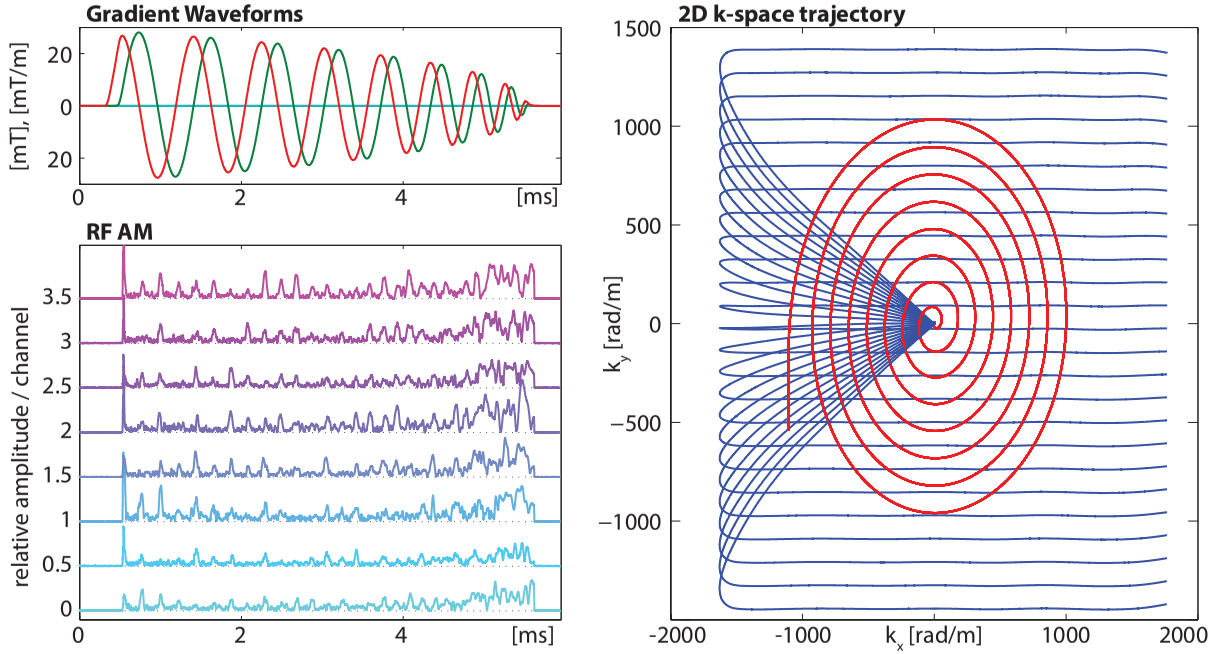

Figure 3.9: Monitoring of a gradient echo sequence using a 4-fold accelerated 8-channel, 2D-selective excitation sequence. The color coding of the gradient waveforms is equal to that in Fig. 3.7. The amplitude modulations are shown shifted by 0.5 for each channel and colored in blue to violet. During the RF pulse the k-space trajectory is plotted in red, the subsequent readout trajectory in blue. For clarity, only every fourth shot of the central slice is plotted.

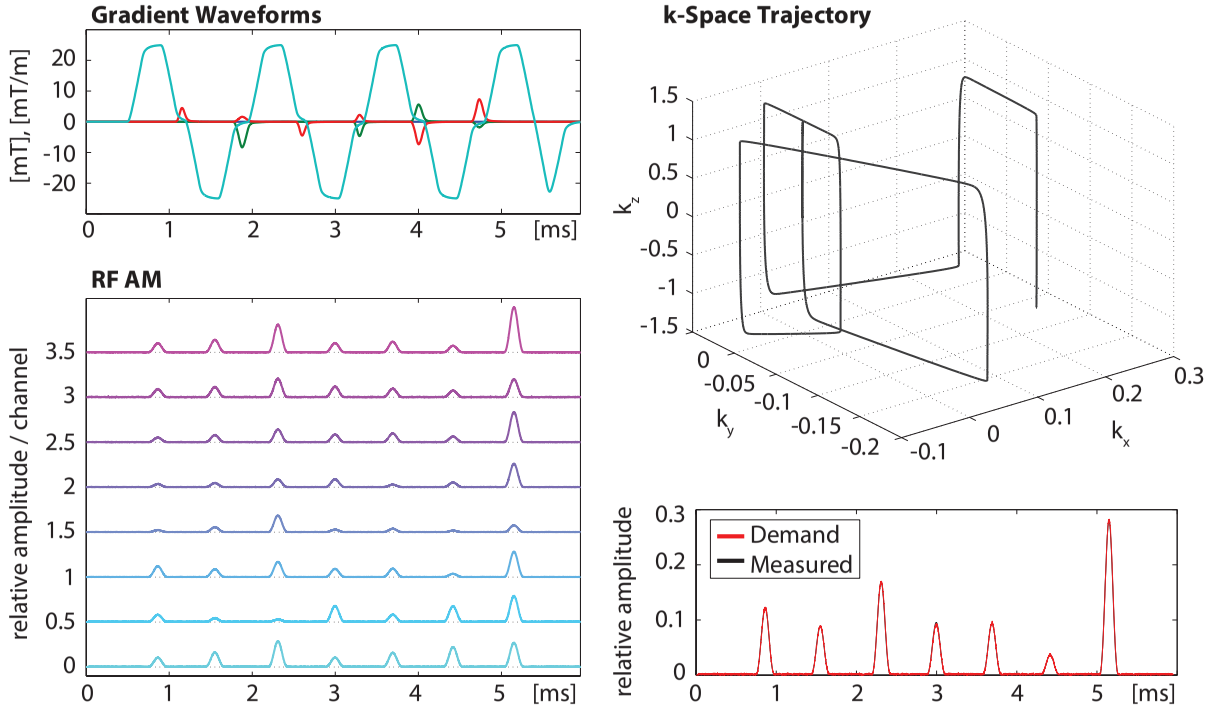

Figure 3.10: Monitored slice-selective 8-channel spoke pulse. The color coding of the gradient waveforms is equal to that in Fig. 3.7. The amplitude modulations are shown shifted by 0.5 for each channel and plotted in blue to violet. A comparison between the waveform demand sent to the scanner and the received waveform is given in the plot on the bottom right showing a very high congruence if aligned to the timing of the calibration pulses.

3.4 Discussion

All dynamic magnetic fields relevant for MR signal formation and encoding were successfully measured with high temporal resolution using a field camera without additional RF pickups and receive channels. A measured sequence diagram is delivered, including fields induced by the sample or subject, by magnet drifts, or by external sources, as far as they can be interpolated with the available finite number of measurement points. This makes it a very versatile development, debugging and validation tool for MRI sequences, similar to an oscilloscope in an electronics lab, delivering quick access to field dynamics in the MRI system.

Additionally to the benefits from longitudinal (low-frequency) field monitoring, as discussed in Chapter 2, the presented system delivers with it's RF monitoring capability insight into the high-power RF stages of MRI systems and their limitations. Effects such as amplitude compression, phase distortions, thermal drifts and memory effects [57], which highly depend on loading conditions, can be observed. Such distortions can lead to deteriorated slice profiles, especially if multi-band pulses with high fidelity demands are employed. Further, concurrent RF monitoring can also be used as a safety measure [49].

Putting the field probes and their wires inside the RF coils can change their fields, similar to other devices, such as dedicated receive coils and visual stimulators. These adverse effects can be reduced by means of optimized probe placement, cable routing and trapping of induced currents.

The use of dedicated RF couplers would certainly increase the SNR in the RF pulse measurements and could be implemented without additional receive channels by signal combination with frequency multiplexing combiners.

Further the entire data evaluation and reconstruction can be based on the concurrently monitored field dynamics with very little

prior information about the sequence that was actually executed. Parsing the sequence diagram [58] yields directly the effective k-space trajectory for the reconstruction and renders a viable image on a unified reconstruction approach even in the presence of small deviations and delays.

4 Continuous Magnetic Field Monitoring Using Rapid Re-Excitation of NMR Probe Sets

Partially published in:

- *"An autonomous system for continuous field monitoring with interleaved probe sets".* Dietrich, Benjamin E.; Barmet, Christoph; Brunner, David O.; Pruessmann, Klaas P. *In Proceedings of the Annual Meeting of ISMRM*, Montréal, Québec, Canada, 2011. Abstract 1842.
- *"A stand-alone system for concurrent gradient and RF sequence monitoring".* Dietrich, Benjamin E.; Brunner, David O.; Barmet, Christoph; Wilm, Bertram J.; Pruessmann, Klaas P. *In Proceedings of the Annual Meeting of ISMRM*, Melbourne, Australia, 2012. Abstract 700.
- *"Analysis of Measurement Precision in Continuous Magnetic Field Monitoring".* Dietrich, Benjamin E.; Brunner, David O.; Wilm, Bertram J.; Barmet, Christoph; Pruessmann, Klaas P. *In Proceedings of the Annual Meeting of ISMRM*, Salt Lake City, Utah, USA, 2013. Abstract 2716.

Partially submitted to:

- *"Continuous magnetic field monitoring using rapid re-excitation of NMR probe sets".* Dietrich, Benjamin E.; Brunner, David O.; Wilm, Bertram J.; Barmet, Christoph; Pruessmann, Klaas P. *IEEE Transactions on Medical Imaging*, 2015. In review.

4.1 Introduction

A key remaining limitation of field monitoring with NMR probes is finite acquisition duration due to signal decay. With susceptibility

matching, current liquid-state field probes achieve lifetimes in the order of 100 ms [20], [23], [30], [31]. Their lifetime is limited by T_2 relaxation, dephasing due to residual susceptibility mismatches and magnetic impurities, and dephasing by external fields, especially gradient fields. As a consequence, field monitoring is typically interrupted after one sequence repetition time or even less for methods using large gradient moments such as diffusion MRI. One workaround is repeated partial measurement [22], [41], which, however, is time-consuming and applies only when the field dynamics of interest are already known to be reproducible.

To overcome these limitations, the present work proposes strictly continuous field monitoring by use of NMR field probes with very short intrinsic lifetime and rapid re-excitation.

At common strengths of several tens of mT/m a gradient field dephases a 1-mm ^{1}H probe in less than a millisecond. Therefore, for continuous field measurement under strong gradients such probes need to be re-excited after several 100 µs. For this to be possible with high SNR yield, T_1 and hence T_2 of the probe liquid are chosen in that same time range, requiring rapid re-excitation also in the absence of strong gradients. Even with such short T_2, upon immediate probe re-excitation there will be a certain amount of residual previous coherence that may perturb the field measurement by the formation of out-of-phase spin echoes. This issue is addressed by alternating operation of multiple sets of probes, such that each individual probe is allowed to relax more fully before re-excitation [59]. In the resulting series of FIDs the RF pulses applied for probe excitation cause gaps by parasitic coupling into the receive paths. This issue is addressed by keeping the gaps small enough, in the range of 10 µs to 20 µs, to recover the full field evolution based on its known bandwidth limitation. Sub-microsecond transmit-receive (T/R) switching, minimized digital filter delays, and frequency-modulated excitation are employed to keep the gaps short and achieve large-angle, large-bandwidth excitation. For con-

tinuous operation the receiver and storage system are laid out to support a 100% acquisition duty cycle over several hours.

Fully continuous measurement capability is desirable for recordings of the magnetic field per se and also for k-space trajectory mapping, which is readily achieved by time integration of measured gradient time courses. Concerning the latter, however, it is important to consider a further key difference between the proposed re-excitation approach and the conventional use of long-lived probes with single excitation. After single excitation, field integration over time is inherently and fully performed by coherent spin precession. In this case, the measurement noise in k-space trajectories depends only on the signal-to-noise ratio (SNR) of the probes at the respective time [20]. By contrast, with repeated probe excitation, the numerical summation of partial integrals provokes accumulation of measurement noise, causing it to increase over time in proportion to the square-root of the number of excitations. Therefore the measurement of long k-space trajectories forms a particular challenge for the re-excitation approach and poses formidable SNR requirements. It is hence given particular attention in the experimental part of this work.

The functionality of the proposed system is demonstrated by examples of continuous sequence monitoring and a case of trajectory mapping. To put the concept to a rigorous test, trajectory mapping was performed for an unusually long (90 ms) single-shot echo-planar readout and verified by image reconstruction. For both field and trajectory measurement the demonstrations are complemented by sensitivity analyses.

4.2 Methods

The continuous monitoring system was created by extension and modification of the stand-alone field camera design previously described in Chapter 2 and 3. In terms of hardware the key addi-

tions and changes concern the probehead design, front-end module, and sequencing provisions for rapid and optionally alternating re-excitation. Figure 4.1 illustrates the most important system components and their interconnections.

4.2.1 Probe Frontend

Two types of field probe arrays were used in this work, one using ^{1}H NMR for high-sensitivity measurements and methods evaluation and one using ^{19}F NMR for concurrent gradient and RF monitoring. Due to superior sensitivity, ^{1}H-based probe arrays are generally favorable for system diagnostics and calibration, gradient and shim characterization [41], [42], and sequence debugging. ^{19}F probes are intrinsically less sensitive but offer spectral decoupling for measurement in the presence of ^{1}H RF transmission or image acquisition.

The ^{1}H probes were built from 2.2 mm inner diameter (0.2 mm wall thickness, approx. 30 mm length) glass capillaries filled with H_2O and doped with $GdCl_3.6H_2O$. Two doping concentrations were used, one such that $T_2 \approx 135\,\mu s$ ($T_1 \approx 160\,\mu s$) and a second one such that $T_2 \approx 70\,\mu s$ ($T_1 \approx 83\,\mu s$). The ^{19}F probes were based on the same type of capillaries filled with 2,3-dimethyl-2,3-butanediol ($C_6F_{12}O_2H_2$) and doped with gadolinium-acetylacetonate ($Gd(C_5H_8O_2)_3$), such that $T_2 \approx 400\,\mu s$ ($T_1 \approx 1.5\,ms$).

To prevent parasitic NMR signals, other ^{1}H or ^{19}F content, respectively, was strictly avoided in the probeheads and connecting lines. The glass capillaries of the ^{1}H probes (Fig. 4.2.B) were mounted on polytetrafluoroethylene (PTFE) holders. Six-turn solenoids (200 µm copper wire with PTFE coating) served as transmit and receive coils [60], [61]. Tuning and matching of the solenoids was achieved with a small adjustable tuning and matching circuit placed on a PTFE-based (Durod, C.I.F, Buc, France) printed circuit board (PCB). They were connected via 50 Ω coaxial cables with PTFE dielectric and a fluorinated ethylene propylene (FEP)

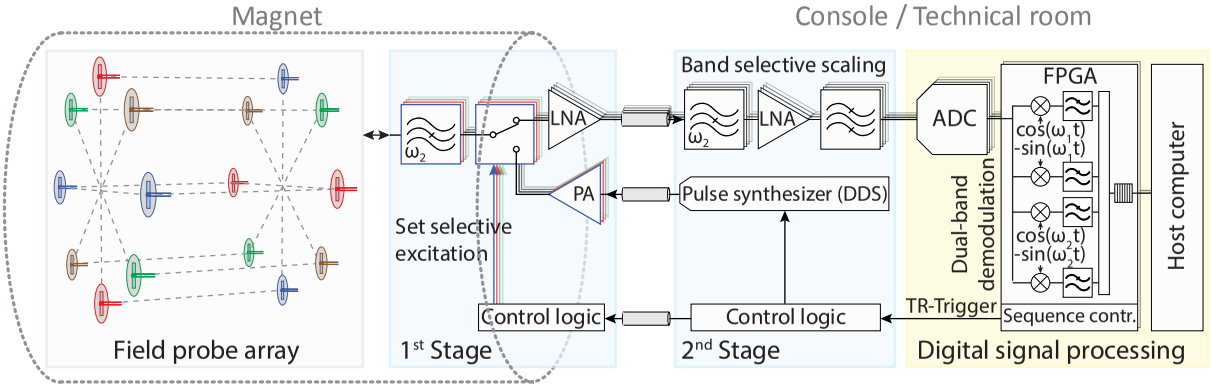

Figure 4.1: Stand-alone monitoring system and its building blocks. From left to right: field probe array and its different probe sets (coloring); 1st-stage electronics, placed inside the scanner bore, comprising filters, transmit-receive switches, low-noise amplifiers (LNA) and excitation amplifiers (PA); 2nd-stage electronics comprising an adjustable gain stage, anti-aliasing filters, and an excitation pulse generation module (DDS); digital signal processing stage consisting of digitizer modules, field programmable gate array (FPGA) modules for demodulation, filtering and decimation, and a host computer for high-level processing and control.

jacket (Multiflex 86, Huber-Suhner, Herisau, Switzerland). In the case of the ^{19}F probes PTFE acts as a source of parasitic signal and was therefore replaced. Here the selected materials were copper wire with polyurethane coating for the solenoids, FR4 for the PCB, and polyethylene as dielectric in the coaxial cable (G 02232 D, Huber-Suhner, Herisau, Switzerland).

The tuning and matching circuit (Fig. 4.2.A) was designed to withstand the excitation power in the order of 1 W to 3 W, which can lead to more than 100 V over the capacitors. Frequency tuning was achieved by scrapping off copper segments designed to form distributed adjustable capacitors (Fig. 4.2.A and B). An input return loss smaller -20 dB was achieved on the 50 Ω port. To reduce strong RF coupling to any external proton transmitter in case of the ^{19}F probes, the leads of the solenoid were twisted and a stubline filter at the proton frequency was added, built from a coaxial cable of suitable length.

The rather large capillary diameter compared to typical long-lived field probes [20], [21], [23], [30] is motivated by the need to boost SNR for trajectory mapping. It is bounded by tuning and matching limits on the inductance of the transmit-receive solenoid and by dephasing under strong field gradients. At the chosen diameter, the highest prospective gradient strength of 40 mT m^{-1} leads to critical dephasing after approximately 380 µs, which is well above the T_2 of the ^{1}H probes and thus limits the potential impact of spin echos. Although desirable, in the ^{19}F probes T_2 decay could not be rendered quite as dominant due to limited solubility of suitable relaxation agents.

An array of 16 ^{1}H probes was mounted on two PTFE plates as shown in Fig. 4.2.C. To vary the diameter of the setup, slits in the plates allow the probes to be moved radially and the distance between the plates can be adjusted with thread bars. The probe arrangement was chosen such as to form 4 sets of equal tetrahedral structure (illustrated by coloring in Fig. 4.1) for opti-

mal conditioning of first-order spherical-harmonic field expansions (B_0, G_x, G_y, G_z). The ^{19}F probe array was mounted in a similar fashion, using a 2-set configuration with the two sets forming mutually rotated cubes.

4.2.2 Transmit/Receive Hardware

As detailed in Chapter 2 and [52] the receiver hardware was based on a software-defined radio approach without analog frequency conversion. A first stage of electronics, comprising T/R-switches, preamplifiers and excitation amplifiers was directly connected to the field probe array for placement inside the magnet bore (Fig. 4.1). A second stage of electronics used for signal scaling and conditioning as well as digitization and digital signal processing was connected via coaxial cables and placed outside the scanner room due to incompatibility with high magnetic fields.

Each probe's T/R-switch and excitation power amplifier blanking circuit was controlled separately to enable alternating excitation of subsets of probes. Field effect transistor (FET)-based T/R-switches were used to achieve sub-microsecond switching performance [52].

To enable simultaneous reception of ^{19}F probe signals and ^{1}H RF pulses from the host MR system, a set of band-selective filters was added in front of the gain stages (notch filters at ω_2 in Fig. 4.1), similar to the presented solution in Chapter 3. They attenuate the typically much stronger ^{1}H transmit signals to a degree that the receive chain stays in a safe, linear regime while receiving both signals [62]. Two sets of in-phase and quadrature demodulators, one for each frequency band, were implemented on the field programmable gate arrays (FPGA) of the digital signal processing stage to retrieve complex baseband signals with a typical bandwidth of 1 MHz. Fully continuous reception with 16 channels, 1 MHz bandwidth each for probes and RF pickup, and a word width of 32 bit each for real and imaginary parts, resulted in a

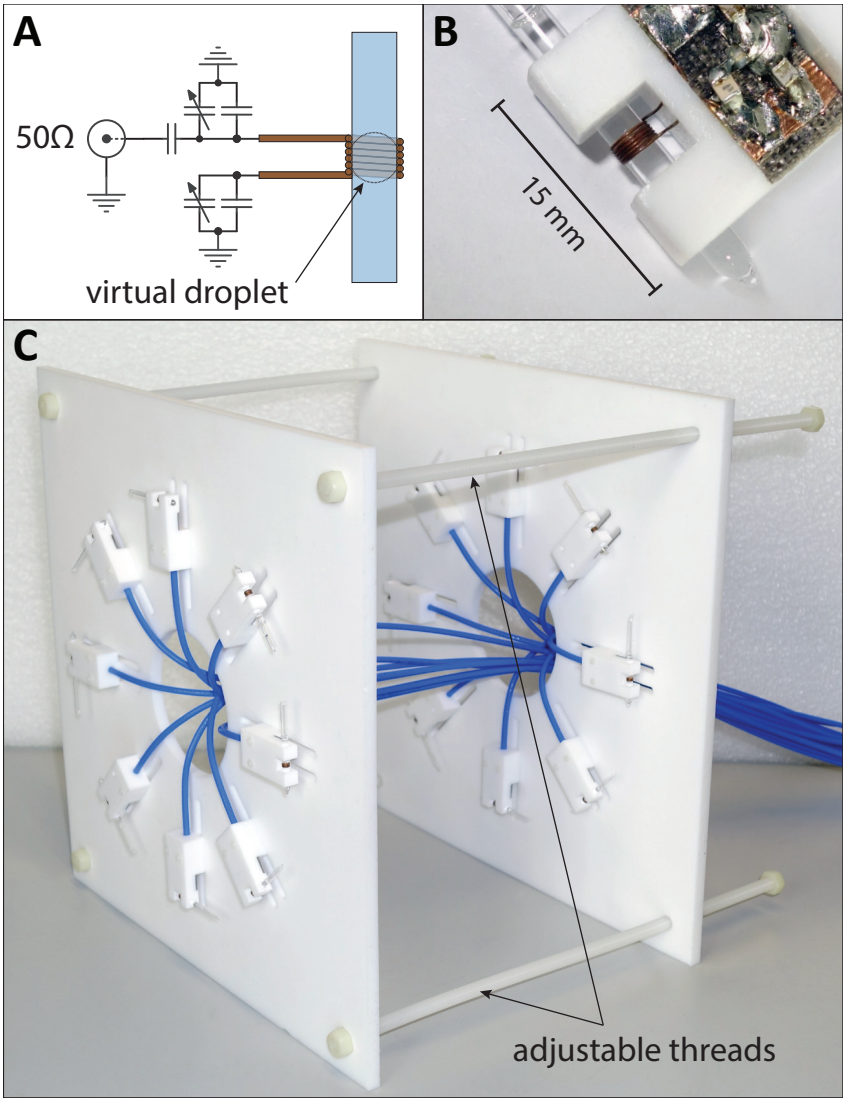

Figure 4.2: Schematic of the probe circuit and capillary (A). Image of an actual field probe (B). Adjustable field probe array comprising a total of 16 probes (C).

total data rate of 256 MB/s. To permit acquisition of such large data streams over long periods, the system was further equipped with a redundant array of independent disks (RAID) with a capacity of 6 TB, enabling continuous acquisitions up to 6.5 h. To keep the excitation gaps in the data sufficiently small the group delay of digital filtering in the FPGA was minimized. Filter delays add directly to the total gap duration and hence limit the monitoring bandwidth. The resulting group delays range between 2 µs and 3.5 µs, depending on the selected output data rate and stop band rejection.

The direct digital synthesis (DDS) based pulse synthesizer module used for probe excitation pulse generation was programmed to generate 8.5 µs long frequency-sweep pulses of 800 kHz bandwidth. The large bandwidth is required to cover the full range of Larmor frequencies that the probes may assume in the presence of gradients. Frequency modulation enhances the flip angle that can be achieved within the given RF power limits. Shorter pulses are straightforward yet would come at the expense of flip angle and hence reduced SNR.

4.2.3 Sequence Timing and Synchronization

A set of logic cores and pulse generators operating at 100 MHz, implemented on one of the FPGA modules, serves as sequence controller and generated all required control signals. The selection and interleaving of probe sets is performed by programmable logic connected to the transmit unit. In a 1-set configuration a single set of probes is immediately re-excited after each alternation period (T_{set}). In a 2-set configuration two sets are operated in an alternating fashion such that each set is excited every 2 T_{set}. Analogously, 3-set and 4-set operation involves cycling through the available sets with correspondingly prolonged recovery periods (see also the probe coloring in Fig. 4.1). Figure 4.3 depicts the timing and control scheme for a typical 2-set configuration. The system

can be started and synchronized by an external trigger signal, typically from the MR system under study.

To use monitoring results together with imaging data acquired with the host MR system, the two systems are synchronized and corrected for receive chain delays. The resolution of trigger-based synchronization was 10 ns and thus two orders of magnitude higher than the temporal resolution of typical imaging data. Delay calibration was achieved with the help of an amplitude-modulated reference signal which was transmitted into both receive chains during a calibration scan. The resulting delay was calculated by cross-correlation of the two signals.

Remnant coupling between channels corrupts all received signals during re-excitation of any set due to the enormous power difference (90 dB and more) between transmit and receive signals. The length of the resulting excitation gaps (T_{gap}) is given by the cumulated duration of the excitation pulse (8.5 µs), the transmit-receive and receive-transmit switching delays (< 1 µs each), and twice the digital filter delay (≈ 4 µs to 7 µs total). The field evolution during the gaps can be recovered by interpolation if the signal support comprises a regular grid of sufficient density with respect to the bandwidth (BW) of the field dynamics. This is the case if

$$\frac{1}{T_{gap}} \geq \frac{\left\lfloor \frac{T_{set}}{T_{gap}} \right\rfloor}{T_{set}} \geq 2\,BW, \tag{4.1}$$

where the brackets indicate rounding down. Accordingly, for $T_{set} = 150\,\mu s$ and a typical total re-excitation gap of $T_{gap} = 16\,\mu s$ the allowed field bandwidth is $BW = 30\,kHz$, which is sufficient for typical clinical MR systems.

4.2.4 High-Level Signal Processing

Figure 4.5 illustrates higher-level processing using a 2-set example (measured data). First the signal phase of each probe is ex-

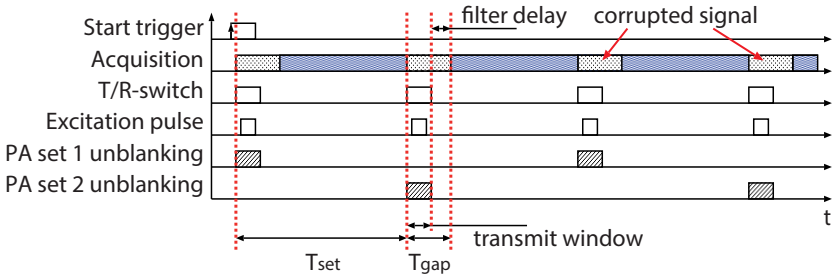

Figure 4.3: Control signal timing of a typical monitoring experiment with two alternating probe sets.

tracted and unwrapped for the relevant intervals. Then the phase coefficients $k_0(t), k_x(t), k_y(t), k_z(t)$ are calculated by fitting a first-order spherical-harmonic model as described in Section 1.2.2 and Ref. [21]. As the figure illustrates, the resulting coefficient time courses still have arbitrary offsets per interval, arising from the arbitrary phase of probe excitation. These are eliminated by taking the time derivative of the coefficient functions and dividing by the gyromagnetic ratio of the probe nucleus to arrive at the field representation $B_0(t), G_x(t), G_y(t), G_z(t)$ (only gradient components shown). Next the gaps are removed by interpolation under the given bandwidth limitation (Eq. 4.1). This is done by formulation as a least-squares fit with the bandwidth condition as a linear constraint. The fit is carried out with a standard conjugate-gradient algorithm using alternation between the time and frequency domains for efficient multiplication with the respective support functions. After the interpolation step the results are optionally decimated, according to the bandwidth constraint, to reduce the data volume. Time integration of the interpolated gradient time courses yields continuous k-space trajectories if desired.

In the case of complementary RF monitoring, the RF recordings were equally affected by the excitation gaps, since they share the

same analog receive chains. The amplitude and phase-time courses were first extracted, the frequency modulation retrieved by temporal derivation of the phase-time course and then interpolated using the same approach and bandwidth limitation constraint as described above.

4.2.5 Experiments

All measurements were performed in a whole-body 7 T Philips Achieva system (Philips Healthcare, Cleveland, USA). For imaging experiments a commercially available 16-channel head receive array was used (Nova Medical, Wilmington, USA).

For demonstration of continuous field monitoring capability a diffusion-weighted spin-echo EPI sequence ($G_{max} = 40\,\mathrm{mT\,m^{-1}}$, $b = 5000\,\mathrm{s\,mm^{-2}}$) and a balanced steady-state free-precession sequence (bSSFP) (TE = 13 ms, resolution = 1 mm × 1 mm, field of view = 220 mm × 220 mm) were monitored with one of the ^{1}H probe arrays ($T_2 = 135\,\mu\mathrm{s}$) in a 2-set configuration of 4 probes each and a set alternation period $T_{set} = 150\,\mu\mathrm{s}$.

To demonstrate trajectory monitoring an exceptionally long single-shot gradient-echo EPI readout (90 ms duration, $40\,\mathrm{mT\,m^{-1}}$ peak gradient strength, 1.5 mm in-plane resolution) was used. To increase robustness against spurious spin echo formation this experiment was performed with the ^{1}H probe array of $T_2 = 70\,\mu\mathrm{s}$, using a 2-set configuration of 8 probes each. The set alternation period was $T_{set} = 110\,\mu\mathrm{s}$. For verification, the trajectory thus measured was used for image reconstruction from phantom image data obtained subsequently with the same sequence. Algebraic reconstruction was performed with the iterative algorithm described in Ref. [45], yet without the use of coil sensitivity maps.

Combined continuous monitoring of gradient fields and RF pulses is demonstrated with examples of bSSFP, Turbo Spin Echo (equivalent to RARE [63]), and point resolved spectroscopy (PRESS) [64] with outer-volume suppression. These sequences were monitored

with the ^{19}F array in a 2-set configuration of 8 probes each. A set alternation period of 500 µs was selected due to the larger T_2 of the ^{19}F probes. This is a compromise between SNR and spurious spin-echo formation. Additionally the peak gradient amplitude was reduced to 10 mT m^{-1} in order to limit probe dephasing.

4.2.6 Sensitivity and Consistency Assessment

For sensitivity assessment continuous field measurements of 1 s duration each were performed with the ^{1}H array ($T_2 \approx 135$ µs) under constant gradients for varying gradient directions, strengths, setup diameters, number of probe sets, and set alternation periods. To ensure gradient settling, each measurement was delayed by 200 ms with respect to the gradient ramp. For each readout the standard deviations of the continuous spatial field expansions were calculated. As a measure of sensitivity in relation to gradient strength the root mean square of the standard deviation was then determined across 1$^{\text{st}}$-order components of equal gradient magnitude. For comparison the same sensitivity measure was also calculated based on simulated FIDs incorporating measured relaxation times and probe signal SNR, but without taking into account any errors due to spin echo formation or field variation in probe droplets.

When fields of higher spatial order than the employed field model are present they contaminate the available lower orders in a fashion akin to aliasing, causing measurement error. With alternating probe sets, this mechanism is inconsistent between sets and thus causes spurious field dynamics upon interpolation. To assess this issue, measurements with redundant sets of probes (once a pair of 1-sets of 4 probes and once a pair of 2-sets of 4 probes) were performed. Again, field measurements under static gradients were carried out similar to the previous experiment. This time the standard deviations were calculated on the difference between the redundant measurements and the root mean square of the standard deviations across 1$^{\text{st}}$-order components of equal gradient magnitude was used

as measure of consistency.

To study the expected altered noise behavior in trajectory measurements a direct comparison with a set of single-coherence probes was performed. Four long-lived ^{19}F probes ($T_2 \approx 36\,\text{ms}$, 1.3 mm droplet diameter), as described in [31], [34], [37], were employed together with 2 sets of 4 ^{1}H continuous probes ($T_2 \approx 70\,\mu\text{s}$) in a setup of 23 cm diameter. The ^{19}F nucleus ensured spectral decoupling from the short-lived ^{1}H probes. While the long-lived reference probes were only excited once in the beginning, the continuous monitoring probes were operated as shown in Fig. 4.3 ($T_{set} = 110\,\mu\text{s}$). A series of 50 EPI readouts was used for statistical analysis of the resulting trajectory differences. The choice of maximum k-space excursion ($1500\,\text{rad}\,\text{m}^{-1}$) and readout duration (23 ms) was limited by the long-lived reference probes.

4.3 Results

At full excitation with the 8.5 µs sweep pulse the short-lived probes achieved sensitivities $\xi = SNR\sqrt{BW}$ [20] of $\xi_{1\text{H}} = 2.6 \times 10^6\sqrt{Hz}$ and $\xi_{19\text{F}} = 1.6{\times}10^5\sqrt{Hz}$. In nominally constant background field a small non-linear phase residual in the order of 1 mrad to 5 mrad was observed (Fig. 4.4). This phase error is partially due to actual field fluctuations but also relates to residual coherences from preceding excitations and to field variation inside the probes due to static susceptibility effects of the wires and PTFE holders. The error increases towards the end of a readout and leads to inconsistency with the beginning of the next readout.

4.3.1 Field Monitoring

Figure 4.5 shows a continuously monitored diffusion-weighted spin-echo EPI sequence and the involved processing steps in close-ups. At the bottom the whole time course is depicted including the

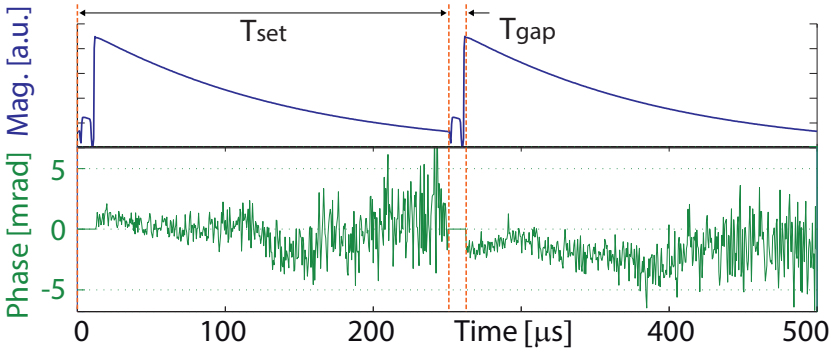

Figure 4.4: Magnitude and phase of a probe signal over two acquisition intervals. Excerpt from a continuous monitoring experiment in the presence of a constant gradient of $20\,\mathrm{mT\,m^{-1}}$ in a 1-set configuration with the ^{1}H array. The probe is re-excited after $T_{set} = 250\,\mu\mathrm{s}$.

large-moment diffusion gradients. A balanced SSFP sequence monitored continuously for about 12 s is shown in Fig. 4.6. The close-up shows intermediate, gapped data at 1 MHz bandwidth along with the result of band-limited interpolation (cf. rows 4 & 5 in Fig. 4.5).

Sensitivity and Consistency

Figure 4.7 illustrates the results of the field sensitivity measurements. It shows that signal decay upon long T_{set} (Fig. 4.7.B) and gradient-induced dephasing (Fig. 4.7.C) have more severe effects on net sensitivity than spurious echo formation, which would affect the single-set configuration more strongly than multiple-set configurations. Errors due to spurious coherence histories corrupt the measurements primarily when dephasing by strong gradients is involved and can be reduced by set alternation as seen in Fig. 4.7.C. As expected, the sensitivity increases with the setup diameter due

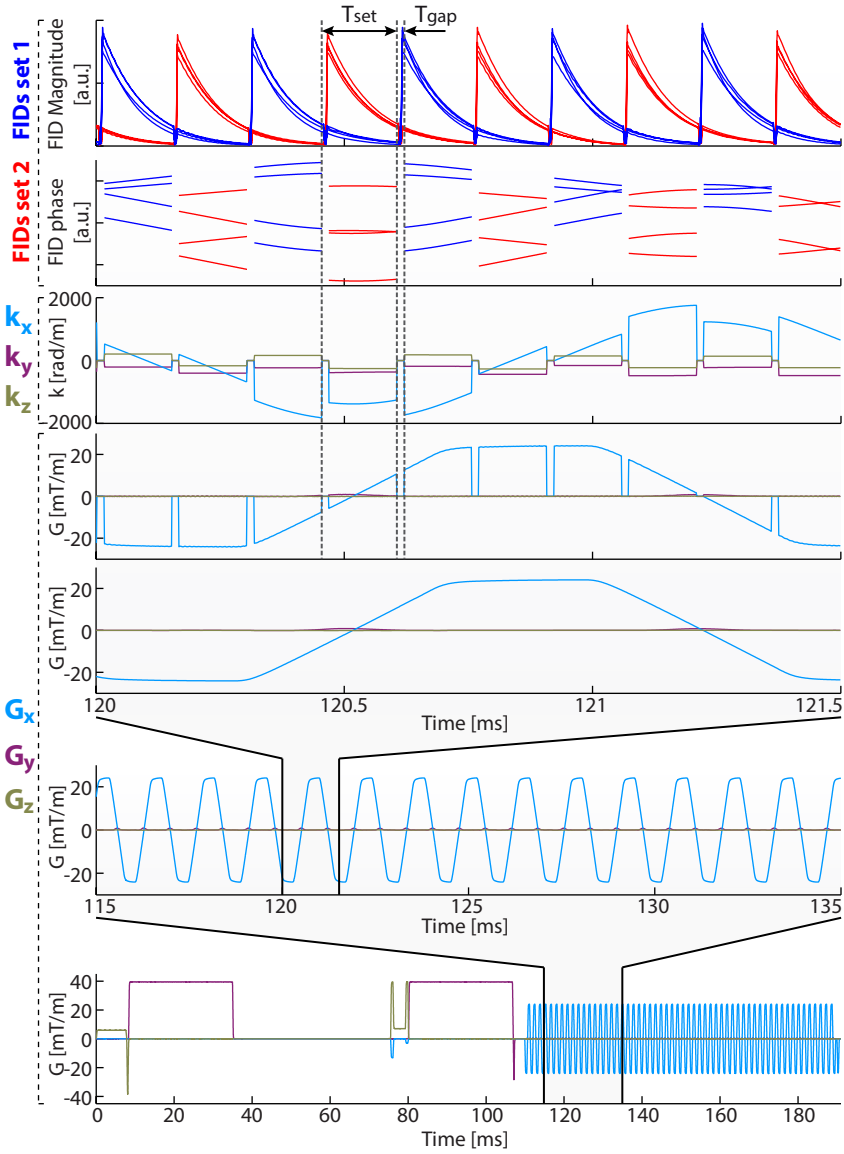
FIDs set 1
FIDs set 2
FID Magnitude [a.u.]
FID phase [a.u.]
Tset
Tgap
kx
ky
kz
k [rad/m]
2000
0
-2000
G [mT/m]
20
0
-20
Gx
Gy
Gz
120
120.5
121
121.5
Time [ms]
115
120
125
130
135
40
-40
0
20
40
60
80
100
120
140
160
180

Figure 4.5: Continuously monitored diffusion-weighted spin-echo EPI sequence and involved processing steps in the zoomed part of the EPI readout. Monitored with 2 sets (blue and red) of 4 probes each. Top-down: magnitude of the FIDs, phase evolution of selected probe sets, phase coefficients k(t), gradient fields G(t) with re-excitation gaps, and interpolated gradient fields.

to the larger excursions of gradient fields (Fig. 4.7.A). Apparent sensitivity was slightly increased by turning off the gradient and shim amplifiers, indicating a variance contribution from actual field noise (Fig. 4.7.C). Overall the achieved sensitivity lies in the range of $5\,\mu T\,m^{-1}$ at a bandwidth of 30 kHz, resulting in a resolution of 0.5 µT to 1 µT within a typical imaging volume. Inconsistencies among redundant simultaneous measurements are shown in Fig. 4.8 for various static gradient and probe set configurations. They are in the same range as the precision measurements, suggesting that there was no severe spatial consistency problem. These measurements also show a similar pattern regarding the number of sets: multiple sets are beneficial under strong gradients when significant inhomogeneous broadening occurs.

4.3.2 Trajectory Monitoring

Figure 4.9.A shows the continuously monitored 90-ms single-shot EPI trajectory. The corresponding phantom image reconstructed with the monitored trajectory is shown in Fig. 4.9.B. It shows no conspicuous artifacts other than common truncation ringing, non-uniform RF coverage, and slight distortion due to B_0 non-uniformity, correction of which was not included in the reconstruction. In particular, the image shows no ghosting, which is a sensitive marker of EPI trajectory errors.

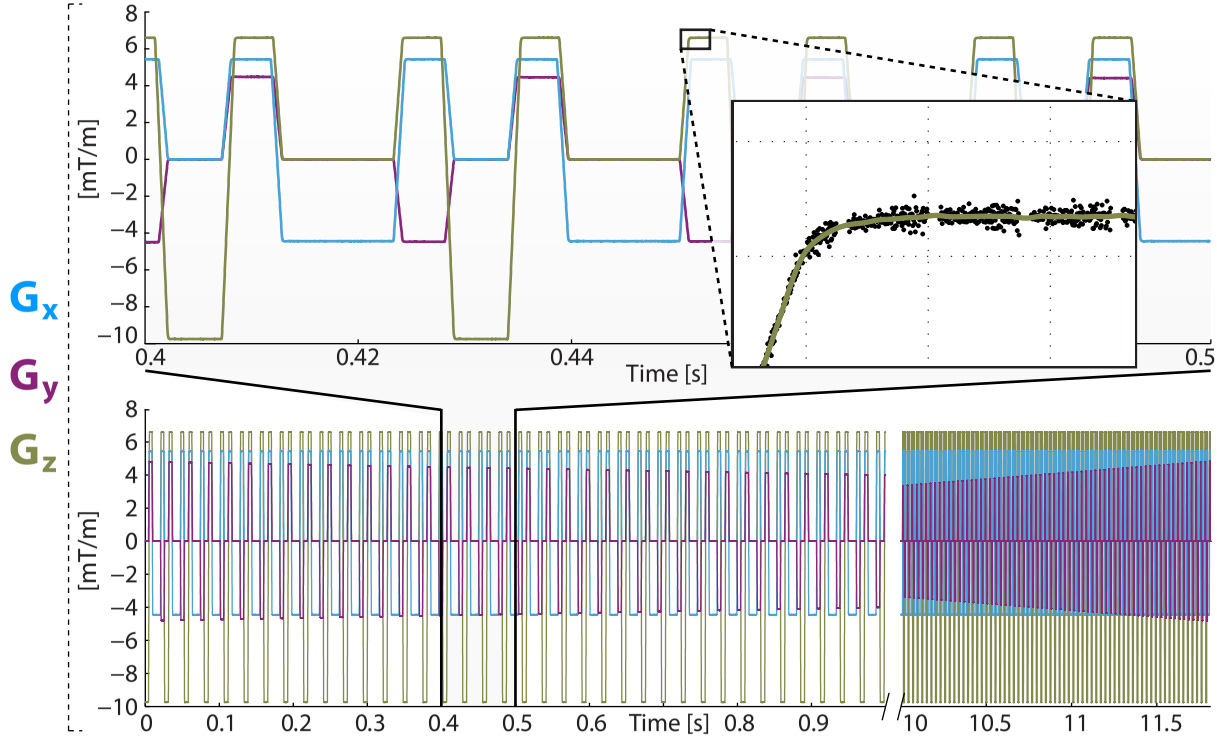

Figure 4.6: Continuously monitored balanced SSFP. Close-up: field evolution before interpolation at 1 MHz bandwidth (black dots) and final band-limited z-gradient field evolution (olive).

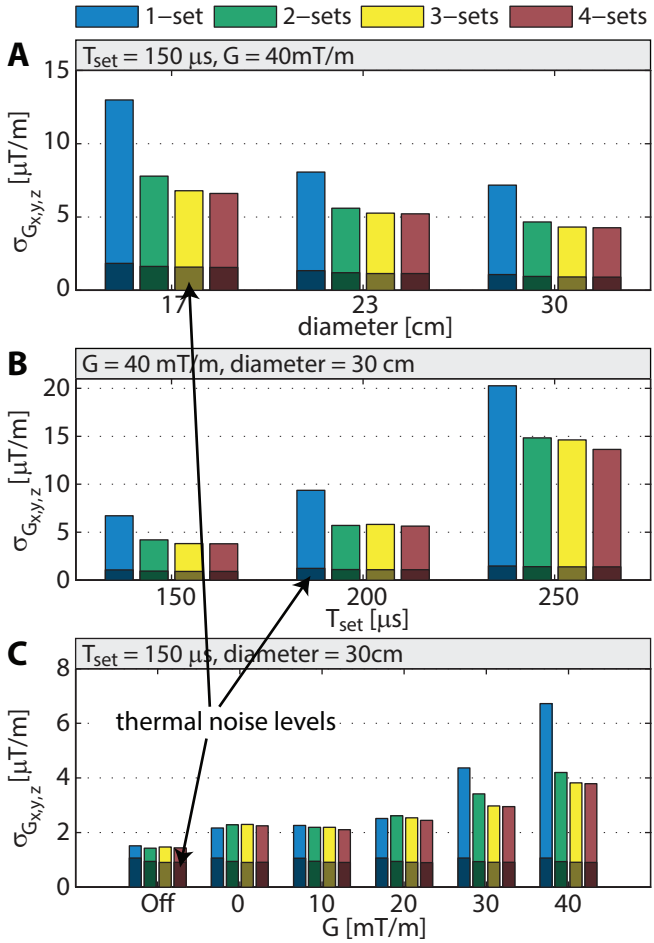

Figure 4.7: Sensitivity under constant fields measured with various setup diameters (A), set alternation periods (B), gradient strengths (C), and set configurations at a field measurement bandwidth of 30 kHz. The shorter, darker bars represent expected thermal noise according to measured SNR(t) of the probe signals. "off" in C indicates that the gradient and shim amplifiers were fully turned off unlike the case of $0\,\mathrm{mT\,m^{-1}}$, in which the MR system was idle while powered on.

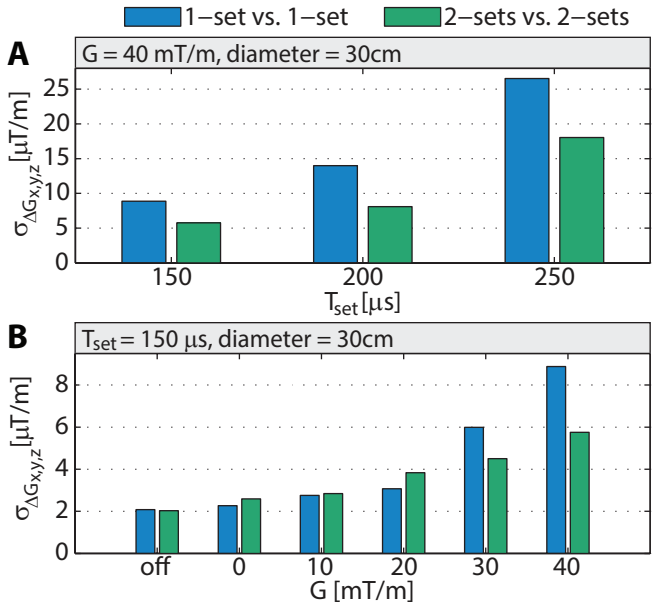

Figure 4.8: Consistency between two redundant concurrent measurements is shown for various set alternation periods (A), gradient strengths (B), and set configurations, at a bandwidth of 30 kHz. "off" in B indicates that the gradient and shim amplifiers were fully turned off unlike the case of $0\,\mathrm{mT\,m^{-1}}$, in which the MR system was idle while powered on.

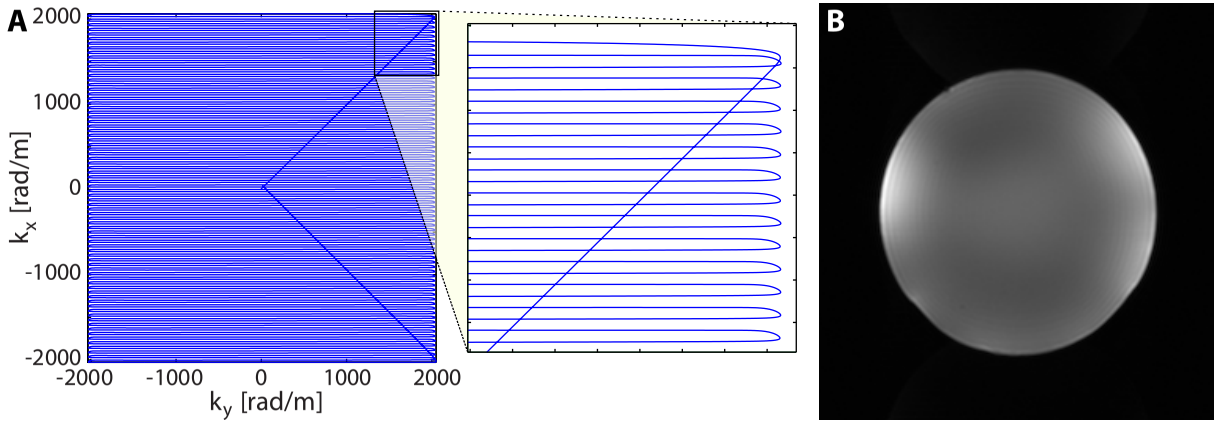

Figure 4.9: Continuously monitored single-shot EPI trajectory of 90 ms duration obtained with over 800 field probe excitations (A). Phantom image acquired with this readout and reconstructed based on the measured trajectory (B).

Sensitivity and Consistency

As can be seen in Fig. 4.10, comparison between the single-coherence reference method and the proposed rapid re-excitation approach confirms the expected square-root noise behavior. Different standard deviations $\sigma(t) = \sigma_{step}\sqrt{t/T_{set}}$ result for different spatial components with $\sigma_{step} = 2.8\,\mathrm{mrad}$ in case of the 0^{th}-order component and $\sigma_{step} = 4\,\mathrm{mrad\,m^{-1}}$ averaged over all 1^{st}-order components. The discrepancies within the 1^{st}-order components are most likely due to the spatial phase expansion, scaling the sensitivity depending on the probe positions, and due to sensitivity variations between probes.

4.3.3 Simultaneous RF Pulse and Gradient Monitoring

Figure 4.11 shows the results of continuous concurrent gradient and RF pulse monitoring, which delivers a comprehensive view of all dynamic magnetic fields relevant for MR signal formation and encoding through a single measurement.

4.4 Discussion

The proposed concept enables fully continuous spatio-temporal field monitoring over arbitrary durations without any modification of the MR system or sequence under test. In particular, it newly permits field monitoring of sequences employing large gradient moments such as high-resolution or diffusion imaging, and of long readouts with large gradient strength. Studying essentially any magnetic field dynamics is no longer limited by probe dephasing and relaxation or restricted to time-consuming snapshot measurements. This capability holds promise for a variety of uses ranging from sequence development, image reconstruction, field control [32], and motion correction [40], [65] to system characterization [41], [42] and calibration, hardware diagnostics, and

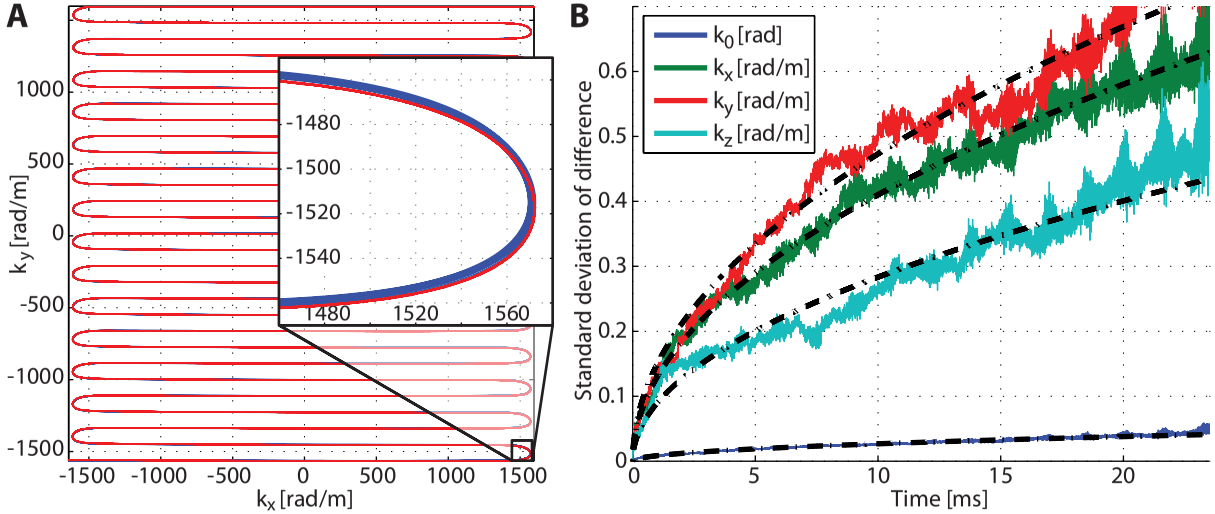

Figure 4.10: Series of 50 EPI trajectories acquired with the single coherence reference method (red), and continuous method (blue) at the same time (A). Standard deviation of the difference between the trajectories (B). The black dotted lines indicate fitted square root functions according to expected noise accumulation behavior.

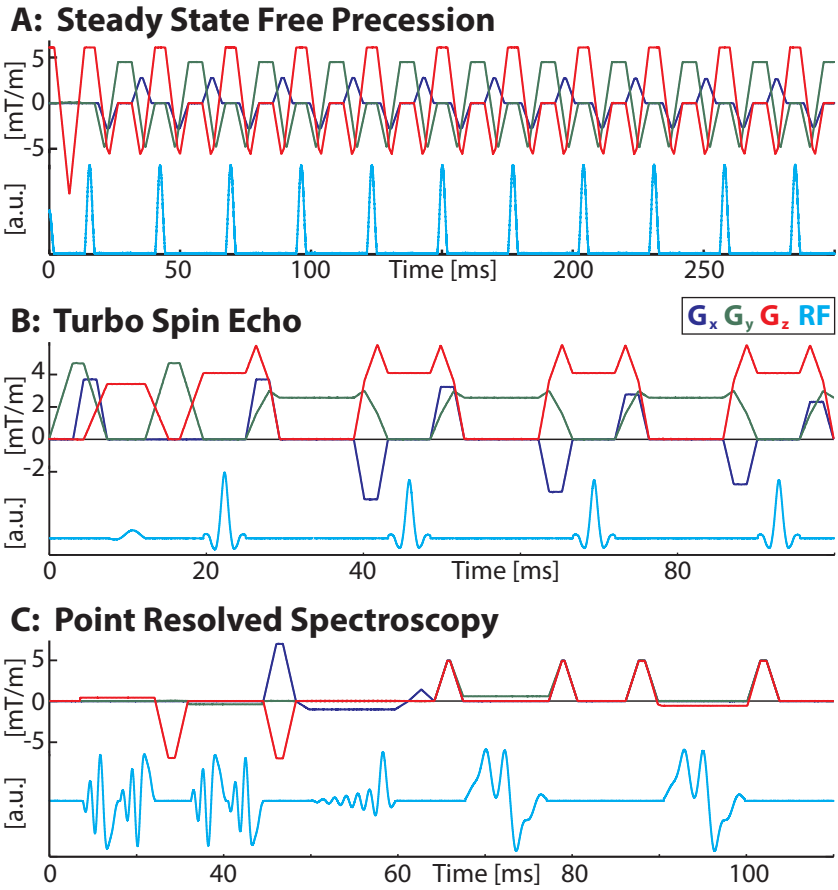

Figure 4.11: Continuously monitored steady-state free precession (A) and turbo spin-echo (B) sequences as well as point-resolved spectroscopy with outer-volume suppression (C), including concurrent RF pulse monitoring.

quality assurance. Additionally, continuous field monitoring opens up the novel capability of routinely recording entire scans. Such large data sets may prompt further modes of use such as machine-learning approaches for remote MR system diagnostics and failure prediction.

With the current ^{1}H implementation the achieved field measurement precision is in the range of 0.5 µT to 1 µT at a bandwidth of 30 kHz, relying on raw probe SNR of multiple thousands at 1 MHz bandwidth. The remaining measurement error is partly related to thermal detection noise but has been found to be predominantly of systematic nature. According to the reported sensitivity study, for moderate external gradients the largest error contribution stems from residual field distortion inside the probe droplets. It could be reduced by susceptibility matching of all materials around the droplet, which however is challenging due to the need to strictly avoid sources of ^{1}H signal. When strong external gradients render T_2^* of the droplet significantly shorter than T_2, spin echoes can introduce errors if their phase is not aligned with that of the concurrent FID. This issue has been successfully addressed by alternation of probe sets. Conversely, this means that probe alternation permits rendering the diameter of the droplets larger, resulting in a steep increase in sample volume and thus signal-to-thermal-noise ratio. Practical limits to the feasible probe size are set by increasing transmit power requirements and the need for robust tuning and matching. A third source of systematic error is inconsistency between alternated probe sets, which occurs when the observed field is of higher spatial order than the probes can resolve. The reported consistency experiment suggests that this mechanism was not a dominant source of error in this work.

Field probes based on ^{19}F NMR permit continuous gradient monitoring concurrently with ^{1}H imaging procedures and/or with equally continuous ^{1}H transmit RF recording as demonstrated in this work. The use of ^{19}F samples also simplifies susceptibility

matching of probeheads, since it removes the need to avoid materials that contain ^{1}H. On the other hand, ^{19}F field probes are inherently less sensitive than ^{1}H probes due to lower gyromagnetic ratio and lower spin density than, e.g., water. Furthermore, suitable liquids of high ^{19}F content, particularly fluorocarbons, do not or hardly dissolve paramagnetic salts. Therefore it remains challenging to reduce their relaxation times to the order of 100 µs.

For trajectory mapping this study has confirmed the anticipated accumulation of measurement noise in proportion to the square root of the number of excitations involved. Nonetheless, continuous mapping of a long single-shot trajectory was of sufficient fidelity for image reconstruction even though it involved over 800 probe excitations in 90 ms. Generally, the root-time accumulation of trajectory noise is benign compared to exponential error growth due to relaxation with single excitations. The single-coherence approach is advantageous when the duration of the targeted trajectory does not substantially exceed the probe T_2, its k-space excursions are within limits set by the probe diameter, and the subsequent need for probe recovery is acceptable.

Combined continuous gradient and RF pulse monitoring constitutes comprehensive MR sequence recording, which holds promise as a tool for sequence development, verification, and debugging, as well as system analysis. In the presented configuration the same analog receive chains are used for RF pulses and probe FIDs. Therefore the RF monitoring capability shares the bandwidth limitation that arises from the probe excitation acquisition gaps. The currently feasible bandwidth of about 30 kHz suffices for many common sequences. Frequency-modulated RF pulses of larger bandwidth can still be resolved as long as the amplitude and frequency modulation functions are within the 30 kHz limit. Nevertheless, certain types of RF waveforms, e.g., multiple-dimensionally selective or multiple-band pulses will only be captured with larger actual recording bandwidth. This requirement could be met with sepa-

rate pickup circuits and analog receive chains for the RF pulses, bypassing the T/R-switches and probe signal amplification stages.

5 Continuous Higher-Order Magnetic Field Monitoring and Single-Shot Shim Characterization

Partially published in:

- *"Continuous 3^{rd}-order field monitoring: Design and application for single-shot shim characterization".* Dietrich, Benjamin E.; Brunner, David O.; Vannesjo, S. Johanna; Duerst, Yolanda; Wilm, Bertram J.; Pruessmann, Klaas P. *In Proceedings of the Annual Meeting of ISMRM*, Toronto, Ontario, Canada, 2015. Abstract 1016.

5.1 Introduction

So far continuous magnetic field monitoring (Chapter 4) has been limited to 0^{th} and 1^{st}-order spatial field expansions. However, uninterrupted measurement over long times is equally critical in dealing with higher-order fields, particularly in the context of recent advances in dynamic shim updating [66]–[69], real-time field control [32], [33], and application of non-linear encoding schemes [70], [71]. Also methods based on retrospective correction of higher order field distortions, such as caused by eddy currents in diffusion weighted MRI [34] or caused by physiological field fluctuations [39], would benefit from uninterrupted higher-order field monitoring.

The need for enhanced measurement capability is further exemplified by the task of determining gradient and shim impulse

response functions [42], [72] for system characterization. Knowing the impulse response functions of the entire system (gradients and shims) enables accurate trajectory prediction and calculation of pre-emphasis filters [73], [74]. So far, impulse response function measurements with NMR probes required a large number of stroboscopic acquisitions [41], resulting in long overall measurement duration. In contrast, continuous observation with sufficient sensitivity holds the potential of permitting such characterization in a single shot within seconds, prompting the intriguing perspective of real-time analyses of system properties, e.g., under thermal stress.

The aim of the present work is to accomplish this capability by implementation of 3rd-order fully continuous field monitoring, which poses a range of challenges. Among others, enhanced sensitivity requirements for higher-order field components impose rigorous suppression of parasitic NMR signals from solids in the probeheads. And the substantial increase in probe and channel counts requires advanced considerations for mutual RF decoupling and provisions for massive data flows during continuous measurements. The presented solution is based on the continuous monitoring system introduced in Chapter 4 and its functionality presented in examples of single-shot impulse response function measurements, sequence/system analysis, and continuous sequence monitoring including dynamic shim fields.

5.2 Methods

5.2.1 Monitoring System

Dynamic field monitoring was performed with the custom built, scanner independent field camera, as introduced in Chapters 2,4 and Refs. [52], [59]. This system is based on a software defined radio approach without any analog frequency conversion, but direct digitization, digital demodulation, and signal processing on

field programmable gate arrays (FPGA). This enables processing modifications without complex hardware implications and convenient scalability in terms of number of channels. Several modifications were performed in order to support continuous monitoring with multiple probe sets and full 3rd order spherical harmonic field expansions. These modifications comprise the probe head design, field probe array, the number of channels, and the digital data flow. Figure 5.1 schematically illustrates the most important system components and their interconnections.

Simultaneous field expansion on a full 3rd order spherical harmonic basis (Tab. 5.1) requires at least 16 field probes. In case of set alternation, which is especially useful in the presence of strong de-phasing gradients (see Section 4.3.1 and Ref. [75]), this number scales according to the number of employed sets. Therefore the system was upgraded to support 32 channels, by adding a second set of 16 transmit-receive (T/R) modules and gain stages, as well as additional analog to digital converter (ADC) modules and FPGAs, enabling full 3rd order expansions with 2 probe sets.

Each 4-channel ADC module, sampling at a rate of 250 MHz, was connected to a demodulation and down conversion FPGA, streaming complex baseband samples (8 bytes per sample) at a rate of 1 MHz to a data synchronization and sequence control FPGA. All FPGAs were connected through a PCI-Express bus, supporting data rates of up to 4 GB/s per lane. The data, arriving at a combined rate of 256 MB/s, was then stored on a redundant array of independent disks (RAID) with a capacity of 6 TB for further high level processing. This enables continuous acquisitions up to 6.5 h.

The field camera was operated in either a 1-set configuration or 2-set configuration. In the 1-set configuration all probes were re-excited at the same time after 130 µs. In the 2-set configuration the sets were re-excited in an alternating fashion such that each probe set has two set periods of 110 µs for relaxation before

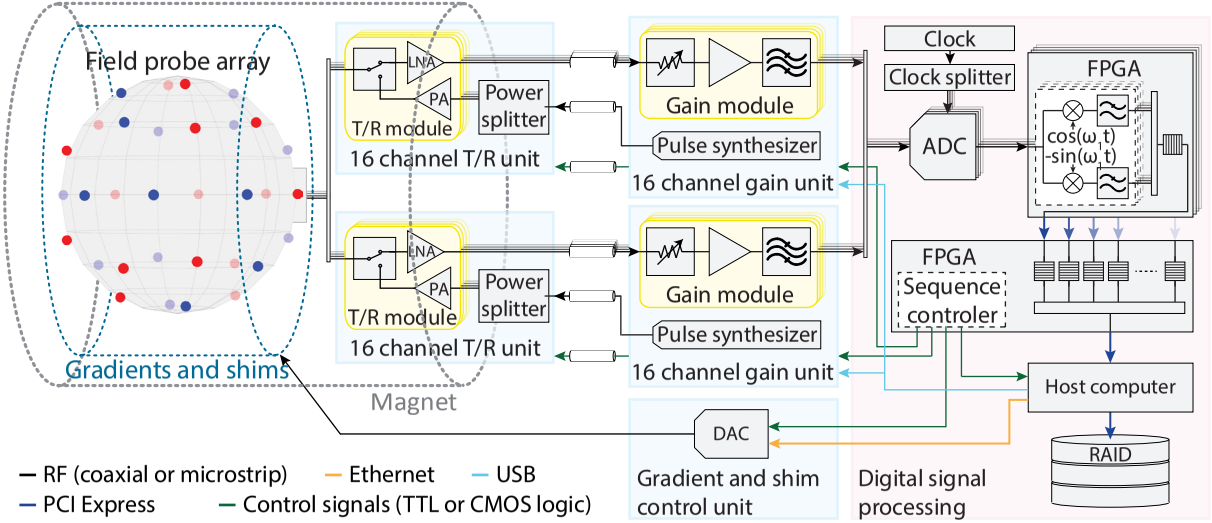

Figure 5.1: System overview comprising the 32 channel field probe array, two sets of T/R and gain units with 16 channels each, the digital signal processing, and shim control unit.

Order	**Spherical harmonic**	**Field coefficient**	**Phase coefficient**
0	1	B_0	k_0
1	x	G_x	k_x
	y	G_y	k_y
	z	G_z	k_z
2	xy	B_4	k_4
	yz	B_5	k_5
	$2z^2 - (x^2 + y^2)$	B_6	k_6
	xz	B_7	k_7
	$x^2 - y^2$	B_8	k_8
3	$3yx^2 - y^3$	B_9	k_9
	xyz	B_{10}	k_{10}
	$5yz^2 - y(x^2 + y^2 + z^2)$	B_{11}	k_{11}
	$2z^3 - 3z(x^2 + y^2)$	B_{12}	k_{12}
	$5xz^2 - x(x^2 + y^2 + z^2)$	B_{13}	k_{13}
	$z(x^2 - y^2)$	B_{14}	k_{14}
	$x^3 - 3xy^2$	B_{15}	k_{15}

Table 5.1: Real-valued spherical harmonics used as spatial basis functions, field coefficient names and shim coils used to produce corresponding fields.

re-excitation. A trigger signal from the scanner was used to synchronize the monitoring system with the scanners sequences, as described in Section 4.2.3.

Field Probe Array

Field probes built from a 2.2 mm inner diameter glass capillary filled with H_2O and doped with $GdCl_3.6H_2O$ such that $T_2 \approx 88\,\mu s$ and $T_1 \approx 105\,\mu s$ were used. ^1H based field probes are favorable for impulse response measurements due to their high sensitivity given by the high gyromagnetic ratio [20] and spin density. A disadvantage is the abundance of ^1H signal sources emitting spurious NMR signals. Therefore polytetrafluorethylene (PTFE) was used for mounting, as substrate for printed circuit boards, and as dielectric in coaxial cables (Multiflex 86, Huber-Suhner, Herisau, Switzerland). Furthermore fluxless solder wire was employed with a minimum of separately added flux for soldering. Thorough ultrasonic cleaning after soldering made sure that remaining flux was removed. A 5-turn solenoid, built from uncoated copper wire of 120 µm diameter, was used as T/R-coil. Small gaps between the coil windings ensured that the coils were short circuit free. A thin layer of solvable Teflon AF 1600 (DuPont, Wilmington, Delaware, USA) was used to fix the coil windings on the glass capillaries. Tuning and matching capacitors were directly soldered onto the coaxial cable as shown in the close-up of Fig. 5.2.A.

Typical human MRI gradient systems spread the frequencies of free induction decay signals (FID) over a range of several hundred kHz, depending on the gradient strength and imaging volume. On the other hand the bandwidth of the dynamic fields (i.e. gradients and shims), and thereby also the bandwidth of the phase evolutions of the field probes FIDs, is typically smaller than 30 kHz. Thus coupling between field probes, spread over a couple of hundred kHz, leads to erroneous phase components with large bandwidths that do not correspond to actual field dynamics. For the employed

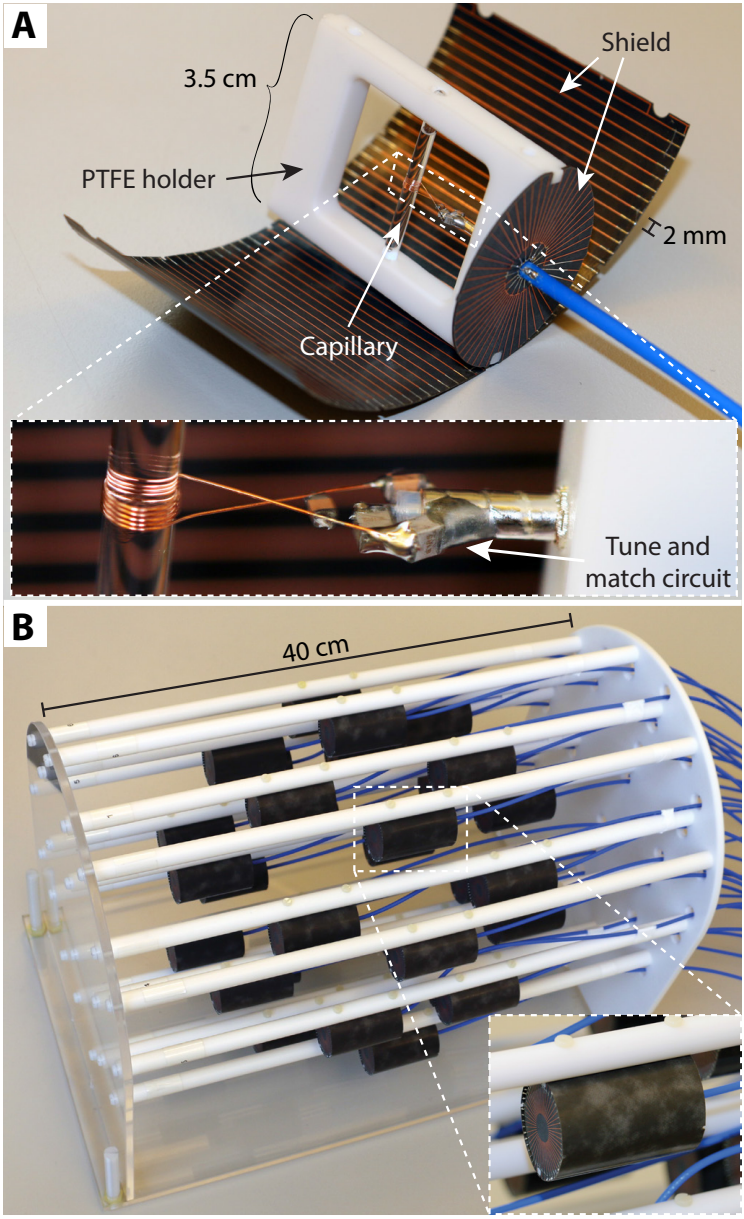

Figure 5.2: Field probe with open shield and close-up of the solenoid and tune-match circuit (A). Fully assembled field probe array and close-up of a probe with closed shield (B).

continuous monitoring method this larger apparent bandwidth also leads to violation of the essential bandwidth limitation, required to recover the field during probe re-excitation (see Section 4.2.4). Especially if high channel counts are involved coupling becomes hard to tackle. Several effects lead to probe coupling, such as inductive and capacitive coupling between the coils and electronics, as well as imperfect balancing of the coils due to the tune-matching circuits and resulting shield currents on the cables. As a consequence a gradient compatible RF shield built from 200 µm wide copper tracks on a bendable PCB (RT/duroid 5880, Rogers Corporation, Connecticut, USA) was used, as illustrated in Fig. 5.2.

A PTFE and Polymethylmethacrylate (PMMA) based structure formed the basis of the used 32 channel field probe array. The probes were mounted such that they were face-centered on a soccer-ball polyhedron with a diameter of 22.5 cm, as shown in Fig. 5.2.B. Optimal set affiliation of the probes, for 2-set operation, was determined by minimization of the conditioning number of the calibration matrix used for spatial field expansion (see Section 1.2.2 and Ref. [21]) and is indicated by coloring in Fig. 5.1.

High-Level Data Processing

Once a train of FIDs from the rapidly re-excited, alternated probe sets was acquired, the phase of the currently active probe set was extracted and spatially expanded on a real-valued spherical harmonic basis (Tab. 5.1) as described in Section 1.2.2. Therefore probe positions were first calibrated by field measurements under constant reference gradients of $5\,\mathrm{mT\,m^{-1}}$ strength, sequentially activated in x, y and z direction. Optionally an expansion based on a basis created by field footprints from the gradient and shim coils, from here on called shim basis, was used. To determine the shim basis each gradient and shim coil was separately driven with a unit value and corresponding measured reference fields were used as basis for the spatial expansion. After spatial expansion the field evo-

lution was extracted by derivation, and the remaining re-excitation gaps were recovered using the knowledge about bandwidth limitation of the dynamic field evolution, as described in Section 4.2.4, resulting in a continuous field time course.

For better comparison of the effect size of higher-order field components, fields were scaled to the maximum value within a sphere of 20 cm diameter. In case of the shim basis the fields were scaled to the maximum value of the calibrated basis pattern.

5.2.2 Scanner and Shim Hardware

A whole-body 7 T Philips Achieva system (Philips Healthcare, Cleveland, OH, USA) with full 3^{rd} order spherical harmonic shim coils was used for the experiments. Tab. 5.1 lists the real-valued spherical harmonic basis functions up to 3^{rd} order and the corresponding shim names. This system has actively shielded gradient coils which also act as 1^{st} order shims, an actively shielded 0^{th} order shim coil, and two coils for Z2 fields (actively shielded Z2sh, and unshielded Z2).

In order to be able to play out custom waveforms on the shim channels, the system was equipped with a set of digital-to-analog converters (DAC) (National Instruments, Austin, USA) connected to the analog input of the shim amplifiers (Resonance Research Inc., Billerica, USA), operating at a rate of 25 kS/s (16 bit). The gradient channels (1^{st} order shims) were controlled over a custom built summation box, adding the demands from a second set of DACs and the scanner. Due to gradient duty-cycle safety reasons the maximum field that could be added by the DACs was limited to $2\,\text{mT}\,\text{m}^{-1}$. These DACs operated at a rate of 100 kS/s (16 bit) in order to deliver full control over the wider bandwidth of the gradient system. An Ethernet connection was used to transmit waveforms to this shim control unit and trigger signals generated by the sequence control FPGA of the monitoring system were used for accurate sample timing, as illustrated in Fig. 5.1.

The scanners RF transmit chain was disabled during all experiments to prevent it from interfering with the field camera, operating in the same frequency range (^{1}H based probes).

5.2.3 Experiments

Single-Shot Impulse Response Function Measurements

Impulse response functions were measured using frequency swept pulses as suggested in [41]. Frequency swept pulses spread the energy both in time and frequency, allowing for arbitrary input energy per frequency and bandwidth by a suitably long pulse. In this work 10 s long pulses of different bandwidth were used. A bandwidth of 30 kHz was selected for the measurement of gradient impulse response functions and bandwidths of 3 kHz and 5 kHz for shim impulse response functions. The sweep was set such that sensitivity was increased towards lower frequencies. Respective pulses were played out consecutively on each shim channel, through the gradient and shim control unit (Fig. 5.1). At the same time the field probes were operated in a single-set configuration to measure the field response. The small field excursions generated by the shim coils and the gradient summation unit cause only negligible probe dephasing, suggesting, according to Chapter 4 that a single-set configuration is preferable due to the SNR gain when all 32 probes are used together. After calculation of the spatio-temporal field evolutions the impulse response functions were retrieved by division in the frequency domain and smoothed, as described in Ref. [41]. Since a full 3$^{\text{rd}}$ order spherical harmonic field model was expanded (Tab. 5.1), self- and cross-terms were measured within a single acquisition. The resulting response functions were then scaled to the DC value of the self-term, for better comparison. Due to the use of a custom shim control unit, the scanner manufacturers software-based gradient pre-emphasis is not included in the characterization.

Sequence Monitoring

A single-shot echo-planar imaging (EPI) sequence with an in plane resolution of 3 mm × 3 mm, a field of view (FOV) of 220 mm × 200 mm and an echo time (TE) of 25 ms was measured using the field camera in the 2-set configuration. Multiple sets are beneficial in this case due to the large gradient moments, as suggested by the results from Chapter 4. Spatial field expansion was performed on a full 3^{rd}-order spherical harmonic basis (Tab. 5.1). To investigate the origin of field oscillations the experiment was repeated with different measures to reduce potential vibrations of the camera. The first measurement was without any additional damping, the second with rubber dampers, and the third with approximately 3 cm of foam underneath the field probe array.

Dynamic Shimming

A series of single-shot EPIs (resolution = 1.25 mm × 1.25 mm, FOV = 180 mm × 50 mm, TE = 20 ms) with slice wise shimming, representing a typical accelerated fMRI experiment, was monitored. Again the 2-set configuration was employed. The shim updates were controlled by the custom shim control unit. Spatial field expansion was based on the shim basis. Two measurements were performed, one including only the shim updates and one including the full sequence with all gradients and shims.

5.3 Results

The achieved probe sensitivity according to [20] was $\xi = SNR\sqrt{BW} = 2.16 \times 10^6\sqrt{Hz}$. The worst case coupling between two probes at a distance of 5 cm, which is roughly equivalent to the smallest distance between two probes in the array, was less than -78 dB. If the whole receive chain with all amplification stages is taken into account the worst case coupling between all channels was -56 dB.

The sensitivity of the measured continuous field time courses, inside a typical spherical imaging volume of 20 cm diameter, was in the range of 300 nT at a bandwidth of 30 kHz (2-set configuration). This is roughly a factor of 1.6 larger than the simulated sensitivity due to probe SNR, decay constants and flip angle. Several effects lead to this deviation, such as non-linear phase components due to inhomogeneous fields and detection sensitivities inside the probe droplet, and residual spin echoes due to fast re-excitation, as detailed in Chapter 4.

5.3.1 Single-Shot Impulse Response Function Measurement

Figures 5.3, 5.4 and 5.5 show results from the impulse response function measurements. The used input chirp, as well as the time domain response of the XY term is depicted in Fig. 5.3.A. The corresponding impulse response function in the frequency domain is shown in Fig. 5.3.B. This 2^{nd}-order term, as well as the 3^{rd}-order Z(X2-Y2) term in Fig. 5.5.A, are plotted together with data obtained from measurements with long-lived field probes as described in [41]. A high degree of agreement can be observed, especially considering that the measurements were taken several months apart.

Effects of long-lived eddy currents are shown in the unshielded Z2 term in Fig. 5.3.B, and the 3^{rd}-order terms in Fig.5.5.A, in the form of Lorentzian peaks at the center of the spectrum.

Differences in the noise levels, nicely visible in the comparison of the shielded and unshielded Z2 terms in Fig. 5.3.B, are related to the smaller field response generated by the shielded shim coil. A weaker field response leads to less SNR in the response function if the noise level, which depends on probe SNR and on actual field noise, stays constant. Since the probe SNR and the actual field noise do not significantly change due to the applied fields and therefore do not scale with the response, the apparent increase in noise is actually a consequence of scaling the signal with less SNR

to its DC value.

A selection of cross-terms is shown in Fig. 5.5.B. The arrows indicate the direction of the cross-term, e.g., Y $\rightarrow$ ZY shows the response in the ZY field term due to driving of the Y channel.

5.3.2 Sequence Monitoring

Figure 5.6 shows measured field evolutions during a single-shot EPI sequence, including slice-selection and higher-order fields. One static shim (X2-Y2 channel or B_8 coefficient) was enabled during the whole sequence for demonstration purposes. Several effects can be observed in the field evolutions, such as eddy currents and oscillations. Eddy currents can be deduced by their temporal alignment with switching of strong gradients, such as visible in the B_0 term and some higher-order terms at the beginning of the sequence. Strong oscillations on the other hand are visible during and after the EPI readout in several field terms. The close-ups in Fig. 5.6 show that the oscillations are very prominent in the Gy term after the actual EPI readout. Results with different camera damping measures are superimposed in different colors for the selected field terms in the close-ups. The very high degree of agreement between the damping measures (almost completely covered by the foremost result with no damping) suggests that the field oscillations do not originate from mechanical oscillations of the field camera. If the camera would oscillate, one could expect changes in the decay constants depending on the damping measure. The decay of the primary oscillation is illustrated with an exponential fit. A look at the spectral components of the field terms during and after the EPI readout, as can be seen in the frequency domain plots underneath the close-ups, reveals slight frequency shifts between the oscillations during the EPI readout and after the readout. The frequencies of the free oscillation (after the EPI readout) correspond quite nicely with the resonances in the Y-gradient impulse response function and Y $\rightarrow$ Z2Y cross-term shown in Fig. 5.4.

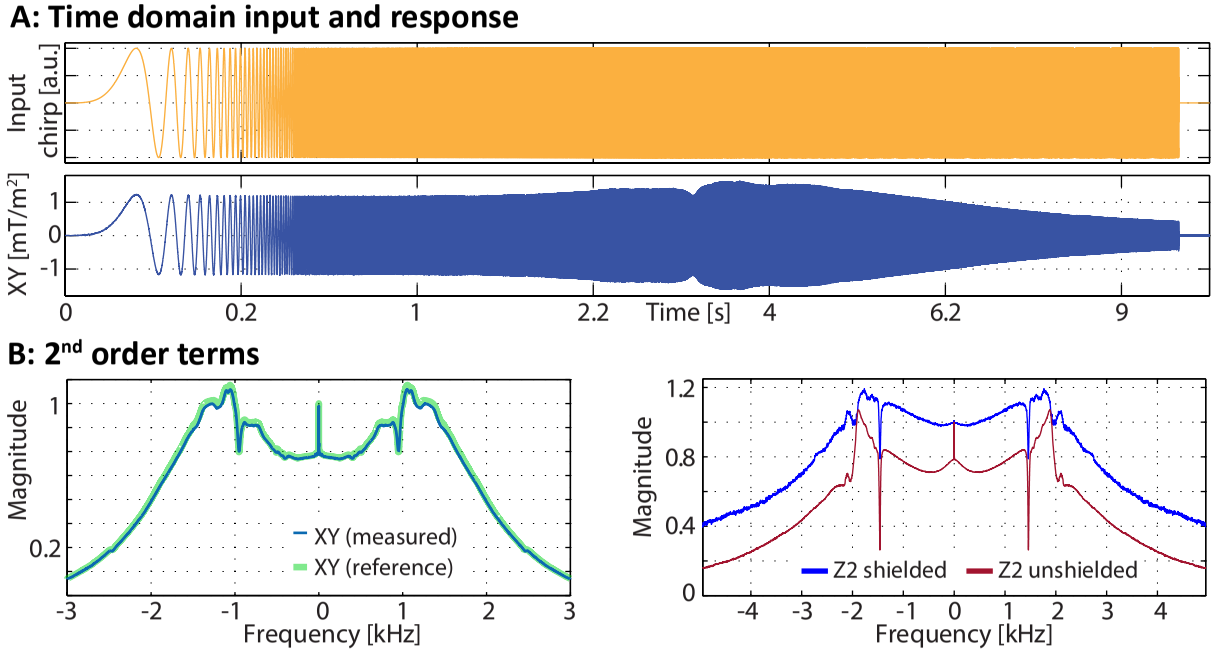

Figure 5.3: Time domain input chirp and corresponding time domain self-term response of the XY shim channel plotted on a quadratic time axis (A). Corresponding impulse response function of the XY term in the frequency domain (thin blue line, B) and reference data measured with long-lived field probes (thick light blue line, B), as well as shielded and unshielded Z2 shim terms (B).

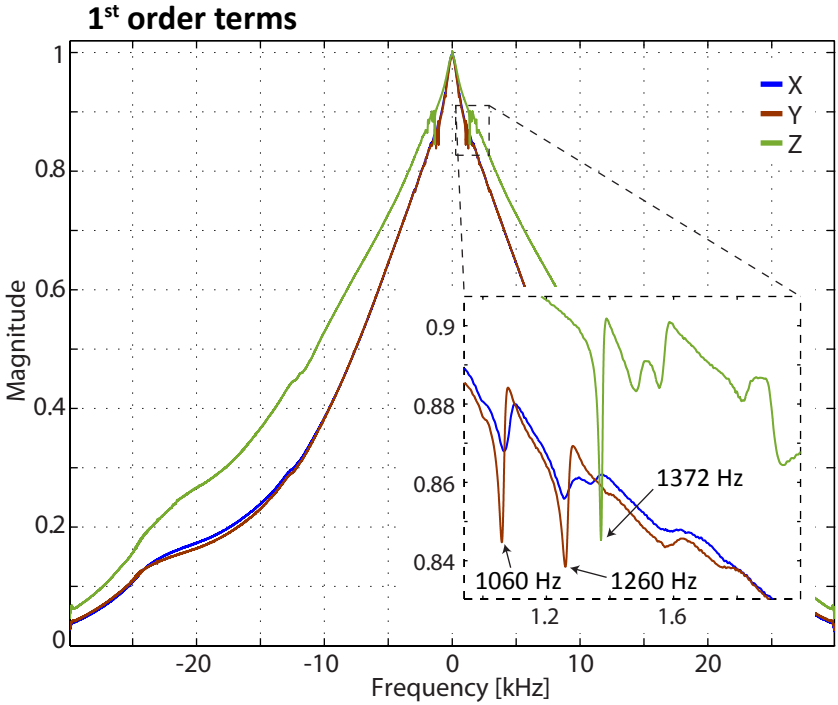

Figure 5.4: Impulse response functions of the gradient terms and close-up of resonances.

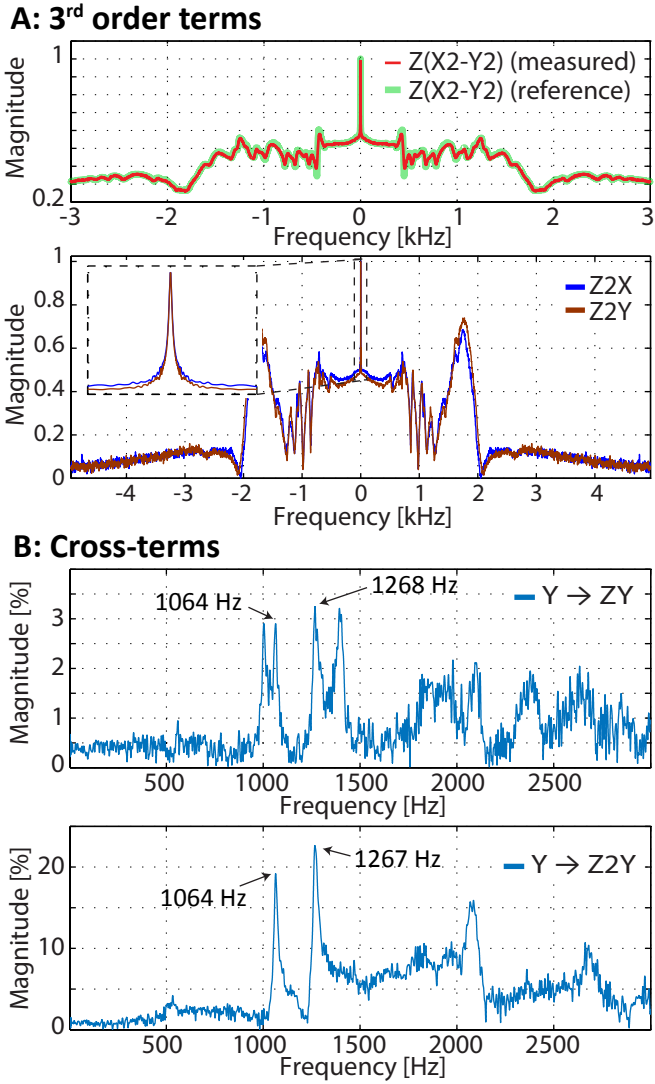

Figure 5.5: Selection of 3rd-order terms with comparative data from measurements with long-lived field probes (A), and a selection of cross responses in percent of the corresponding self-term (B).

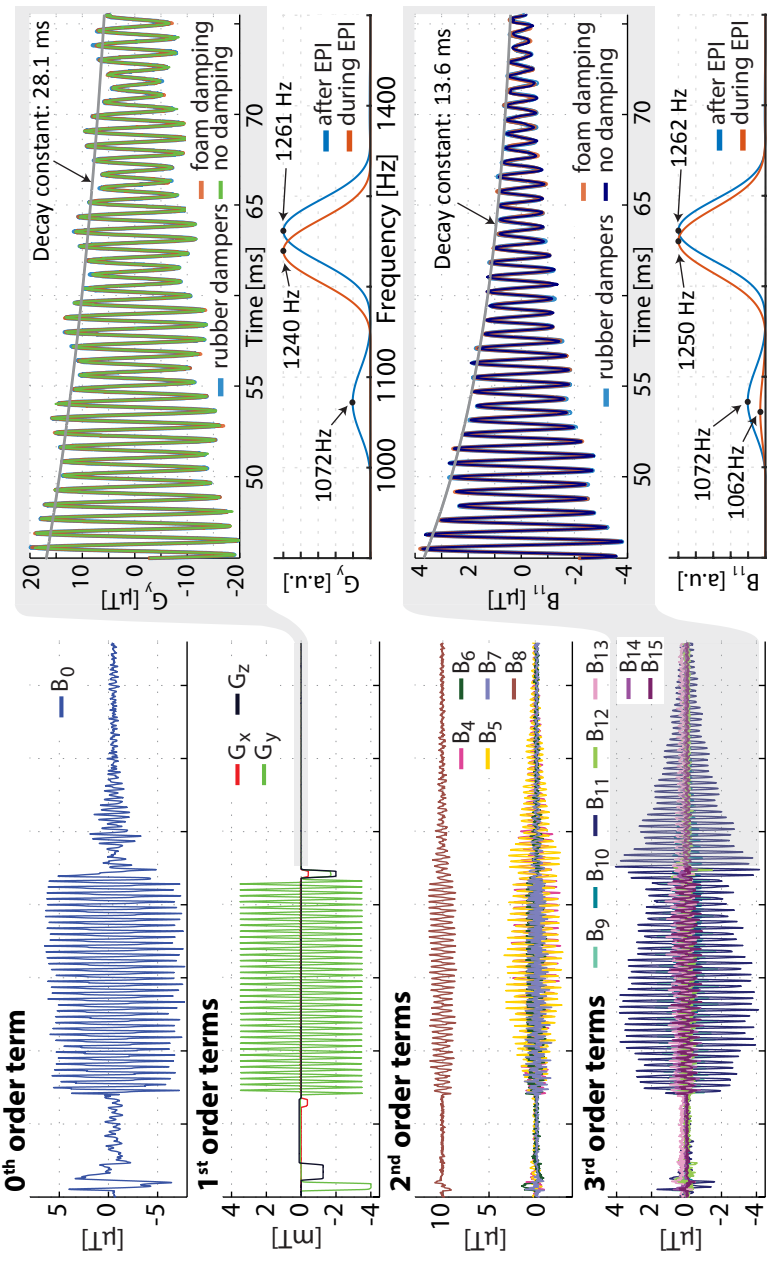
0th order term
1st order terms
2nd order terms
3rd order terms
Time [ms]
Decay constant: 28.1 ms
foam damping
no damping
rubber dampers
1261 Hz
1240 Hz
1072Hz
after EPI
during EPI
Frequency [Hz]
Decay constant: 13.6 ms
1262 Hz
1250 Hz
1062Hz

Figure 5.6: Excerpt of a single-shot EPI sequence and corresponding field evolutions (1^{st} order fields are filtered to 30 kHz, others to 5 kHz, for improved visibility). The close-ups show selected fields under different camera damping conditions. Frequency domain plots underneath the close-ups show the main frequency components of the corresponding fields during the EPI readout and during the zoomed decay period after the EPI readout.

5.3.3 Dynamic Shimming

Field excerpts of the scans with dynamic shim updates are shown in Figs. 5.7 and 5.8 with and without enabled 1^{st}-order spatial encoding fields.

Again eddy currents due to switching of strong gradients can be observed, as well as oscillations in the 0^{th}, 2^{nd} and 3^{rd}-order terms during the EPI readout, which are most likely related to gradient cross-terms and also eddy currents. The observed amplitude of these oscillations is in the same range as the actually applied shim updates. The oscillations vanish if the EPI gradients are disabled as can be seen by comparison of Figs. 5.7 and 5.8. There are no strong oscillations after the EPI readout compared to the previous EPI example shown in Fig. 5.6, which is most likely due to the changed EPI frequency (main component: 734 Hz). This frequency does not coincide with a resonance of the gradient system.

Further it can be seen that the shim system does not reach the demands within the given slice periods of 100 ms, which is related to very long-lived eddy currents that also manifest themselves in the mentioned Lorentzian curves of the impulse response functions (cf. Fig. 5.5).

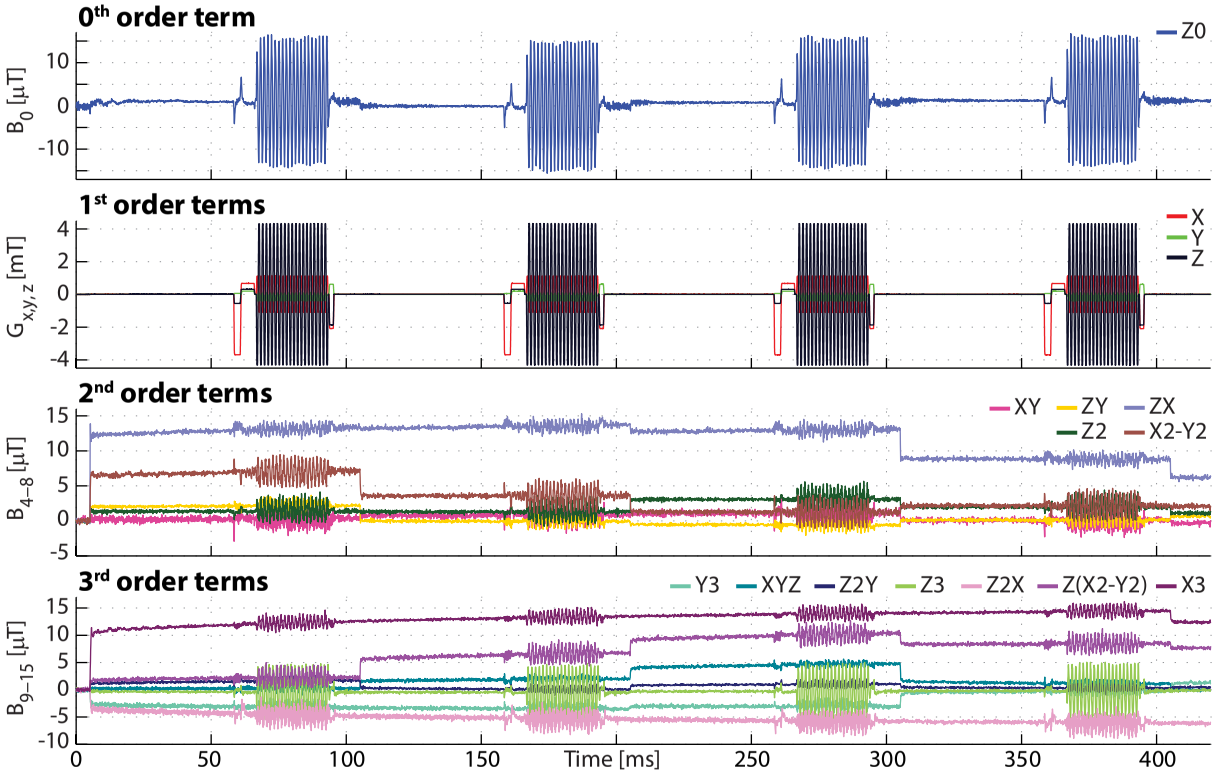

Figure 5.7: Excerpt of the field evolutions during a multi-slice EPI sequence with dynamic shim updates (1^{st} order fields are filtered to 30 kHz, others to 5 kHz, for improved visibility).

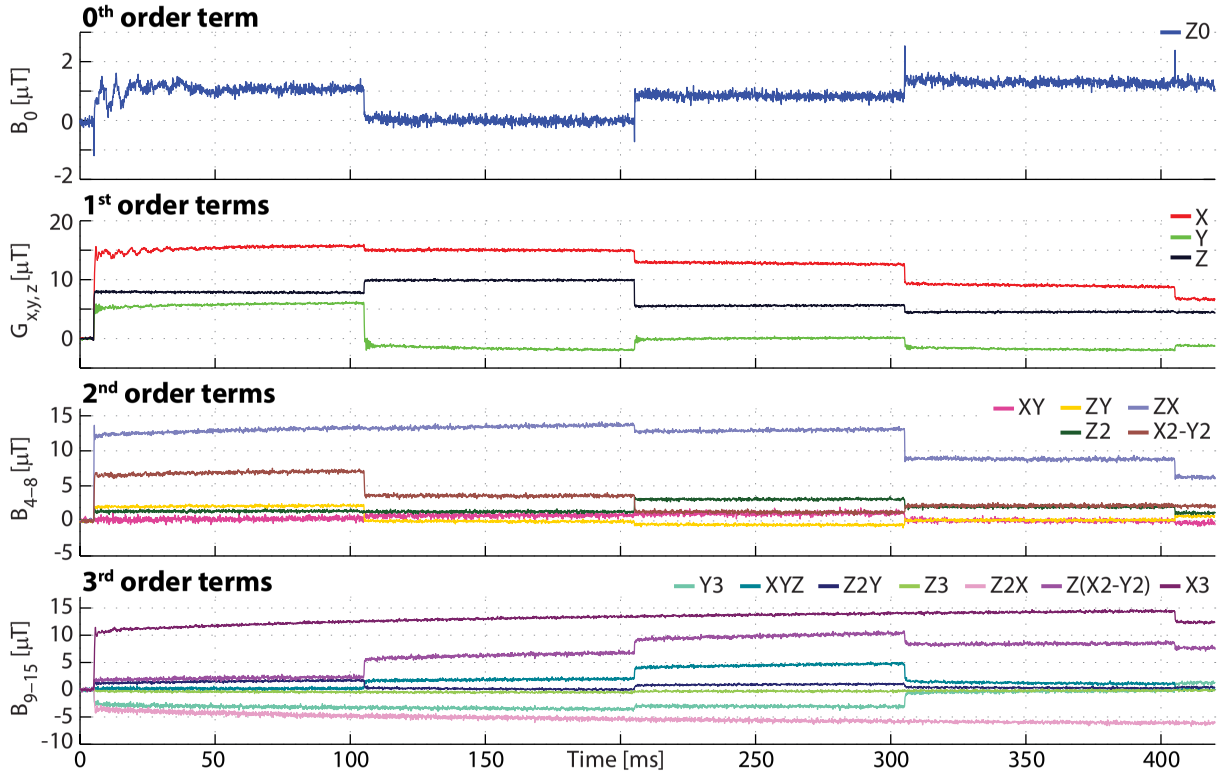

Figure 5.8: Excerpt of the same multi-slice EPI sequence shown in Fig. 5.7, but without the actual gradient pulses of the sequence used for signal encoding (filtered to 5 kHz, for improved visibility).

5.4 Discussion

Continuous magnetic field monitoring based on rapid re-excitation of alternated, short-lived NMR probe sets was successfully extended to 3rd-order spatial field expansions. A stand-alone continuous monitoring system was therefore revised and extended with regard to probe design, channel count and provisions for increased digital data flow, enabling continuous monitoring of higher-order field dynamics over arbitrary durations, only limited by data storage space and without the need to modify the sequence or system under study. The improved field probe design with RF shielding provides a very high degree of inter-probe coupling suppression, enabling construction of dynamic field cameras with large probe counts and high field measurement precision. The difference between the coupling of two probes (-78 dB) and the coupling at the end of the receive chain (-56 dB) leaves room for further optimizations, as for example by means of receive chain coupling characterization and corresponding digital data correction. Further field probe improvements comprise reduction of spurious ^{1}H signals from solids in close proximity of the NMR active droplet and excitation fields.

The demonstrated ability to measure gradient and shim impulse response functions with high resolution and within a single-shot of just a few seconds, 20 times faster than previous field probe based methods [41], holds the potential for new system analysis approaches, such as analysis of changes due to temperature drifts and system aging. This capability might furthermore enable new remote system diagnostic methods and prediction of system failures by means of machine-learning approaches.

The correlation between the observed oscillations in the single-shot EPI shown in Fig. 5.6 and the resonance in the Y-gradient impulse response function (Fig. 5.4), as well as Y $\rightarrow$ Z2Y cross-term (Fig. 5.5.B) illustrates the effect of driving the system close to its

resonance frequencies. This results in field oscillations, which are most likely related to mechanical oscillations of the gradient coils. These oscillations can then lead to increased system heating and as a result field drifts in long scan session with many EPI readouts, such as used in typical fMRI experiments and studied in [37].

Monitoring of an EPI sequence with dynamic shim updates (cf. Figs. 5.7 and 5.8) revealed eddy current and cross-term related 0^{th}, 2^{nd} and 3^{rd} order fields during the EPI readouts with magnitudes in the same range as the actual dynamic shim fields themselves. Further, slow shim field settling could be identified. These observations call for effective shim pre-emphasis filters with full cross-term compensation, which can be designed based on the measured impulse response functions [74].

Different basis functions can be selected for spatial field expansion, such as a spherical harmonic basis or a basis built from field patterns generated by respective gradient and shim coils. Spherical harmonics represent a mathematical solution of the Laplace equation, which describes magnetic fields in free space, in a convenient Euclidean coordinate system. A field pattern based expansion on the other hand represents the fields in terms of driving ports of a linear time-invariant system. Using the latter (shim basis) is advantageous if the resulting field evolutions are used for calculation of pre-emphasis filters [74] or for real-time field updates [32], since they directly represent the field patterns generated by the driving sources which are to be controlled. Such a field pattern or port based expansion is also advantageous if the available coils only approximate the ideal spherical harmonics, and a large number of basis functions is needed for accurate spatial expansion, resulting in the need for an increased number of probes. This is especially associated with high cost if multiple, alternated probe sets are used. Multi probe-set monitoring is very sensitive to incomplete basis sets. If higher-order field terms are present that cannot be resolved with the available basis functions, they are projected onto

the available terms. This projection is different for each probe set, resulting in concatenation of not only erroneous, but also inconsistent field evolutions.

6 Probe Calibration in k-Space and Time Domain

Partially published in:

- *"k-t-Calibration improves continuous field monitoring for image reconstruction"*. Dietrich, Benjamin E.; Wilm, Bertram J.; Brunner, David O.; Duerst, Yolanda; Barmet, Christoph; Pruessmann, Klaas P. *In Proceedings of the Annual Meeting of ISMRM*, Milano, Italy, 2014. Abstract 1842.

6.1 Introduction

Typical short-lived continuous monitoring probes, as presented in Chapters 4 and 5, exhibit small systematic phase distortions during their coherence lifetime (see Section 4.3 and Fig. 6.1). These errors, in the range of a few mrad, are caused by: internally and externally induced B_0 field inhomogeneities inside the NMR active probe droplets, non-uniform excitation and detection sensitivities, spectral impurities and inhomogeneous relaxations of the NMR active material, as well as by imperfections of the receive electronics. When concatenating the train of field measurements and interpolating the short probe re-excitation gaps (10 µs to 20 µs range) to achieve a continuous temporal coverage, as presented in Chapter 4, these distortions form the dominant source of error (see Section 4.3.1). They result in interpolation inconsistencies (jumps) between readouts and probe sets and may even be further amplified by this processing step. Consequently, in the measurement of a constant field, peaks with the frequency of the inverse set alterna-

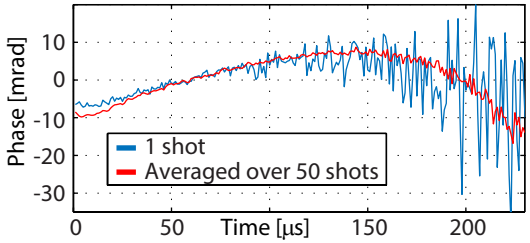

Figure 6.1: Non-linear phase residual of a typical continuous monitoring probe, acquired under a constant gradient of 40 mT m^{-1} (^{1}H compound, $T_2 \approx 88$ µs).

tion period $1/(T_{set})$ and multiples thereof appear in its spectrum. If k-space trajectories are integrated from the obtained continuous field evolutions, these systematic errors accumulate over time, limiting the usefulness of such trajectories for image reconstruction. The method presented in this chapter aims to reduce these errors by means of probe calibration in the joint k-space and time domain.

6.2 Theory

Ideally the phase of a field probe's FID is proportional to the integral of the magnitude of the magnetic field since the last probe excitation (Eq. 1.2) and the field dynamics can be spatially expanded inside a volume of interest by measurement with a surrounding array of field probes as detailed in Section 1.2.2. However, this approach assumes that the static longitudinal background field B_0 and transverse probe excitation fields B_1 have uniform distributions inside the NMR active droplets, and hence, that the probes act as pure point sources. This assumption is challenged, especially towards larger probe diameters and when susceptibility matching of surrounding materials is difficult due to spurious signals emitted

by these materials, such as in the case of the short-lived ^{1}H-based field probes presented in Chapters 4 and 5. But also objects in close proximity can distort the field uniformity inside the NMR active droplet.

By taking the non-uniform field distributions inside a probe into account, the probe phase can be modeled as:

$$\phi(t) = \angle \int_V M(\mathbf{r}) \mathrm{e}^{-i\gamma \int_{t_0}^{t} |\mathbf{B}(\mathbf{r},\tau)| \mathrm{d}\tau} \mathrm{d}^3 r \tag{6.1}$$

where M denotes the distribution of the transverse magnetization inside the probe droplet volume V. In terms of k-space notation this phase can be written as:

$$\phi(t, \mathbf{k}(t)) = (\mathbf{k}(t))_0 + \widehat{\phi}(t - t_0, \mathbf{k}(t)) \tag{6.2}$$

with $\mathbf{k}$ being the k-space phase coefficients, $(\mathbf{k}(t))_0$ the 0^{th} order k-space phase coefficient of $\mathbf{k}$, which is B_0 dependent, t_0 the last excitation time, and $\widehat{\phi}$ the probe's k-t-dependent phase evolution.

The probe-dependent k-t-phase-evolution $\widehat{\phi}$ is constant and can hence be calibrated in a scan where the k-space trajectory is known with high fidelity, such as in a center-out acquisition with settled, static fields. This means that one needs to know, and hence measure the probe phase under all possible k-space excursions, which is equivalent to all possible gradient strengths and directions, in the case of center-out acquisitions. In practice such a phase map is smooth in time and $\mathbf{k}$, allowing for interpolation based on a sufficiently densely sampled subset of measured phase evolutions. The actual k-space trajectory $\mathbf{k}$ of any measured sequence can then be retrieved by means of a non-linear least squares fit:

$$\min_{\mathbf{k}} \left\| \sum_{i=1}^{N} \left(\phi_i(t, \mathbf{k}(t)) - \left((\mathbf{k}(t))_0 + \widehat{\phi}_i(t - t_0, \mathbf{k}(t)) \right) \right)^2 \right\| \tag{6.3}$$

where the index i denotes the i-th probe in the set of size N. In order to get a distinct solution to this minimization problem, the

total number of probes N needs to be equal or larger than the number of spatial basis functions, and the phase maps $\widehat{\phi}_i$ need to be strictly monotonic in $\mathbf{k}$.

6.3 Methods

6.3.1 Hardware

The stand-alone continuous field monitoring system introduced in Chapter 4 was used with the adjustable ^{1}H-based 16-channel field probe array introduced in Section 4.2.1 ($T_2 \approx 70\,\mu s$), and the 32-channel array introduced in Section 5.2.1. Both arrays were only used in the 2-set configuration. All experiments were performed on a whole-body Philips Achieva 7 T MRI system (Philips Healthcare, Cleveland, USA). Imaging experiments employed a commercially available 16-channel head receive array.

6.3.2 Phase Map Generation

In order to integrate a large subset of all possible probe phase evolutions into the phase calibration maps $\widehat{\phi}$, and to be able to interpolate missing parts efficiently, a grid of different gradient strengths and directions was selected, as illustrated in Fig. 6.2.A. The scanner was then programmed to cycle through all these configurations and to apply each gradient for a period of 500 ms. Within each cycle a series of 50 probe FID's was acquired with a repetition period of 7 ms. An initial delay of 150 ms was added in front of each acquisition series to make sure that all fields have settled. Each probe's phase was then extracted and averaged over all 50 shots, resulting, together with the integral of the corresponding nominal gradient value over the acquisition time ($\mathbf{k} = \gamma\,\mathbf{G}\,t$), in high SNR phase maps with a phase value for each k-space grid and time point. Figure 6.2.B shows exemplary data. Spline interpolation was used

to interpolate the phase maps within the calibrated range and linear extrapolation was used to interpolate values outside the range. Figure 6.2.C shows an interpolated 1D phase map over a typical probe readout duration of 110 µs along the k_z axis, and Fig. 6.2.D the same phase map without the linear part. Subtracting the linear phase given by the gradient demand reveals the non-linear phase residuals in the mrad range.

6.3.3 Non-Linear System Solving

The non-linear minimization problem from Eq. 6.3 was solved with the MATLAB (The MathWorks, Inc., Natick, Massachusetts, United States) implementation of the Levenberg-Marquardt algorithm. The dominating linear part and the high SNR of the phase maps ensured that the fitting algorithm did not converge to a local minimum.

Higher-Order Field Model

In order to use this method to reconstruct trajectories on for example a complete 3^{rd}-order spherical harmonic basis (cf. Tab. 5.1), one would need to extend the phase map's dimensions according to the number of selected basis functions. This is not practical and even impossible if the MRI system is not equipped with shim coils that can produce the respective static calibration fields.

To avoid such excessive calibration, a linear approximation approach was used and the higher-order k-space transformed into a probe-local 0^{th} and 1^{st}-order k-spaces. Therefore approximate probe positions $\mathbf{r}_p^G$ were calculated based on the calibration data sets and the higher-order basis functions f_n approximated at these positions using linearization:

$$f_n^{lin}(\mathbf{r}) = f_n(\mathbf{r}_0) + \nabla f_n|_{\mathbf{r}_p^G} \cdot (\mathbf{r} - \mathbf{r}_p^G). \tag{6.4}$$

A
B
C
D
t = 110 µs
Phase [rad]
Phase [mrad]
Non-linear phase [mrad]
Time [µs]
Gx [mT/m]
Gy [mT/m]
Gz [mT/m]
kx [rad/m]
ky [rad/m]
kz [rad/m]
kz [rad/m]

Figure 6.2: A: Equally spaced, 257 point calibration grid. B: 3D k-space phase map and corresponding phase values, 110 µs after probe excitation. C: Time domain view of the interpolated 1D phase map along the k_z axis. The dashed red line illustrates the corresponding phase values from part B. D: Same 1D phase map without the linear part. The black lines illustrate the time axis.

In terms of matrix notation this transformation can be formulated as:

$$\tilde{\mathbf{k}} = \mathbf{T}\,\mathbf{k} \tag{6.5}$$

where $\tilde{\mathbf{k}}$ denotes the probe-local 0^{th} and 1^{st}-order k-space and $\mathbf{T}$ the transformation matrix:

$$\mathbf{T} = \begin{pmatrix} f_0(\mathbf{r}_0) - \nabla f_0|_{\mathbf{r}_0} \cdot \mathbf{r}_0 & \cdots & f_N(\mathbf{r}_0) - \nabla f_N|_{\mathbf{r}_0} \cdot \mathbf{r}_0 \\ \frac{\partial f_0}{\partial x}\Big|_{\mathbf{r}_0} & \cdots & \frac{\partial f_N}{\partial x}\Big|_{\mathbf{r}_0} \\ \frac{\partial f_0}{\partial y}\Big|_{\mathbf{r}_0} & \cdots & \frac{\partial f_N}{\partial y}\Big|_{\mathbf{r}_0} \\ \frac{\partial f_0}{\partial z}\Big|_{\mathbf{r}_0} & \cdots & \frac{\partial f_N}{\partial z}\Big|_{\mathbf{r}_0} \end{pmatrix}. \tag{6.6}$$

The minimization problem from Eq. 6.3 can then be reformulated as shown in Eq. 6.7 and solved with the same algorithm and calibration data.

$$\min_{\mathbf{k}} \left\| \sum_{i=1}^{N} \left(\phi_i(t, \mathbf{k}(t)) - \left((\mathbf{k}(t))_0 + \widehat{\phi}_i(t - t_0, \mathbf{T}\,\mathbf{k}(t)) \right) \right)^2 \right\| \tag{6.7}$$

6.3.4 Experiments

Static Fields, Precision and Phase-Map Resolution

To assess the performance of the presented probe-phase calibration method, a series of continuous monitoring experiments were conducted under constant fields of different strengths and with different calibration grid resolutions. Static gradients were applied

and the field was monitored with 2 sets of 16 probes, over a period of 300 ms (set alternation period $T_{set} = 150\,\mu s$). A delay of 150 ms was introduced between the gradient onset and the monitoring acquisition to make sure that all dynamic fields have settled. A full 3^{rd}-order spherical harmonic field model, including the linear approximation for the higher-order terms, was fitted and scaled to the maximum value within a 20 cm sphere for better comparison of the effects. The measurement gaps, due to probe re-excitation, were recovered using a bandwidth limitation constraint of 30 kHz, as described in Section 4.2.4. The standard deviation of the field-time-course was then calculated and the root-mean-square value across all spatial orders used as a measure of sensitivity.

6.3.5 Higher-Order Fields

As an example of higher-order field monitoring the field evolutions during a diffusion weighted EPI sequence were measured with and without k-t-calibration. Again the 32-channel array was used in a 2-set configuration and a full third-order spherical harmonic field model with the linear approximation was fitted and scaled to the maximum value within a 20 cm sphere. The 0^{th}, 2^{nd} and 3^{rd}-order terms were subsequently filtered to a bandwidth of 4.5 kHz and the 1^{st}-order terms to 30 kHz, for better visibility, under the assumption that these fields originate mostly from the shim and gradient coils, which have different usable bandwidths [41].

Image Reconstruction Based on k-t-Calibrated Trajectory

The method was also tested for field monitoring based image reconstruction of a single-shot EPI acquisition (resolution = 1.5 mm, readout duration = 90 ms, max. gradient strength: $40\,mT\,m^{-1}$). First the trajectory was monitored with the adjustable ^1H 16-channel camera (2-sets of 8 probes each, $T_{set} = 110\,\mu s$, $T_2 \approx 70\,\mu s$), and then the camera was removed and a spherical phantom was

imaged. Data synchronization between the imaging data from the scanner and monitoring data from the stand-alone monitoring system was performed as described in Section 4.2.3. Image reconstruction was completed using iterative algebraic reconstruction as described in Ref. [45], but without coil sensitivity and B_0 maps, similar to the reconstruction in Chapter 4.

6.4 Results

6.4.1 Static Fields, Precision and Phase-Map Resolution

Figure 6.3 shows an excerpt of the first four acquisitions of a static field measurement with and without k-t-calibration, as well as the spectrum of the whole acquisition. The fields within the individual acquisitions show a small but clear bias in the reference method leading to distinct peaks in the spectrum of the field. These peaks are almost completely suppressed in the k-t-calibrated field measurement.

The results from the static field analysis under different gradient strengths and with different phase-map resolutions are shown in Fig. 6.4. As expected, the improvements due to k-t-calibration are larger under strong gradients due to the increase in field inhomogeneity inside the probes, which can also be seen in the phase map in Fig. 6.2.D. Increasing the phase-map resolution does not always produce better results, which supports the assumption that the phase maps can be interpolated from a rather coarse grid.

6.4.2 Higher-Order Fields

Figure 6.5 shows an excerpt of the diffusion weighted EPI sequence with and without k-t-calibration. The k-t-calibrated field evolutions show improvements primarily during the strong diffusion gradients (combined strength of $60\,\mathrm{mT\,m^{-1}}$). These gradients lead

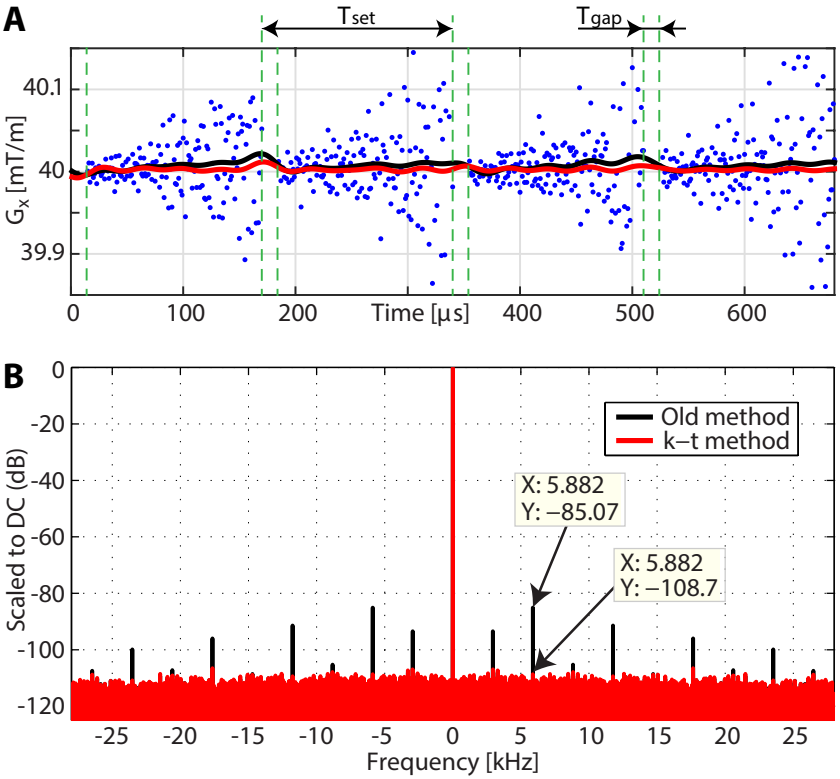

Figure 6.3: A: Excerpt of the first 4 set periods of a continuous monitoring experiment, acquired under a constant gradient of 40 mT m^{-1}, with a 2-set configuration and set alternation period of 170 µs. The blue dots in part A represent the raw data at a bandwidth of 1 MHz. The black lines represent the interpolated field evolution calculated with the reference method, and the red lines the interpolated field calculated with the k-t-calibration method, both at a bandwidth of 30 kHz. B: Frequency domain representation of the whole 300 ms scan.

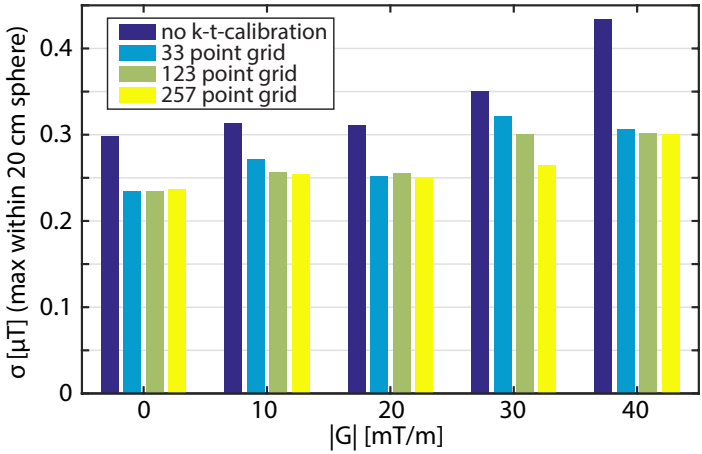

Figure 6.4: Comparison of the sensitivity of field measurements under constant gradients for different calibration grid resolutions, with and without k-t-calibration.

to a considerable degree of dephasing within the employed short-lived probes. Moreover, the large bandwidth required to excite all probes at the edge of the imaging volume limits efficient probe excitation. As a result the overall SNR is lower during the diffusion gradients. The offset in the B_0 term which appears in the reference method, is removed in the k-t-calibrated version.

6.4.3 Image Reconstruction Based on k-t-Calibrated Trajectory

A single-shot EPI trajectory of 90 ms duration and its corresponding phantom image is shown is Fig. 6.6. The close-up shows how the calibration affects the trajectory. The k-t-calibrated trajectory is stretched and slightly straightened compared to the reference method trajectory. In terms of artifacts this affects the recon-

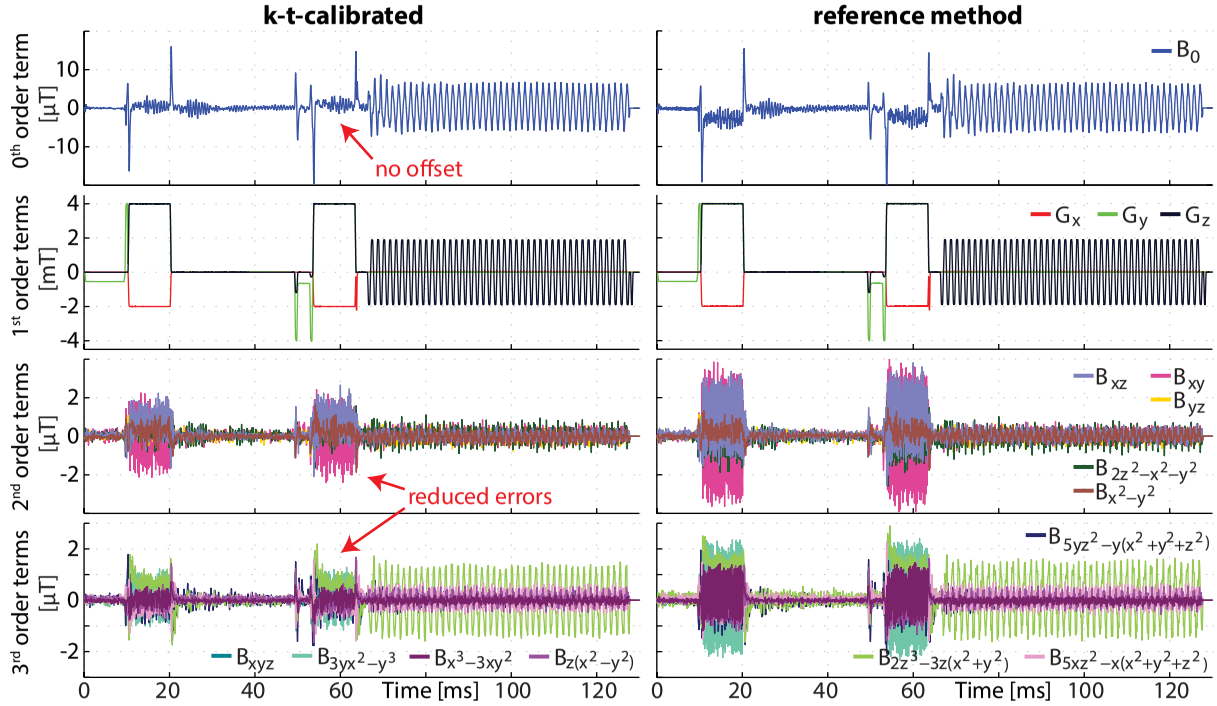

Figure 6.5: Excerpt of a diffusion weighted EPI sequence, reconstructed with and without k-t-calibration. Acquired with the 32 channel array presented in chapter 5 in a 2-set configuration of 16 probes each and with a set alternation period of 150 µs. The fields are scaled to the maximum value within a 20 cm sphere.

structed image to a small degree in the form of a slight shift and stretch, as can be seen in the difference image (Fig. 6.6.D). The overall ghosting level is remarkably low for both methods (Fig. 6.6.B and 6.6.C), considering the very challenging imaging task at 7 T. However, the logarithmically scaled images (Fig. 6.6.E and 6.6.F) reveal remaining artifacts and a slightly lower ghosting level in the image based on the k-t-calibrated trajectory (6.6.F).

6.5 Discussion

Actual phase evolutions of field probes consist of various components that do not directly correspond to the intended field measurement. Among them contributions due to receiver imperfections and point source violation. The presented probe phase calibration in k-space and time removes reproducible parts of such contributions successfully and improves concatenation of field measurements from multiple independent probe sets. It alleviates the need to know exact probe positions, which are not well defined in the case of large (droplet diameter grater than 1 mm) field probes.

Compared to the reference method, which determines probe positions in the image coordinate system based on a set of trusted reference gradients and applies a linear model to spatially expand the phase evolutions, the presented k-t-calibration method relies on densely sampled phase maps under ideally all possible field configurations and hence directly calibrates the demand of the system. Therefore it is inherently blind to gradient amplitude nonlinearities. In principle the phase maps could be corrected for this by correcting the linear part of the phase according to the gradient non-linearity. One could also directly retrieve the amplitude nonlinearity from the phase maps, by looking at the difference between the linear parts of the retrieved phases and comparing them to the ideal difference given by the demand. However, this would require a trusted reference gradient strength as well as a trust region in the

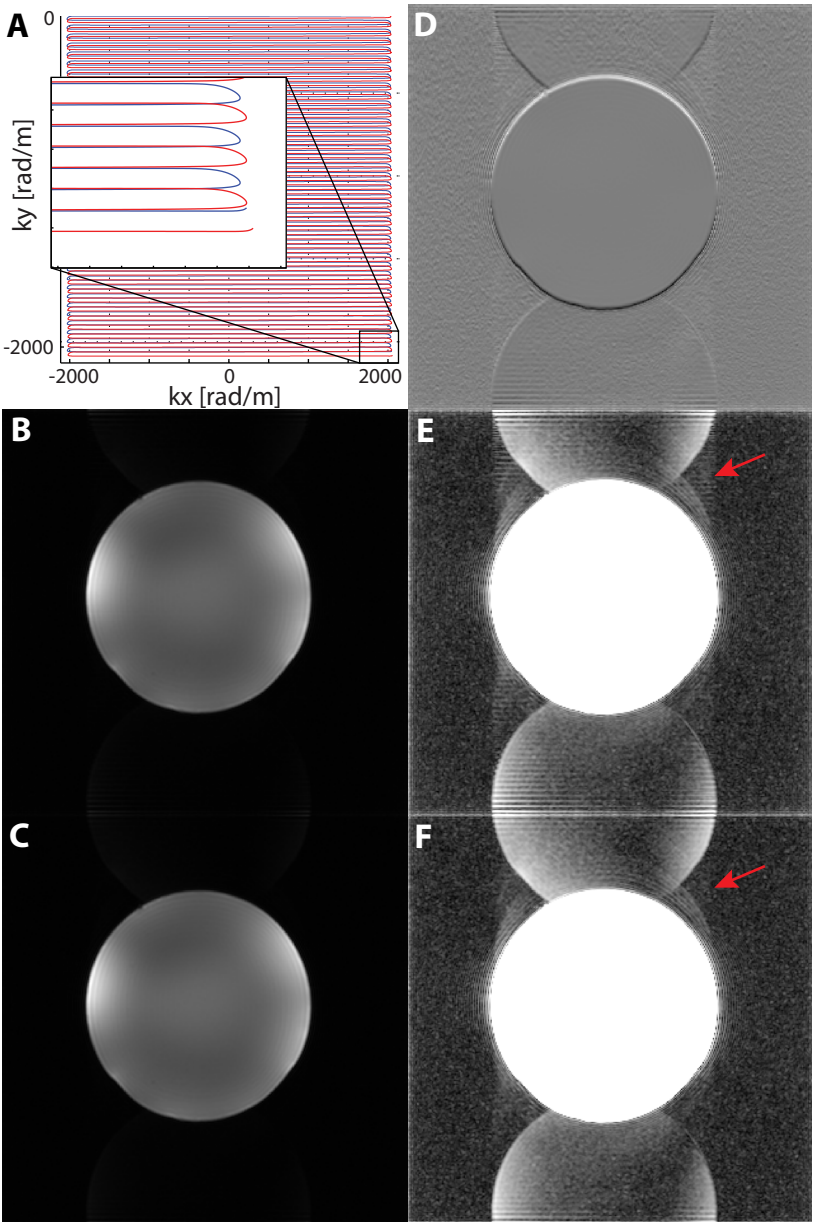
A
0
ky [rad/m]
-2000
-2000
0
2000
kx [rad/m]
D
B
E
C
F

Figure 6.6: Excerpt of measured single-shot EPI trajectory with (red) and without (blue) k-t-calibration (A), corresponding phantom images reconstructed on the trajectory without (B) and with (C) k-t-calibration, logarithmic representation of the image without (E) and with (F) k-t-calibration, as well as difference image of the logarithmic images (D). The red arrows indicate the slightly reduced ghosting.

time domain for the linear fit, which might not be a very robust solution due to the non-linear phase components.

Spatial gradient non-linearities on the other hand cannot be determined with either method, unless the probes are moved by known distances in space, or the positions are calibrated by other means, e.g. by knowing the exact mounting positions on a very precisely built probe array structure.

According to the Maxwell equations for the divergence and curl of the magnetic field, any activated linear field gradient produces additional magnetic fields with nonlinear spatial dependence [76]. These so called concomitant fields were not considered in the presented calibration method and might therefore represent a remaining error source that needs to be considered in future applications of this method.

In terms of numerical effort the presented method is very demanding due to the non-linear fit. Further optimizations would be beneficial to reduce the overall computation time. Acquisition of the phase maps on the other hand is fast, depending of course on the requested number of calibration gradients. As has been shown in Fig. 6.4, a relatively moderate number of calibration gradients is sufficient and requires, if properly optimized, scan time of less than a minute.

From an image point of view the presented reconstructed EPI image did not exhibit major improvements due to the k-t-calibrated

trajectory. The results might be more persuasive in cases where image geometry is of high importance and slight trajectory distortions have severe effects on the resulting image quality.

In principle this calibration can also be applied to single-coherence monitoring methods, such as presented in Chapter 2. However, probe dephasing under strong constant gradients would limit phase map acquisition and therefore the phase map generation approach would need to be reconsidered.

Overall it can be concluded that further investigations and optimizations are necessary towards routine application of this calibration method, especially with regard to concomitant field effects, gradient non-linearities and the excessive computation time.

7 Conclusions and Outlook

A scanner independent monitoring system based on NMR field probes has been developed, which delivers unrestricted camera-like access to spatio-temporal magnetic field dynamics in MRI systems, at high resolution and independent of the MRI system's operation state. A modular software defined radio approach was pursued in system design, making it a versatile tool for rapidly adapting research environments. This system was further equipped with RF waveform pickup capabilities, based on a dual-band receiver architecture, effectively extending it's monitoring capabilities beyond the low frequency longitudinal field dynamics. Further, a continuous monitoring method was introduced, alleviating previous restrictions of NMR probe based monitoring approaches with respect to acquisition duration and maximum gradient moment. Combined with the RF waveform monitoring capability, all relevant field dynamics for image formation and encoding could be observed on a common time basis, similar to a sequence diagram, but with actual field dynamics and disturbances.

Apart from the examples presented earlier in this thesis, this system has already been employed for a variety of other studies, such as real-time field feedback control for improved image acquisition and spectroscopy [32], [33], real-time motion correction based on head-mounted field probes [40], observation of longitudinal nuclear magnetization dynamics and advanced T_1 relaxometry [77], [78], and observation of cardiovascular magneto-dynamics [79], [80]. The underlying spectrometer hardware has also been used for sideband excitation experiments, permitting concurrent NMR excitation and detection by spectral separation of transmit and receive

signals [81], [82], and for zero echo time imaging [83].

Despite the achieved successes there are still several issues that need to be solved on the way to truly comprehensive, continuous field measurements in MRI systems. One challenging task is the search for a suitable non ^{1}H compound for the continuous monitoring probes, which provides spectral decoupling between monitoring and imaging experiments. Spectral decoupling is essential for all methods relying on concurrent imaging and monitoring, such as real-time field feedback [32], [33], retrospective correction of field fluctuation [39] and parsing of the measured sequence diagram for automatic image reconstruction [58].

Relaxation times above the 100 µs range lead to considerable probe dephasing within the short acquisition periods of the presented continuous monitoring method, resulting in limitations with respect to the maximum gradient moment that can be monitored. While the adjustment of the relaxation times is easily done with paramagnetic salts in H_2O (^{1}H) based probes, fluorine (^{19}F) based compounds did so far not allow this to the same degree.

A suitable ^{19}F compound would also help to reduce systematic phase errors caused by B_0 field inhomogeneities inside the probe droplet, because susceptibility matching of the surrounding materials would be easier due to the available choice of materials. This might also alleviate the need for numerically demanding phase calibration methods such as presented in Chapter 6.

In order to reach the same SNR as ^{1}H based probes, ^{19}F based probes need to have larger droplets due to the typically smaller spin density and gyromagnetic ratio. While this is in principle no problem, it can lead to tune-match difficulties due to the increased inductance of the also larger T/R solenoid. A decrease in SNR on the other hand might lead to problems with respect to the random walk error statistic that was observed in the continuously monitored k-space trajectories (Chapter 4).

Thus, ^{19}F delivers less sensitivity per probe volume and might

therefore not be the best choice for pure MRI system characterization measurements, but it allows concurrent monitoring and imaging and might therefore be the key to broad adoption of field monitoring.

Besides the search for a suitable compound, there is also room for other optimizations, such as for example with regard to thermal dissipation. The high re-excitation duty cycle in the range of almost 10 %, combined with increased losses in the sample due to addition of relaxation agents, can lead to sample heating and therewith drifts in the field measurements. These drifts could possibly be avoided by an improved probe design and compound selection. Alternatively, the field camera could be pre-heated until a thermal equilibrium is reached, which is a typical requirement of many precision measurement devices. Another option would be to apply short interleaved calibration measurements to track the rather slow exponential thermal drifts over time and correct them in a post-processing step.

With regard to probe excitation, shorter pulses would reduce the re-excitation gap size and therewith increase the maximum field bandwidth that can be monitored. This could be achieved with more excitation power, which would require new power amplifiers and an improved thermal dissipation management. Another approach would be the use of probe specific excitation pulses of less bandwidth. Approximate probe frequencies could be calculated from the most recent field measurement and then fed to probe specific excitation pulse generators. This would avoid large probe excitation bandwidths (800 kHz), required to excite all probes with the same pulse in the presence of strong gradients. However, it would also require a separate excitation pulse generator for each probe and a real-time frequency update algorithm as well as suitable electronics.

Ideally the measurement gap due to probe re-excitation could be removed completely if the isolation between the probes and

channels was big enough such that an excitation pulse of one probe does not corrupt the received signals from other probes, resulting in undisturbed, overlapped measurements. This has so far not been possible due to the large power difference between excitation and reception (90 dB range), which already challenges coupling between reasonably sized close-by coaxial cables.

If above issues can be solved, especially those regarding concurrent operation to imaging, continuous dynamic magnetic field monitoring might truly live up to its promises and become a natural choice for a manifold of tasks, such as sequence debugging and development, fast system characterization, long term system surveillance, failure prediction and real-time field control.

References

[1] E. M. Purcell, H. C. Torrey, and R. V. Pound, "Resonance absorption by nuclear magnetic moments in a solid", *Physical Review*, vol. 69, no. 1-2, pp. 37–38, 1946. DOI: 10.1103/PhysRev.69.37.

[2] F. Bloch, "Nuclear induction", *Physical Review*, vol. 70, no. 7-8, pp. 460–474, 1946. DOI: 10.1103/PhysRev.70.460.

[3] M. Levitt, *Spin dynamics: Basics of nuclear magnetic resonance*, 2nd ed. New York: John Wiley & Sons, 2008, ISBN: 978-0-470-51712-3.

[4] P. C. Lauterbur, "Image formation by induced local interactions: examples employing nuclear magnetic resonance", *Nature*, vol. 242, no. 5394, pp. 190–191, 1973. DOI: 10.1038/242190a0.

[5] A. Kumar, D. Welti, and R. R. Ernst, "Nmr fourier zeugmatography", *Journal of Magnetic Resonance*, vol. 18, no. 1, pp. 69–83, 1975. DOI: 10.1016/0022-2364(75)90224-3.

[6] P. Mansfield, "Multi-planar image formation using nmr spin echoes", *Journal of Physics C: Solid State Physics*, vol. 10, no. 3, pp. L55–L58, 1977. DOI: 10.1088/0022-3719/10/3/004.

[7] De Graaf, Robin A, *In vivo NMR spectroscopy: Principles and techniques*, 2nd ed. Chichester, West Sussex, England and Hoboken, NJ: John Wiley & Sons, 2007, ISBN: 978-0-470-02670-0.

[8] Y. Zhu, "Parallel excitation with an array of transmit coils", *Magnetic Resonance in Medicine*, vol. 51, no. 4, pp. 775–784, 2004. DOI: 10.1002/mrm.20011.

[9] P. Mansfield and B. Chapman, "Active magnetic screening of gradient coils in nmr imaging", *Journal of Magnetic Resonance*, vol. 66, no. 3, pp. 573–576, 1986. DOI: 10.1016/0022-2364(86)90205-2.

[10] R. Turner, "Gradient coil design: a review of methods", *Magnetic resonance imaging*, vol. 11, no. 7, pp. 903–920, 1993. DOI: 10.1016/0730-725X(93)90209-V.

[11] D. J. Schaefer, J. D. Bourland, and J. A. Nyenhuis, "Review of patient safety in time-varying gradient fields", *Journal of Magnetic Resonance Imaging*, vol. 12, no. 1, pp. 20–29, 2000. DOI: 10.1002/1522-2586(200007)12:1{<}20::AID-JMRI3{>}3.0.CO;2-Y.

[12] M. Bencsik, R. Bowtell, and R. Bowley, "Electric fields induced in the human body by time-varying magnetic field gradients in mri: numerical calculations and correlation analysis", *Physics in Medicine and Biology*, vol. 52, no. 9, pp. 2337–2353, 2007. DOI: 10.1088/0031-9155/52/9/001.

[13] D. K. Sodickson and W. J. Manning, "Simultaneous acquisition of spatial harmonics (smash): fast imaging with radiofrequency coil arrays", *Magnetic Resonance in Medicine*, vol. 38, no. 4, pp. 591–603, 1997.

[14] K. P. Pruessmann, M. Weiger, M. B. Scheidegger, and P. Boesiger, "Sense: sensitivity encoding for fast mri", *Magnetic Resonance in Medicine*, vol. 42, no. 5, pp. 952–962, 1999. DOI: 10.1002/(SICI)1522-2594(199911)42:5{<}952::AID-MRM16{>}3.0.CO;2-S.

[15] M. A. Griswold, P. M. Jakob, R. M. Heidemann, M. Nittka, V. Jellus, J. Wang, B. Kiefer, and A. Haase, "Generalized autocalibrating partially parallel acquisitions (grappa)", *Magnetic Resonance in Medicine*, vol. 47, no. 6, pp. 1202–1210, 2002. DOI: 10.1002/mrm.10171.

[16] C. Boesch, R. Gruetter, and E. Martin, "Temporal and spatial analysis of fields generated by eddy currents in superconducting magnets", *Magnetic Resonance in Medicine*, vol. 20, no. 2, pp. 268–284, 1991. DOI: 10.1002/mrm.1910200209.

[17] A. Barnett, "Comments on gradient-induced acoustic and magnetic field fluctuations in a 4t whole-body mr imager", *Magnetic Resonance in Medicine*, vol. 46, no. 2, p. 207, 2001. DOI: 10.1002/mrm.1179.

[18] T. W. Nixon, S. McIntyre, D. L. Rothman, and R. A. d. Graaf, "Compensation of gradient-induced magnetic field perturbations", *Journal of Magnetic Resonance*, vol. 192, no. 2, pp. 209–217, 2008. DOI: 10.1016/j.jmr.2008.02.016.

[19] A. Ebel and A. A. Maudsley, "Detection and correction of frequency instabilities for volumetric 1h echo-planar spectroscopic imaging", *Magnetic Resonance in Medicine*, vol. 53, no. 2, pp. 465–469, 2005. DOI: 10.1002/mrm.20367.

[20] N. D. Zanche, C. Barmet, J. A. Nordmeyer-Massner, and K. P. Pruessmann, "Nmr probes for measuring magnetic fields and field dynamics in mr systems", *Magnetic Resonance in Medicine*, vol. 60, no. 1, pp. 176–186, 2008. DOI: 10.1002/mrm.21624.

[21] C. Barmet, N. D. Zanche, and K. P. Pruessmann, "Spatiotemporal magnetic field monitoring for mr", *Magnetic Resonance in Medicine*, vol. 60, no. 1, pp. 187–197, 2008. DOI: 10.1002/mrm.21603.

[22] H. Han, R. P. MacGregor, and B. J. Balcom, "Pure phase encode magnetic field gradient monitor", *Journal of Magnetic Resonance*, vol. 201, no. 2, pp. 212–217, 2009. DOI: 10.1016/j.jmr.2009.09.011.

[23] P. T. Sipilä, S. Greding, G. Wachutka, and F. Wiesinger, "2h transmit-receive nmr probes for magnetic field monitoring in mri", *Magnetic Resonance in Medicine*, vol. 65, no. 5, pp. 1498–1506, 2011. DOI: 10.1002/mrm.22741.

[24] J. E. Lenz, "A review of magnetic sensors", *Proceedings of the IEEE*, vol. 78, no. 6, pp. 973–989, 1990. DOI: 10.1109/5.56910.

[25] P. Keller, *Technologies for precision magnetic field mapping*, 2007.

[26] S. Tumanski, "Induction coil sensors—a review", *Measurement Science and Technology*, vol. 18, no. 3, R31–R46, 2007. DOI: 10.1088/0957-0233/18/3/R01.

[27] R. Pound and W. Knight, "A radiofrequency spectrograph and simple magnetic–field meter", *The Review of Scientific Instruments*, vol. 21, no. 3, pp. 219–225, 1950. DOI: 10.1063/1.1745537.

[28] G. Boero, J. Frounchi, B. Furrer, P. A. Besse, and R. S. Popovic, "Fully integrated probe for proton nuclear magnetic resonance magnetometry", *The Review of Scientific Instruments*, vol. 72, no. 6, pp. 2764–2768, 2001. DOI: 10.1063/1.1374599.

[29] C. Barmet, B. J. Wilm, M. Pavan, and K. P. Pruessmann, "A third-order field camera with microsecond resolution for mr system diagnostics", in *Proc Int Soc Magn Reson Med Sci Meet Exhib*, vol. 17, 2009, p. 781.

[30] C. Barmet, N. D. Zanche, B. J. Wilm, and K. P. Pruessmann, "A transmit/receive system for magnetic field monitoring of in vivo mri", *Magnetic Resonance in Medicine*, vol. 62, no. 1, pp. 269–276, 2009. DOI: 10.1002/mrm.21996.

[31] C. Barmet, B. J. Wilm, M. Pavan, G. Katsikatsos, J. Keupp, G. Mens, and K. P. Pruessmann, "Concurrent higher-order field monitoring for routine head mri: an integrated heteronuclear setup", in *Proc Int Soc Magn Reson Med Sci Meet Exhib*, vol. 18, 2010, p. 216.

[32] Y. Duerst, B. J. Wilm, B. E. Dietrich, S. J. Vannesjo, C. Barmet, T. Schmid, D. O. Brunner, and K. P. Pruessmann, "Real-time feedback for spatiotemporal field stabilization in mr systems", *Magnetic Resonance in Medicine*, vol. 73, no. 2, pp. 884–893, 2014. DOI: 10.1002/mrm.25167.

[33] B. J. Wilm, Y. Duerst, B. E. Dietrich, M. Wyss, S. J. Vannesjo, T. Schmid, D. O. Brunner, C. Barmet, and K. P. Pruessmann, "Feedback field control improves linewidths in in vivo magnetic resonance spectroscopy", *Magnetic Resonance in Medicine*, vol. 71, no. 5, pp. 1657–1662, 2014. DOI: 10.1002/mrm.24836.

[34] B. J. Wilm, C. Barmet, M. Pavan, and K. P. Pruessmann, "Higher order reconstruction for mri in the presence of spatiotemporal field perturbations", *Magnetic Resonance in Medicine*, vol. 65, no. 6, pp. 1690–1701, 2011. DOI: 10.1002/mrm.22767.

[35] D. Giese, M. Haeberlin, C. Barmet, K. P. Pruessmann, T. Schaeffter, and S. Kozerke, "Analysis and correction of background velocity offsets in phase-contrast flow measurements using magnetic field monitoring", *Magnetic Resonance in Medicine*, vol. 67, no. 5, pp. 1294–1302, 2012. DOI: 10.1002/mrm.23111.

[36] R. F. Fischer, C. Barmet, M. Rudin, P. Boesiger, K. P. Pruessmann, and S. Kozerke, "Monitoring and compensating phase imperfections in cine balanced steady-state free precession", *Magnetic Resonance in Medicine*, vol. 70, no. 6, pp. 1567–1579, 2013. DOI: 10.1002/mrm.24606.

[37] L. Kasper, S. Bollmann, S. J. Vannesjo, S. Gross, M. Haeberlin, B. E. Dietrich, and K. P. Pruessmann, "Monitoring, analysis, and correction of magnetic field fluctuations in echo planar imaging time series", *Magnetic Resonance in Medicine*, vol. 74, no. 2, pp. 396–409, 2015. DOI: 10.1002/mrm.25407.

[38] L. Kasper, M. Haeberlin, B. E. Dietrich, S. Gross, C. Barmet, B. J. Wilm, S. J. Vannesjo, D. O. Brunner, C. C. Ruff, K. E. Stephan, and K. P. Pruessmann, "Matched-filter acquisition for bold fmri", *NeuroImage*, vol. 100C, pp. 145–160, 2014. DOI: 10.1016/j.neuroimage.2014.05.024.

[39] S. J. Vannesjo, B. J. Wilm, Y. Duerst, S. Gross, D. O. Brunner, B. E. Dietrich, T. Schmid, C. Barmet, and K. P. Pruessmann, "Retrospective correction of physiological field fluctuations in high-field brain mri using concurrent field monitoring", *Magnetic Resonance in Medicine*, vol. 73, no. 5, pp. 1833–1843, 2015. DOI: 10.1002/mrm.25303.

[40] M. Haeberlin, L. Kasper, C. Barmet, D. O. Brunner, B. E. Dietrich, S. Gross, B. J. Wilm, S. Kozerke, and K. P. Pruessmann, "Real-time motion correction using gradient tones and head-mounted nmr field probes", *Magnetic Resonance in Medicine*, vol. 74, no. 3, pp. 647–660, 2015. DOI: 10.1002/mrm.25432.

[41] S. J. Vannesjo, B. E. Dietrich, M. Pavan, D. O. Brunner, B. J. Wilm, C. Barmet, and K. P. Pruessmann, "Field camera measurements of gradient and shim impulse responses using frequency sweeps", *Magnetic Resonance in Medicine*, vol. 72, no. 2, pp. 570–583, 2014. DOI: 10.1002/mrm.24934.

[42] S. J. Vannesjo, M. Haeberlin, L. Kasper, M. Pavan, B. J. Wilm, C. Barmet, and K. P. Pruessmann, "Gradient system characterization by impulse response measurements with a dynamic field camera", *Magnetic Resonance in Medicine*, vol. 69, no. 2, pp. 583–593, 2013. DOI: 10.1002/mrm.24263.

[43] P. B. Kenington, *RF and baseband techniques for software defined radio*, ser. Mobile communications series. Boston: Artech House, 2005, ISBN: 1580537936.

[44] W. E. Doherty Jr and R. Joos, *Pin diode circuit designers handbook*, 1999.

[45] K. P. Pruessmann, M. Weiger, P. Börnert, and P. Boesiger, "Advances in sensitivity encoding with arbitrary k-space trajectories", *Magnetic Resonance in Medicine*, vol. 46, no. 4, pp. 638–651, 2001. DOI: 10.1002/mrm.1241.

[46] U. Katscher, P. Börnert, C. Leussler, and van den Brink, Johan S, "Transmit sense", *Magnetic Resonance in Medicine*, vol. 49, no. 1, pp. 144–150, 2003. DOI: 10.1002/mrm.10353.

[47] I. Graesslin, "Parallel transmission: a comprehensive rf safety concept", in *Progress in Electromagnetics Research Symposium*, 2008, pp. 698–700.

[48] D. O. Brunner and K. P. Pruessmann, "Optimal design of multiple-channel rf pulses under strict power and sar constraints", *Magnetic Resonance in Medicine*, vol. 63, no. 5, pp. 1280–1291, 2010. DOI: 10.1002/mrm.22330.

[49] I. Graesslin, P. Vernickel, P. Börnert, K. Nehrke, G. Mens, P. Harvey, and U. Katscher, "Comprehensive rf safety concept for parallel transmission mr", *Magnetic Resonance in Medicine*, vol. 74, no. 2, pp. 589–598, 2015. DOI: 10.1002/mrm.25425.

[50] G. Scott, P. Stang, W. Overall, A. B. Kerr, and J. M. Pauly, "Signal vector decoupling for transmit arrays", in *Proc Int Soc Magn Reson Med Sci Meet Exhib*, 2007, p. 168.

[51] *The ARRL handbook for radio communications, 2008*, 85th ed. Newington, CT: American Radio Relay League, 2007, ISBN: 0-87259-102-6.

[52] B. E. Dietrich, D. O. Brunner, B. J. Wilm, C. Barmet, S. Gross, L. Kasper, M. Haeberlin, T. Schmid, S. J. Vannesjo, and K. P. Pruessmann, "A field camera for mr sequence monitoring and system analysis", *Magnetic Resonance in Medicine*, 2015. DOI: 10.1002/mrm.25770.

[53] C. W. Farrow, "A continuously variable digital delay element", in *IEEE International Symposium on Circuits and Systems*, vol. 3, 1988, pp. 2641–2645.

[54] C. J. Bergin, J. M. Pauly, and A. Macovski, "Lung parenchyma: projection reconstruction mr imaging", *Radiology*, vol. 179, no. 3, pp. 777–781, 1991. DOI: 10.1148/radiology.179.3.2027991.

[55] W. Grissom, C.-y. Yip, Z. Zhang, V. A. Stenger, J. A. Fessler, and D. C. Noll, "Spatial domain method for the design of rf pulses in multicoil parallel excitation", *Magnetic Resonance in Medicine*, vol. 56, no. 3, pp. 620–629, 2006. DOI: 10.1002/mrm.20978.

[56] C. Ma, D. Xu, K. F. King, and Z.-P. Liang, "Joint design of spoke trajectories and rf pulses for parallel excitation", *Magnetic Resonance in Medicine*, vol. 65, no. 4, pp. 973–985, 2011. DOI: 10.1002/mrm.22676.

[57] J. Vuolevi and T. Rahkonen, *Distortion in RF power amplifiers*, ser. Artech House microwave library. Boston: Artech House, 2003, ISBN: 1580536298.

[58] D. O. Brunner, B. E. Dietrich, C. Barmet, S. Gross, B. J. Wilm, and K. P. Pruessmann, "Automatic reconstruction of gradient echo imaging sequences by concurrent and continuous monitoring of gradient and rf waveforms", in *Proc Int Soc Magn Reson Med Sci Meet Exhib*, vol. 21, 2013, p. 553.

[59] B. E. Dietrich, C. Barmet, D. O. Brunner, and K. P. Pruessmann, "An autonomous system for continuous field monitoring with interleaved probe sets", in *Proc Int Soc Magn Reson Med Sci Meet Exhib*, vol. 19, 2011, p. 1842.

[60] K. R. Minard and R. A. Wind, "Solenoidal microcoil design. part ii", *Concepts in Magnetic Resonance*, vol. 13, no. 3, pp. 190–210, 2001. DOI: 10.1002/cmr.1008.

[61] J. Mispelter, M. Lupu, and A. Briguet, *NMR probeheads for biophysical and biomedical experiments: Theoretical principles & practical guidelines*. London: Imperial College Press, 2006, ISBN: 1860946372.

[62] D. O. Brunner, B. E. Dietrich, M. Cavusoglu, C. Barmet, B. J. Wilm, and K. P. Pruessmann, "Concurrent monitoring of rf and gradient waveforms of parallel transmission pulses by a field camera", in *Proc Int Soc Magn Reson Med Sci Meet Exhib*, vol. 21, 2013, p. 293.

[63] J. Hennig, A. Nauerth, and H. Friedburg, "Rare imaging: a fast imaging method for clinical mr", *Magnetic Resonance in Medicine*, vol. 3, no. 6, pp. 823–833, 1986. DOI: 10.1002/mrm.1910030602.

[64] P. A. Bottomley, "Spatial localization in nmr spectroscopy in vivo", *Annals of the New York Academy of Sciences*, vol. 508, no. 1 Physiological, pp. 333–348, 1987. DOI: 10.1111/j.1749-6632.1987.tb32915.x.

[65] M. B. Ooi, S. Krueger, W. J. Thomas, S. V. Swaminathan, and T. R. Brown, "Prospective real-time correction for arbitrary head motion using active markers", *Magnetic Resonance in Medicine*, vol. 62, no. 4, pp. 943–954, 2009. DOI: 10.1002/mrm.22082.

[66] A. M. Blamire, D. L. Rothman, and T. W. Nixon, "Dynamic shim updating: a new approach towards optimized whole brain shimming", *Magnetic Resonance in Medicine*, vol. 36, no. 1, pp. 159–165, 1996. DOI: 10.1002/mrm.1910360125.

[67] R. A. d. Graaf, P. B. Brown, S. McIntyre, D. L. Rothman, and T. W. Nixon, "Dynamic shim updating (dsu) for multislice signal acquisition", *Magnetic Resonance in Medicine*, vol. 49, no. 3, pp. 409–416, 2003. DOI: 10.1002/mrm.10404.

[68] K. M. Koch, L. I. Sacolick, T. W. Nixon, S. McIntyre, D. L. Rothman, and R. A. d. Graaf, "Dynamically shimmed multivoxel 1h magnetic resonance spectroscopy and multislice magnetic resonance spectroscopic imaging of the human brain", *Magnetic Resonance in Medicine*, vol. 57, no. 3, pp. 587–591, 2007. DOI: 10.1002/mrm.21141.

[69] C. Juchem, T. W. Nixon, P. Diduch, D. L. Rothman, P. Starewicz, and R. A. d. Graaf, "Dynamic shimming of the human brain at 7 tesla", *Concepts in Magnetic Resonance Part B: Magnetic Resonance Engineering*, vol. 37B, no. 3, pp. 116–128, 2010. DOI: 10.1002/cmr.b.20169.

[70] J. Hennig, A. M. Welz, G. Schultz, J. Korvink, Z. Liu, O. Speck, and M. Zaitsev, "Parallel imaging in non-bijective, curvilinear magnetic field gradients: a concept study", *Magnetic Resonance Materials in Physics, Biology, and Medicine*, vol. 21, no. 1-2, pp. 5–14, 2008. DOI: 10.1007/s10334-008-0105-7.

[71] F. Testud, D. Gallichan, K. J. Layton, C. Barmet, A. M. Welz, A. Dewdney, C. A. Cocosco, K. P. Pruessmann, J. Hennig, and M. Zaitsev, "Single-shot imaging with higher-dimensional encoding using magnetic field monitoring and concomitant field correction", *Magnetic Resonance in Medicine*, vol. 73, no. 3, pp. 1340–1357, 2015. DOI: 10.1002/mrm.25235.

[72] N. O. Addy, H. H. Wu, and D. G. Nishimura, "Simple method for mr gradient system characterization and k-space trajectory estimation", *Magnetic Resonance in Medicine*, vol. 68, no. 1, pp. 120–129, 2012. DOI: 10.1002/mrm.23217.

[73] M. A. Morich, D. A. Lampman, W. R. Dannels, and F. Goldie, "Exact temporal eddy current compensation in magnetic resonance imaging systems", *IEEE transactions on medical imaging*, vol. 7, no. 3, pp. 247–254, 1988. DOI: 10.1109/42.7789.

[74] S. J. Vannesjo, B. E. Dietrich, M. Pavan, C. Barmet, and K. P. Pruessmann, "Digital cross-term pre-emphasis for higher-order dynamic shimming", in *Proc Int Soc Magn Reson Med Sci Meet Exhib*, vol. 21, 2013, p. 671.

[75] B. E. Dietrich, D. O. Brunner, B. J. Wilm, C. Barmet, and K. P. Pruessmann, "Analysis of measurement precision in continuous magnetic field monitoring", in *Proc Int Soc Magn Reson Med Sci Meet Exhib*, vol. 21, 2013, p. 2716.

[76] M. A. Bernstein, X. J. Zhou, J. A. Polzin, K. F. King, A. Ganin, N. J. Pelc, and G. H. Glover, "Concomitant gradient terms in phase contrast mr: analysis and correction", *Magnetic Resonance in Medicine*, vol. 39, no. 2, pp. 300–308, 1998.

[77] S. Gross, C. Barmet, B. E. Dietrich, and K. P. Pruessmann, "Observation of longitudinal nuclear magnetization dynamics with nmr field probes", in *Proc Int Soc Magn Reson Med Sci Meet Exhib*, vol. 20, 2012, p. 378.

[78] S. Gross, B. E. Dietrich, C. Barmet, and K. P. Pruessmann, "Improved t1 relaxometry with nmr field probes: demonstration of contrast agent characterization", in *Proc Int Soc Magn Reson Med Sci Meet Exhib*, vol. 21, 2013, p. 466.

[79] K. P. Pruessmann, B. E. Dietrich, and C. Barmet, "Observation of cardiovascular dynamics by field recording with an nmr probe", in *Proc Int Soc Magn Reson Med Sci Meet Exhib*, vol. 19, 2011, p. 1171.

[80] S. Gross, B. E. Dietrich, C. Barmet, and K. P. Pruessmann, "Spatially resolved observation of cardiovascular magnetodynamics with nmr field probes", in *Proc Int Soc Magn Reson Med Sci Meet Exhib*, vol. 21, 2013, p. 1410.

[81] D. O. Brunner, M. Pavan, B. E. Dietrich, and K. P. Pruessmann, "Sideband excitation for concurrent rf transmission and reception", in *Proc Int Soc Magn Reson Med Sci Meet Exhib*, vol. 19, 2011, p. 625.

[82] D. O. Brunner, B. E. Dietrich, M. Pavan, and K. P. Pruessmann, "Mri with sideband excitation: application to continuous swift", in *Proc Int Soc Magn Reson Med Sci Meet Exhib*, vol. 20, 2012, p. 150.

[83] M. Weiger, D. O. Brunner, B. E. Dietrich, C. F. Müller, and K. P. Pruessmann, "Zte imaging in humans", *Magnetic Resonance in Medicine*, vol. 70, no. 2, pp. 328–332, 2013. DOI: 10.1002/mrm.24816.

Curriculum Vitae

Name:	Benjamin Emanuel Dietrich
Date of birth:	7$^{\text{th}}$ December 1982
Citizenship:	Swiss

Education

2009 – 2015 **Doctoral candidate**
Institute for Biomedical Engineering, ETH Zurich

2007 – 2009 **Master in Electrical Engineering and Information Technology**, *ETH Zurich*
Specialization in communication technology and integrated circuits.

2004 – 2007 **Bachelor in Electrical Engineering and Information Technology**, *ETH Zurich*
Specialization in computer networks.

2001 – 2003 **High School**
Gymnasium Münchenstein, Basel-Landschaft
Type A: Physics and Math.

List of Publications

Journal Articles

[1] B. E. Dietrich, D. O. Brunner, B. J. Wilm, C. Barmet, S. Gross, L. Kasper, M. Haeberlin, T. Schmid, S. J. Vannesjo, and K. P. Pruessmann, "A field camera for mr sequence monitoring and system analysis", *Magnetic Resonance in Medicine*, 2015. DOI: 10.1002/mrm.25770.

[2] D. O. Brunner, B. E. Dietrich, M. Çavuşoğlu, B. J. Wilm, T. Schmid, S. Gross, C. Barmet, and K. P. Pruessmann, "Concurrent recording of rf pulses and gradient fields - comprehensive field monitoring for mri", *NMR in biomedicine*, 2015. DOI: 10.1002/nbm.3359.

[3] B. J. Wilm, Z. Nagy, C. Barmet, S. J. Vannesjo, L. Kasper, M. Haeberlin, S. Gross, B. E. Dietrich, D. O. Brunner, T. Schmid, and K. P. Pruessmann, "Diffusion mri with concurrent magnetic field monitoring", *Magnetic Resonance in Medicine*, 2015. DOI: 10.1002/mrm.25827.

[4] Y. Duerst, B. J. Wilm, M. Wyss, B. E. Dietrich, S. Gross, T. Schmid, D. O. Brunner, and K. P. Pruessmann, "Utility of real-time field control in t2 *-weighted head mri at 7t", *Magnetic Resonance in Medicine*, 2015. DOI: 10.1002/mrm.25838.

[5] M. Haeberlin, L. Kasper, C. Barmet, D. O. Brunner, B. E. Dietrich, S. Gross, B. J. Wilm, S. Kozerke, and K. P. Pruessmann, "Real-time motion correction using gradient tones and

head-mounted nmr field probes", *Magnetic Resonance in Medicine*, vol. 74, no. 3, pp. 647–660, 2015. DOI: 10.1002/mrm.25432.

[6] L. Kasper, S. Bollmann, S. J. Vannesjo, S. Gross, M. Haeberlin, B. E. Dietrich, and K. P. Pruessmann, "Monitoring, analysis, and correction of magnetic field fluctuations in echo planar imaging time series", *Magnetic Resonance in Medicine*, vol. 74, no. 2, pp. 396–409, 2015. DOI: 10.1002/mrm.25407.

[7] S. J. Vannesjo, B. J. Wilm, Y. Duerst, S. Gross, D. O. Brunner, B. E. Dietrich, T. Schmid, C. Barmet, and K. P. Pruessmann, "Retrospective correction of physiological field fluctuations in high-field brain mri using concurrent field monitoring", *Magnetic Resonance in Medicine*, vol. 73, no. 5, pp. 1833–1843, 2015. DOI: 10.1002/mrm.25303.

[8] L. Kasper, M. Haeberlin, B. E. Dietrich, S. Gross, C. Barmet, B. J. Wilm, S. J. Vannesjo, D. O. Brunner, C. C. Ruff, K. E. Stephan, and K. P. Pruessmann, "Matched-filter acquisition for bold fmri", *NeuroImage*, vol. 100C, pp. 145–160, 2014. DOI: 10.1016/j.neuroimage.2014.05.024.

[9] B. J. Wilm, Y. Duerst, B. E. Dietrich, M. Wyss, S. J. Vannesjo, T. Schmid, D. O. Brunner, C. Barmet, and K. P. Pruessmann, "Feedback field control improves linewidths in in vivo magnetic resonance spectroscopy", *Magnetic Resonance in Medicine*, vol. 71, no. 5, pp. 1657–1662, 2014. DOI: 10.1002/mrm.24836.

[10] Y. Duerst, B. J. Wilm, B. E. Dietrich, S. J. Vannesjo, C. Barmet, T. Schmid, D. O. Brunner, and K. P. Pruessmann, "Real-time feedback for spatiotemporal field stabilization in mr systems", *Magnetic Resonance in Medicine*, vol. 73, no. 2, pp. 884–893, 2014. DOI: 10.1002/mrm.25167.

[11] S. J. Vannesjo, B. E. Dietrich, M. Pavan, D. O. Brunner, B. J. Wilm, C. Barmet, and K. P. Pruessmann, "Field camera measurements of gradient and shim impulse responses using

frequency sweeps", *Magnetic Resonance in Medicine*, vol. 72, no. 2, pp. 570–583, 2014. DOI: 10.1002/mrm.24934.

[12] M. Weiger, D. O. Brunner, B. E. Dietrich, C. F. Müller, and K. P. Pruessmann, "Zte imaging in humans", *Magnetic Resonance in Medicine*, vol. 70, no. 2, pp. 328–332, 2013. DOI: 10.1002/mrm.24816.

Conference Contributions

[1] K. P. Pruessmann, B. E. Dietrich, and C. Barmet, "Observation of cardiovascular dynamics by field recording with an nmr probe", in *Proc Int Soc Magn Reson Med Sci Meet Exhib*, vol. 19, 2011, p. 1171.

[2] D. O. Brunner, M. Pavan, B. E. Dietrich, and K. P. Pruessmann, "Sideband excitation for concurrent rf transmission and reception", in *Proc Int Soc Magn Reson Med Sci Meet Exhib*, vol. 19, 2011, p. 625.

[3] B. E. Dietrich, C. Barmet, D. O. Brunner, and K. P. Pruessmann, "An autonomous system for continuous field monitoring with interleaved probe sets", in *Proc Int Soc Magn Reson Med Sci Meet Exhib*, vol. 19, 2011, p. 1842.

[4] B. E. Dietrich, D. O. Brunner, C. Barmet, B. J. Wilm, and K. P. Pruessmann, "A stand-alone system for concurrent gradient and rf sequence monitoring", in *Proc Int Soc Magn Reson Med Sci Meet Exhib*, vol. 20, 2012, p. 700.

[5] S. Gross, C. Barmet, B. E. Dietrich, and K. P. Pruessmann, "Observation of longitudinal nuclear magnetization dynamics with nmr field probes", in *Proc Int Soc Magn Reson Med Sci Meet Exhib*, vol. 20, 2012, p. 378.

[6] S. J. Vannesjo, B. E. Dietrich, C. Barmet, B. J. Wilm, D. O. Brunner, and K. P. Pruessmann, "Measurement and preemphasis of shim responses using frequency sweeps", in *Proc Int Soc Magn Reson Med Sci Meet Exhib*, vol. 20, 2012, p. 142.

[7] B. J. Wilm, C. Barmet, L. Kasper, M. Haeberlin, B. E. Dietrich, and K. P. Pruessmann, "Partial fourier accelerated spiral sense imaging using magnetic field monitoring", in *Proc Int Soc Magn Reson Med Sci Meet Exhib*, vol. 20, 2012, p. 2544.

[8] Y. Duerst, B. J. Wilm, B. E. Dietrich, S. J. Vannesjo, and K. P. Pruessmann, "Real-time shim feedback for field stabilization in human mri systems", in *Proc Int Soc Magn Reson Med Sci Meet Exhib*, vol. 20, 2012, p. 702.

[9] M. Weiger, D. O. Brunner, B. E. Dietrich, C. F. Müller, and K. P. Pruessmann, "Zte imaging on a human whole-body system", in *Proc Int Soc Magn Reson Med Sci Meet Exhib*, vol. 20, 2012, p. 2296.

[10] D. O. Brunner, B. E. Dietrich, M. Pavan, and K. P. Pruessmann, "Mri with sideband excitation: application to continuous swift", in *Proc Int Soc Magn Reson Med Sci Meet Exhib*, vol. 20, 2012, p. 150.

[11] Y. Duerst, B. J. Wilm, B. E. Dietrich, D. O. Brunner, C. Barmet, T. Schmid, S. J. Vannesjo, and K. P. Pruessmann, "Full 3rd order real-time shim feedback for field stabilization and its application in brain mri at 7t", in *Proc Int Soc Magn Reson Med Sci Meet Exhib*, vol. 21, 2013, p. 669.

[12] S. Klein, L. Kasper, S. J. Vannesjo, M. Haeberlin, S. Gross, B. E. Dietrich, and K. P. Pruessmann, "Concurrent magnetic field monitoring of epi time series: characterizing encoding field and image fluctuations using principal compo-

nent analysis", in *Proc Int Soc Magn Reson Med Sci Meet Exhib*, vol. 21, 2013, p. 2715.

[13] S. Gross, B. E. Dietrich, C. Barmet, and K. P. Pruessmann, "Spatially resolved observation of cardiovascular magnetodynamics with nmr field probes", in *Proc Int Soc Magn Reson Med Sci Meet Exhib*, vol. 21, 2013, p. 1410.

[14] S. J. Vannesjo, B. J. Wilm, Y. Duerst, B. E. Dietrich, D. O. Brunner, C. Barmet, T. Schmid, and K. P. Pruessmann, "Snapshot field monitoring enables correction of slow field perturbations in high-resolution brain mri", in *Proc Int Soc Magn Reson Med Sci Meet Exhib*, vol. 21, 2013, p. 2569.

[15] S. J. Vannesjo, B. E. Dietrich, M. Pavan, C. Barmet, and K. P. Pruessmann, "Digital cross-term pre-emphasis for higher-order dynamic shimming", in *Proc Int Soc Magn Reson Med Sci Meet Exhib*, vol. 21, 2013, p. 671.

[16] L. Kasper, M. Haeberlin, B. E. Dietrich, S. Gross, C. Barmet, C. C. Ruff, K. E. Stephan, and K. P. Pruessmann, "Analysis of bold sensitivity in matched filter fmri", in *Proc Int Soc Magn Reson Med Sci Meet Exhib*, vol. 21, 2013, p. 3332.

[17] N. N. Graedel, S. J. Vannesjo, L. Kasper, S. Gross, B. E. Dietrich, C. Barmet, and K. P. Pruessmann, "Image reconstruction using the gradient impulse response for trajectory prediction", in *Proc Int Soc Magn Reson Med Sci Meet Exhib*, vol. 21, 2013, p. 552.

[18] M. Weiger, D. O. Brunner, B. E. Dietrich, and K. P. Pruessmann, "High-bandwidth zte imaging with sub-millisecond tr", in *Proc Int Soc Magn Reson Med Sci Meet Exhib*, vol. 21, 2013, p. 761.

[19] B. J. Wilm, Y. Duerst, B. E. Dietrich, M. Wyss, D. O. Brunner, C. Barmet, T. Schmid, S. J. Vannesjo, and K. P. Pruessmann, "Higher-order feedback field control improves

linewidths in mr spectroscopy at 7t", in *Proc Int Soc Magn Reson Med Sci Meet Exhib*, vol. 21, 2013, p. 529.

[20] D. O. Brunner, B. E. Dietrich, C. Barmet, S. Gross, B. J. Wilm, and K. P. Pruessmann, "Automatic reconstruction of gradient echo imaging sequences by concurrent and continuous monitoring of gradient and rf waveforms", in *Proc Int Soc Magn Reson Med Sci Meet Exhib*, vol. 21, 2013, p. 553.

[21] D. O. Brunner, B. E. Dietrich, M. Cavusoglu, C. Barmet, B. J. Wilm, and K. P. Pruessmann, "Concurrent monitoring of rf and gradient waveforms of parallel transmission pulses by a field camera", in *Proc Int Soc Magn Reson Med Sci Meet Exhib*, vol. 21, 2013, p. 293.

[22] D. O. Brunner, B. E. Dietrich, M. Pavan, and K. P. Pruessmann, "Fast reconstruction for rf monitored sweep imaging with sideband excitation", in *Proc Int Soc Magn Reson Med Sci Meet Exhib*, vol. 21, 2013, p. 78.

[23] B. E. Dietrich, D. O. Brunner, B. J. Wilm, C. Barmet, and K. P. Pruessmann, "Analysis of measurement precision in continuous magnetic field monitoring", in *Proc Int Soc Magn Reson Med Sci Meet Exhib*, vol. 21, 2013, p. 2716.

[24] J. Reber, J. Marjanovic, D. O. Brunner, T. Schmid, U. Moser, B. E. Dietrich, C. Barmet, and K. P. Pruessmann, "In-bore broadband array receivers with optical transmission", in *Proc Int Soc Magn Reson Med Sci Meet Exhib*, vol. 22, 2014, p. 619.

[25] Y. Duerst, M. Wyss, B. J. Wilm, B. E. Dietrich, S. Gross, D. O. Brunner, T. Schmid, and K. P. Pruessmann, "Feedback field control in 3d t2* imaging at 7t", in *Proc Int Soc Magn Reson Med Sci Meet Exhib*, vol. 22, 2014, p. 1417.

[26] S. Klein, L. Kasper, S. J. Vannesjo, S. Gross, B. E. Dietrich, C. Barmet, M. Haeberlin, D. O. Brunner, B. J. Wilm, and K. P. Pruessmann, "Physiological and system-induced field fluctuations in epi time series in vivo", in *Proc Int Soc Magn Reson Med Sci Meet Exhib*, vol. 22, 2014, p. 3067.

[27] M. Wyss, Y. Duerst, B. J. Wilm, B. E. Dietrich, T. Schmid, C. Barmet, and K. P. Pruessmann, "Feedback field control improves the accuracy of t2* mapping at 7t", in *Proc Int Soc Magn Reson Med Sci Meet Exhib*, vol. 22, 2014, p. 929.

[28] Y. Duerst, B. J. Wilm, S. J. Vannesjo, B. E. Dietrich, S. Gross, D. O. Brunner, T. Schmid, and K. P. Pruessmann, "Faster feedback field control using shim pre-emphasis", in *Proc Int Soc Magn Reson Med Sci Meet Exhib*, vol. 22, 2014, p. 1387.

[29] Y. Duerst, M. Wyss, B. J. Wilm, B. E. Dietrich, S. Gross, D. O. Brunner, T. Schmid, and K. P. Pruessmann, "Utility of real-time field control in t2* imaging at 7t", in *Proc Int Soc Magn Reson Med Sci Meet Exhib*, vol. 22, 2014, p. 312.

[30] M. Weiger, D. O. Brunner, M. Wyss, B. E. Dietrich, B. J. Wilm, and K. P. Pruessmann, "Zte imaging with t1 contrast", in *Proc Int Soc Magn Reson Med Sci Meet Exhib*, vol. 22, 2014, p. 4262.

[31] J. Marjanovic, J. Reber, D. O. Brunner, M. Weiger, B. E. Dietrich, T. Schmid, U. Moser, C. Barmet, and K. P. Pruessmann, "Dead time reduction with a variable rate broadband receiver – applications to zero echo time imaging", in *Proc Int Soc Magn Reson Med Sci Meet Exhib*, vol. 22, 2014, p. 927.

[32] B. E. Dietrich, B. J. Wilm, D. O. Brunner, Y. Duerst, C. Barmet, and K. P. Pruessmann, "K-t-calibration improves continuous field monitoring for image reconstruction", in *Proc Int Soc Magn Reson Med Sci Meet Exhib*, vol. 22, 2014, p. 1390.

[33] B. J. Wilm, L. Kasper, Y. Duerst, B. E. Dietrich, S. Gross, T. Schmid, D. O. Brunner, C. Barmet, and K. P. Pruessmann, "Real-time field control for enhanced temporal snr in fmri time series", in *Proc Int Soc Magn Reson Med Sci Meet Exhib*, vol. 22, 2014, p. 862.

[34] B. E. Dietrich, D. O. Brunner, S. J. Vannesjo, Y. Duerst, B. J. Wilm, and K. P. Pruessmann, "Continuous 3rd-order field monitoring: design and application for single-shot shim characterization", in *Proc Int Soc Magn Reson Med Sci Meet Exhib*, vol. 23, 2015, p. 1016.

[35] M. Cavusoglu, L. Kasper, S. J. Vannesjo, B. E. Dietrich, S. Gross, and K. P. Pruessmann, "Correcting for encoding filed imperfections in arterial spin labeling using gradient impulse responses and concurrent field monitoring", in *Proc Int Soc Magn Reson Med Sci Meet Exhib*, vol. 23, 2015, p. 2954.

[36] D. O. Brunner, B. E. Dietrich, S. Gross, T. Schmid, C. Barmet, and K. P. Pruessmann, "Field monitoring during high-power transmission pulses: a digital noise cancelling approach", in *Proc Int Soc Magn Reson Med Sci Meet Exhib*, vol. 23, 2015, p. 1013.

[37] D. O. Brunner, S. Gross, J. Nussbaum, B. E. Dietrich, C. Barmet, and K. P. Pruessmann, "Field probes with in-situ controllable thermal relaxation times", in *Proc Int Soc Magn Reson Med Sci Meet Exhib*, vol. 23, 2015, p. 448.

[38] B. J. Wilm, C. Barmet, S. Gross, L. Kasper, S. J. Vannesjo, M. Haeberlin, B. E. Dietrich, D. O. Brunner, T. Schmid, and K. P. Pruessmann, "High-resolution single-shot spiral imaging using magnetic field monitoring and its application to diffusion weighted mri", in *Proc Int Soc Magn Reson Med Sci Meet Exhib*, vol. 23, 2015, p. 955.

[39] L. Kasper, M. Haeberlin, S. Bollmann, S. J. Vannesjo, B. J. Wilm, B. E. Dietrich, S. Gross, K. E. Stephan, and K. P. Pruessmann, "Matched-filter acquisition of high-resolution single-shot spirals", in *Proc Int Soc Magn Reson Med Sci Meet Exhib*, vol. 23, 2015, p. 2060.

[40] M. Cavusoglu, B. E. Dietrich, D. O. Brunner, and K. P. Pruessmann, "Optimization of parallel rf transmission enabled by concurrent recording of rf and gradient fields", in *Proc Int Soc Magn Reson Med Sci Meet Exhib*, vol. 23, 2015, p. 1819.

Acknowledgements

Many people have contributed directly or indirectly to this work and supported me over these last years. I am very grateful for all the support, knowledge, and discussions I was confronted with every day and feel very much indebted to many people. Therefore I hereby want to thank everyone at the Institute for Biomedical Engineering of the University of Zurich and ETH Zurich for creating such a pleasant environment for both research and after-work activities. I further would like to address special credits in arbitrary units and order to:

Prof. Dr. Klaas Pruessmann for giving me the opportunity to work in his group, for supervising this thesis and for trustful guidance.

Dr. David Brunner, Dr. Christoph Barmet and Dr. Bertram Wilm for being my go-to guys with respect to any scientific problem, for always providing immediate solutions or paths to solutions and for the continuous interest in my work.

My hardware guys: Dr. Matteo Pavan, Giorgos Katsikatsos, Dr. Jan Paska, Jonas Reber and Josip Marjanovic for sharing the burdens of hardware engineering with me.

My former and current office colleagues: Dr. Alexander Fuchs, Dr. Andreas Hock, Dr. Milan Scheidegger, Simon Gross, Constantin von Deuster, Dr. Erin MacMillan, Nicole Fichtner, Dr. Ioan-Andrei Manoliu, Jennifer Nussbaum and Zsofia Proehle.

The entire MR-Technology group: Dr. Johanna Vannesjo, Dr. Maximilian Haeberlin, Dr. Lars Kasper, Dr. Mustafa Cavusoglu, Yolanda Duerst, Alexander Penn, Laetitia Vionnet, Alexander Aranovitch, Romain Froidevaux, Michael Wyss, Thomas Schmid and Dr. Markus Weiger.

The entire MR group with its former and present members: Dr. Christian Stoeck, Dr. Johannes Schmidt, Dr. Carolin Reischauer, Dr. Xing Chen, Maximilian Fuetterer, Dr. Thomas Kirchner, Patrik Wespi, Niklaus Zoelch, Christian Binter, Julia Busch, Dr. Claudio Santelli, Lukas Wiessmann, Georg Spinner, Jonas Steinhauser, Vlad Ceregan, Adrian Huber, Dr. Martin Bührer, Dr. Anke Henning and many more.

The former and present backbones of the institute: Marianne Berg, Prof. Dr. Peter Boesiger, Dr. Roger Lüchinger and Isabel Spiess.

Stephen Wheeler for his help with mechanical construction of various monitoring system components.

Prof. Dr. Richard Bowtell for co-examining this thesis.

My friends Lukas Haas, Gabriel Schneider and Amanda Hüsler for influencing my decision on whether or not to pursue this path in my life.

My family: Erika, Männi†, Adrian, Salome, Anna-Laetitia and Mauritius.

And last but not least: Dian Liu for sharing many wonderful moments with me, on various mountains and in various countries.